

박 사 학 위 논 문

Ph.D. Dissertation

연속체 역학 기반 4 절점 쉘 유한요소의
막잠김 현상 해결

Alleviation of membrane locking in continuum-mechanics
based 4-node quadrilateral shell elements

2017

고 영 빈 (高 瑛 彬 Ko, Yeongbin)

한 국 과 학 기 술 원

Korea Advanced Institute of Science and Technology

박 사 학 위 논 문

연속체 역학 기반 4 절점
셀 유한요소의 막잠김 현상 해결

2017

고 영 빈

한 국 과 학 기 술 원

기 계 공 학

연속체 역학 기반 4 절점 셸 유한요소의 막잠김 현상 해결

고 영 빈

위 논문은 한국과학기술원 박사학위논문으로
학위논문 심사위원회의 심사를 통과하였음

2016 년 11 월 30 일

심사위원장 이 필 승



심사위원 이 병 채



심사위원 윤 정 환



심사위원 김 도 년



심사위원 정 현



Alleviation of membrane locking in continuum-mechanics based 4-node quadrilateral shell elements

Yeongbin Ko

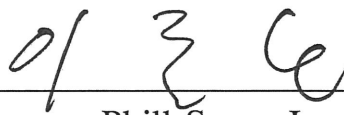
Advisor: Phill-Seung Lee

A dissertation/thesis submitted to the faculty of
Korea Advanced Institute of Science and Technology in
partial fulfillment of the requirements for the degree of
Doctor of Philosophy in Mechanical Engineering

Daejeon, Korea

November 30, 2016

Approved by



Phill-Seung Lee,

Professor of Mechanical Engineering

The study was conducted in accordance with Code of Research Ethics¹

1) Declaration of Ethical Conduct in Research: I, as a graduate student of Korea Advanced Institute of Science and Technology, hereby declare that I have not committed any act that may damage the credibility of my research. This includes, but is not limited to, falsification, thesis written by someone else, distortion of research findings, and plagiarism. I confirm that my dissertation contains honest conclusions based on my own careful research under the guidance of my advisor.

DME
20135014

고영빈. 연속체 역학 기반 4 절점 쉘 유한요소의 막잠김 현상 해결. 기계공학. 2017 년. 131+viii 쪽. 지도교수: 이필승. (영문 논문)

Yeongbin Ko. Alleviation of membrane locking in continuum-mechanics based 4-node quadrilateral shell elements. Department of Mechanical Engineering. 2017. 131+viii pages. Advisor: Phill-Seung Lee. (Text in English)

Abstract: In this paper, several continuum-mechanics based finite elements are developed by remedying their deficiencies. Our focus is to develop reliable and efficient shell and solid-shell elements satisfying the ellipticity, consistency and inf-sup conditions. That is, basic tests including the isotropy, patch and zero energy mode tests should be passed and the elements should show uniformly optimal convergence to reference solutions regardless of asymptotic categories of the shell structures considered. Membrane locking severely deteriorates the performance of the of 4-node quadrilateral shell elements when curved geometries are solved with distorted meshes. Previous studies to remedy membrane locking based on reduced integration and assumed strain method has not been successful in developing reliable 4-node shell elements. In the present study, membrane locking in 4-node quadrilateral shell elements is deeply studied for arbitrary mesh geometry. Three new 4-node shell elements developed are presented. In addition, 6-node triangular solid-shell element is developed as an extension of previous shear locking treatment of 3-node shell element and the remedies of thickness locking in the previous literatures. The newly developed continuum-mechanics based shell elements are examined through basic numerical tests as well as comprehensive convergence studies encompassing the practical range of shell thickness.

Keywords: shell element, solid-shell element, assumed strain method, membrane locking, thickness locking

Table of contents

Abstract	i
Table of Contents	ii
List of Tables	v
List of Figures	vi

Chapter 1. Introduction

1.1 Introduction	1
1.2 Previous studies of low-order shell elements	2
1.2.1 Solid-shell elements	2
1.2.2 Flat shell elements	4
1.2.3 Degenerated shell elements	5
1.3 Type of locking and its treatments	7
1.3.1 Membrane locking problem	9
1.3.2 Mathematical derivation of the cause of membrane locking	10
1.3.3 Previous treatments of membrane locking	14
1.3.4 Previous treatment of thickness locking	16
1.4 Basic requirements and basic tests	18
1.4.1 Pass of patch test	19
1.4.2 Pass of zero energy mode test	22
1.5 Outline of the paper	25

Chapter 2. The new 4-node quadrilateral shell elements

2.1 The formulations of the developed 4-node quadrilateral shell elements	27
2.1.1 Basic 4-node quadrilateral shell element, MITC4	27
2.1.2 The MITC4+ shell element	30
2.1.3 The MITC4+N shell element	34
2.1.4 The new MITC4+ shell element	39
2.2 Basic tests	48
2.3 Convergence studies	54
2.3.1 Fully clamped square plate problem	55

2.3.2 Cylindrical shell problems	56
2.3.3 Hyperboloid shell problems	60
2.3.4 Spherical shell problems	63
2.4 Classical benchmark tests	67
2.4.1 Twisted beam problem	68
2.4.2 Pinched cylinder problem	69
2.4.3 Hemispherical shell problem	70
2.5 Geometric nonlinear analysis	72
2.5.1 Cantilever bending problem	72
2.5.2 Hemispherical shell problem	74
2.5.3 Bending of cylindrical shell structure	78
2.5.4 Twisted cantilever beam problem	81
2.6 Conclusions	82
Chapter 3. The new 6-node triangular solid-shell element	
3.1 The geometric nonlinear formulation of the developed 6-node triangular solid-shell element, MITC-S6	84
3.2 The previous 8-node quadrilateral solid-shell element, MITC-S8	91
3.3 Basic tests	93
3.4 Classical benchmark tests	94
3.4.1 Fully clamped square plate problem	95
3.4.2 Pinched cylinder problem	97
3.4.3 Twisted beam problem	100
3.4.4 Scordelis-Lo roof problem	102
3.4.5 Pressurized cylinder problem	103
3.5 Detailed convergence studies	105
3.5.1 Fully clamped square plate problem	106
3.5.2 Hyperboloid shell problems	108
3.6 Geometric nonlinear analysis	110
3.6.1 Cantilever under end shearing force	111
3.6.2 Pinched cylindrical shell	111
3.7 Conclusions	114
Chapter 4. Conclusions	115

References	117
Summary in Korean	129
Acknowledgements in Korean	131

List of Tables

Table 1.1. Comparison of techniques to remedy membrane locking	15
Table 1.2. Comparison of techniques to treat thickness locking	17
Table 2.1. Relative comparison of assembly time	47
Table 2.2. Vertical displacements at the center of tip A for Cook's problem	52
Table 2.3. Vertical displacements ($\times 10^{-4}$) at the tip A for cantilever problem	53
Table 2.4. Vertical displacements at the tip A for thick curved beam problem	53
Table 3.1. Normalized vertical deflections at the plate center (point A) for the clamped plate problem	97
Table 3.2. Normalized vertical deflections of the cylinder at point A	99
Table 3.3. Normalized deflections at the free end of the twisted beam in the direction of applied load	101
Table 3.4. Normalized vertical deflections at the center of free edge (point D) of the Scordelis-Lo roof problem	103

List of Figures

Fig. 1.1. Transverse displacement and coordinate in direction of bending	11
Fig. 1.2. Five in-plane modes of 4-node quadrilateral element	23
Fig. 1.3. Low-order continuum-mechanics based shell elements	24
Fig. 2.1. A standard 4-node quadrilateral continuum mechanics based shell element	28
Fig. 2.2. Tying positions (A), (B), (C) and (D) for the assumed transverse shear strain field of the MITC4 shell element	29
Fig. 2.3. Triangular subdivision of the mid-surface of the 4-node shell element	31
Fig. 2.4. Four triangles to determine the center point of the MITC4+ shell element	32
Fig. 2.5. Tying positions (A), (B), (C) and (D) for the assumed membrane strain field of the MITC4+ shell element	33
Fig. 2.6. The construction of center points	35
Fig. 2.7. Area coordinates (q_1 and q_2) used for the MITC4+N shell element	38
Fig. 2.8. The representative vectors from the element geometry	40
Fig. 2.9. Tying positions (A), (B), (C), (D) and (E) for the assumed membrane shear strain field	43
Fig. 2.10. Mesh geometry used for the patch tests	49
Fig. 2.11. Mesh geometry, loading and boundary conditions used for the membrane patch tests	49
Fig. 2.12. Stresses along lines L1 to L6 for the membrane patch tests of the MITC4+ shell element	51
Fig. 2.13. Cook's problem	52
Fig. 2.14. Cantilever problem	52
Fig. 2.15. Thick curved beam problem	53
Fig. 2.16. Fully clamped square plate under uniform pressure ($L = 1.0$, $E = 1.7472 \times 10^7$, $q = 1.0$ and $\nu = 0.3$)	56
Fig. 2.17. Distorted mesh patterns for (a) $N = 4$ and (b) $N = 8$	57
Fig. 2.18. Convergence curves for the fully clamped square plate problem with (a) the regular and (b) distorted meshes shown in Fig. 2.17	58
Fig. 2.19. Cylindrical shell problem ($L = R = 1.0$, $E = 2.0 \times 10^5$, $\nu = 1/3$ and $p_0 = 1.0$)	59
Fig. 2.20. Convergence curves for the clamped cylindrical shell problem with (a) the regular or (b) distorted meshes	60
Fig. 2.21. Convergence curves for the free cylindrical shell problem with (a) the regular and (b) distorted meshes	61

Fig. 2.22. Hyperboloid shell problem ($E = 2.0 \times 10^{11}$, $\nu = 1/3$, $L = 1.0$ and $p_0 = 1.0$)	62
Fig. 2.23. Convergence curves for the clamped hyperboloid shell problem with (a) the regular and (b) distorted meshes	63
Fig. 2.24. Convergence curves for the free hyperboloid shell problem with (a) the regular and (b) distorted meshes	64
Fig. 2.25. Spherical shell problem ($E = 2.0 \times 10^{11}$, $\nu = 1/3$, $R = 1.0$, $\phi_0 = 18^\circ$ and $p_0 = 1.0$)	65
Fig. 2.26. Convergence curves for the clamped spherical shell problem with (a) the regular and (b) distorted meshes	66
Fig. 2.27. Convergence curves for the free spherical shell problem with (a) the regular and (b) distorted meshes	67
Fig. 2.28. Twisted beam problem	68
Fig. 2.29. Convergence of the normalized vertical deflections for the twisted beam problem	69
Fig. 2.30. Pinched cylinder problem	70
Fig. 2.31. Convergence of the normalized vertical deflections for the pinched cylinder problem	70
Fig. 2.32. Hemispherical shell problem	71
Fig. 2.33. Convergence of the normalized vertical deflections for the hemispherical shell problem	71
Fig. 2.34. Cantilever bending problem (16×1 mesh)	72
Fig. 2.35. Load-displacement curves for the cantilever (a) under tip shearing force and (b) under tip moment	73
Fig. 2.36. Deformed shapes of the cantilever (a) under tip shearing force and (b) under tip moment	74
Fig. 2.37. Hemispherical shell problem	75
Fig. 2.38. Load-displacement curves for the hemispherical shell problem with the uniform mesh	76
Fig. 2.39. Load-displacement curves for the hemispherical shell problem with the distorted mesh	77
Fig. 2.40. Bending of cylindrical shell structure	78
Fig. 2.41. Load-displacement curves for the bending of cylindrical shell structure with the uniform mesh	79
Fig. 2.42. Load-displacement curves for the bending of cylindrical shell structure with the distorted mesh	80
Fig. 2.43. Twisted cantilever beam problem (4×24 mesh)	81
Fig. 2.44. Load-displacement curves for the twisted cantilever beam problem	82
Fig. 3.1. Nonlinear kinematics of the 6-node triangular solid-shell element	85
Fig. 3.2. A 6-node triangular solid-shell element	85

Fig. 3.3. Tying positions for the transverse shear strains of the MITC-S6 solid-shell element	87
Fig. 3.4. An 8-node quadrilateral solid-shell element	92
Fig. 3.5. Patch tests	94
Fig. 3.6. An element used for the constant compression test	94
Fig. 3.7. Fully clamped square plate problem	95
Fig. 3.8. Mesh patterns used for the benchmark tests	96
Fig. 3.9. Convergence of the normalized vertical deflections for the fully clamped square plate problem with (a) $t/L=1/100$, (b) $t/L=1/1000$ and (c) $t/L=1/10000$	98
Fig. 3.10. Convergence of the normalized vertical deflections for the pinched cylinder problem with the type 1 regular mesh shown in Fig. 3.8	99
Fig. 3.11. Twisted beam problem	100
Fig. 3.12. Convergence of the normalized deflections for the twisted beam problem with (a) in-plane and (b) out-of-plane load cases	101
Fig. 3.13. Scordelis-Lo roof problem	102
Fig. 3.14. Convergence of the normalized vertical deflections for the Scordelis-Lo roof problem with the type 1 regular mesh shown in Fig. 3.8	103
Fig. 3.15. Pressurized cylinder in plane strain condition	104
Fig. 3.16. Radial stresses across thickness of the pressurized cylinder	105
Fig. 3.17. Irregular mesh patterns used ($N = 4$) for (a) triangular and (b) quadrilateral elements	106
Fig. 3.18. Convergence curves for the fully clamped square plate problem with the (a) regular and (b) irregular mesh patterns shown in Fig. 3.17	107
Fig. 3.19. Convergence curves for the clamped hyperboloid shell problem with the (a) regular and (b) irregular mesh pattern shown in Fig. 3.17	109
Fig. 3.20. Convergence curves for the free hyperboloid shell problem with the (a) regular and (b) irregular mesh pattern shown in Fig. 3.17	110
Fig. 3.21. Load-displacement curve for the cantilever beam under end shearing force	111
Fig. 3.22. Deformed shapes at shear tip forces $P = 1.0, 2.0$ or 4.0 for the cantilever beam problem	112
Fig. 3.23. Pinched cylindrical shell	112
Fig. 3.24. Load-displacement curves for the pinched cylindrical shell	113
Fig. 3.25. Deformed shape at $P = 700$ for the pinched cylindrical shell	113

Chapter 1. Introduction

1.1 Introduction

Shells are beautiful and efficient structures that exist in nature and many engineering applications, but their inherently complicated behavior is not easy to predict. The Finite Element Method (FEM) has been very useful for the analysis of shell structures. For several decades, the development of effective shell elements has been of great interest [1-22]. More recently, there have been another approaches to analyze the shell structure, using schemes such as extended FEM [23,24] or isogeometric analysis [25-27]. However, in this paper, we focus on classical shell finite elements and remedying its deficiencies.

The low-order shell elements have minimum number of nodal unknowns and hence very efficient. Low-order quadrilateral shell elements are most widely used for its accurate predictive capability, while low-order triangular shell elements are frequently used because of its feasibility in modeling arbitrary shell structures. [6,28]. However, such low-order shell elements frequently suffer from different kinds of locking (shear, membrane and thickness locking) which prevent the solution to converge accurately. The main topic of this paper is to remedy membrane and thickness locking for some specific categories of classical shell finite elements.

A reliable shell finite element should satisfy mathematical condition such as ellipticity and consistency while giving stable convergence toward the reference solution, also known as the inf-sup condition. Such “ideal” shell elements should pass basic tests such as patch, zero energy mode, in-plane mode and isotropy tests. In addition, a uniformly optimal convergence should be shown through shell problems regardless of the kinds of asymptotic behavior (membrane-dominated, bending-dominated and mixed) which depends on the geometry, loading and boundary condition of the shell structures [15-22].

There are essentially three different approaches in formulating the shell element discretization. In the ‘superposition’ approach, the shell behavior is seen as a superposition of membrane and plate

bending actions. These ‘flat shell’ elements do not include the curvature effect and the plate bending and membrane behavior is coupled only at the nodal points. In the ‘theory based’ approach, element formulation is based on a specific shell theory. However, the finite element discretization requires nodal point variables appear on the derivatives in addition to the nodal displacements and rotations. If the shell theory is only applicable to certain shell geometries or analysis conditions, the finite element is subjected to the same restrictions. In the ‘continuum-mechanics based’ approach, very general finite element formulation which can be used for any types of analysis is obtained by degenerating the three-dimensional continuum to shell behavior [29].

The continuum-mechanics based approach results in two big categories of shell element discretization. In ‘solid-shell’ elements [30-42], nodes at the top and bottom surfaces remains and only internal formulation of the element is modified to account for shell behavior. Since it is enough to use only nodal translations in the displacement unknowns, solid-shell elements are often preferred in certain analysis types involving heavy computations, such as elasto-plastic analysis. In ‘degenerated shell’ elements [1,2,5-17,42], nodes are placed only at the mid-surface of the shell structure. These elements, frequently called as ‘shell’ elements, are most efficient and widely used while requiring both nodal translations and rotations in the nodal displacements.

In the present study, main efforts are devoted to the development of effective continuum-mechanics based shell elements. The two different types of low-order shell elements, 4-node quadrilateral shell and 6-node triangular solid-shell elements are developed.

1.2 Previous studies of low-order shell elements

In this section, we review previous studies of low-order quadrilateral and triangular shell elements, encompassing solid-, flat and degenerated shell elements.

1.2.1 Solid-shell elements

Firstly, we review the previous studies on the 8-node solid-shell elements.

There are many literatures on 8-node solid-shell elements which are close to the optimal element. Hauptmann et al. (1998) presented among the first 8-node quadrilateral solid-shell element [35]. Kemp et al. (1998) published assumed strain solid-shell element [43]. Klinkel et al. (1999) presented solid-shell element for laminated structure [33]. Hauptmann et al. (2000) applied solid-shell concept to large elasto-plastic deformations [44]. Sze et al. (2000,2002) applied hybrid stress and assumed stress techniques to solid-shell elements [36,37]. Harnau et al. (2002) presented element for large-deformation non-linear analysis [41]. Alves de Sousa et al. (2005) applied Enhanced Assumed Strain (EAS) and Assumed Natural Strain (ANS) on reduced integrated solid-shell element with stabilization [45]. Kim et al. (2005) applied resultant stress formulation to 8-node solid-shell element for increased efficacy in non-linear simulation [46]. Klinkel et al. (2006) also presented element for non-linear analysis [32]. Cardoso and Yoon et al. (2008) applied EAS, ANS and ‘area coordinate method’ on development of solid-shell element with one-point integration with stabilization [47]. Kulikov et al. (2008) [48] applied geometrically exact formulation of Simo et al. (1989) [49] into solid-shell with seven D.O.Fs per node. Schwarze et al. (2009) applied EAS and ANS method to develop solid-shell element with reduced integration and stabilization [34].

Secondly, we review the previous studies on the 6-node solid-shell elements.

There have been relatively few literatures on 6-node triangular solid-shell elements. Sze et al. (2001) developed a 6-node pentagonal solid-shell element by using the ANS technique for shear locking and the ‘modified laminated stiffness matrix’ for thickness locking [30]. Flores (2013) developed a 6-node solid-shell element by applying the ANS technique for shear locking and the EAS technique for thickness locking [31]. Those two elements passed all the basic tests, but we remark that convergence tests were not sufficient. Sze et al. tested the convergence of displacements on several linear benchmark problems focusing on coarse-meshes [30]. The element by Flores lacks linear tests to fully see the convergence behavior, especially for the thin shell cases [31]. Trinh VD et al. (2010) presented a 6-node solid-shell element using assumed strain projection method, but pass of basic tests were not considered [50]. In our study, we aim to show the convergence performance of the newly developed solid-shell element from coarse to fine meshes over shell problems with various curvatures encompassing a practical range of shell thickness (ratio of thickness to overall dimension, $t/L = 1/100 \sim 1/10000$).

1.2.2 Flat shell elements

Firstly, we review the previous studies on the 4-node flat shell elements.

Many literatures considered flat shell element with 6 DOFs (Degrees of Freedom) per node and warping correction. Bathe and Ho (1981) developed flat shell element by superimposing membrane element and plate bending elements [51]. Ibrahimbegovic and Wilson (1991) presented unified formulation for triangular or quadrilateral flat shell element [52]. Aminpour (1992) applied assumed stress hybrid method to the flat shell element [53]. Cook (1994) studied and reviewed the use of drilling degrees of freedom on flat shell element having warped geometry [54]. Groenwold et al. (1995) applied assumed strain method and modified drilling degrees of freedom and 5-point quadrature rule to obtain the flat shell element [55]. Kim and Lee et al. (1998) applied assumed strain method and Allman-type modification on displacements of flat shell regarding membrane locking [56]. Choi and Lee et al. (1999) applied higher order modes, 5-point integration with warping correction on the flat shell element [57]. Choi and Lee et al. (2003) used various non-conforming modes on the flat shell elements regarding the membrane locking [58].

First limitation of the literatures of flat shell are, that they use warping correction (or ‘rigid-link correction’) by Taylor (1987) [59]. Because it is forcibly applied to the geometry to project elements into flat shapes, it tends to decrease the performance of the element in general distorted cases, as pointed out by Groenwold et al. [55]. Secondly, although separation of membrane and bending is simplest and actual physical nature of flat shell structures, it does not correctly account for the membrane-bending coupling which naturally arises for general curved shell structures. Adding the coupling between membrane and bending, and also further including Reissner-Mindlin theory was studied by Cook [54], but it is hard to manipulate all the (separated) membrane, bending and the coupled parts in a way to make optimally converging element.

Secondly, we review the previous studies on the 3-node flat shell and plate bending elements.

Batoz et al. (1980) studied one of the first 3-node plate bending elements [60]. Fricker (1985) improved the bending performance of the element by inclusion of cubic order of shape function [61].

Auricchio et al. (1994) developed a plate bending element with cubic bubble shape function applied only to the two internal ‘rotation’ DOFs [62]. Argyris et al. (1994) developed a flat shell element based on assumed Natural Mode Method (NMM) [63]. Despite the fact that NMM has huge potential in improving the behavior of the elements, the formulation is relatively complex to be implemented. All the plate bending and flat shell element discussed above did not show uniformly optimal convergence behavior regarding shear locking. Onate et al. (2000) presented a set of flat triangular elements without rotation DOFs, but the computations external to the element domains were required [64].

1.2.3 Degenerated shell elements

In this section, we review the previous studies on the 4-node degenerated shell elements.

One major sub-category is related to reduced-integration with stabilization. Work by Belytschko, Tsay and Liu (1981) is one of the first to apply reduced integration and stabilization on the shell element [65]. Hughes and Liu (1981) consequently developed another one-point quadrature shell [66]. Belytschko and Tsay (1983) presented a stabilization procedure for plate element [67]. Belytschko et al. (1984) showed usefulness of one-point quadrature shell on explicit, nonlinear dynamics [68]. Belytschko et al. (1992) applied warping correction to the Belytschko-Tsay or Hughes-Liu shell element [69]. Belytschko and Leviathan (1994) developed new physical stabilization procedure so that the element passes patch test [70]. Zhu et al. (1996) developed new one-point quadrature shell element with drilling DOFs [71]. Kim et al. (2003) applied assumed strain hybrid method with quasi-conforming modes to develop shell element with 6 DOFs per nodes [72].

One clear disadvantage of reduced integration with stabilization is that it requires empirical parameter, the control parameter for hourglass stabilization. Using the physical stabilization [70], one can obtain the hourglass stiffness with no parameters, but the framework of stabilization still requires the control parameter. Second disadvantage of reduced integration with stabilization is that it requires projection on displacements [73] to express correct rigid body modes for the warped geometry of the 4-node shell elements. For general 4-node shell elements, this mingles the physical nature of translation and rotation DOFs and thus affecting the physical nature of the shell solutions. Thus,

although it may obtain convergent behavior in some tests, it is hard to satisfy convergence in strict sense: such as accurate convergence of all of displacement, strain and stress combined measured using s-norm [18].

Another major sub-category is related to mode-increasing technique of Enhanced Assumed Strain/Stress (EAS) formulation, which is usually used in conjunction with other types of techniques. Lee et al. (1978) studied improvement on shell finite elements using mixed formulation such as EAS or ANS [74]. Andelfinger and Ramm (1993) developed several EAS elements and showed the equivalence to elements formulated by the Hellinger-Reissner functional [75]. Bischoff and Ramm (1997) combined both EAS and ANS techniques to shell elements [76]. Witkowski (2009) applied semi-EAS-ANS method to 6 parameter shell element [77].

Disadvantage of the EAS formulation is that the increased performance is directly related to the increased computational cost, the assembly cost of the elements. For the membrane locking problem, element behavior is improved as more higher-order terms are involved using the EAS technique, because the higher-order terms guarantee higher rates of convergence. However, this is not effective than finding the method to eliminate the cause of the membrane locking on the 4-node shell element without highly increasing the assembly cost. Most importantly, the error due to locking overruns the increased accuracy as thickness is decreased.

Another sub-category is related to hybrid stress/strain or Assumed Stress Hybrid (ASH) technique. Rengarajan et al. (1995) published assumed-stress hybrid shell element with drilling DOFs for linear stress, buckling and free vibration analysis [78]. Sze et al. (1997) published hybrids stress quadrilateral shell element with full rotational DOFs per node [79]. Sansour et al. (2000) studied families of 4-node or 9-node elements with hybrid stress/strain formulation, with no successful result in patch tests [80]. Regarding the membrane part, Cen et al. (2011) [81] derived hybrid stress-function plane element with drilling DOFs extending the original work by Pian (1964) [82].

One disadvantage of the hybrid stress/strain formulation is that it does not always yield a symmetric stiffness matrix. This is due from that it is required to modify specifically the stress or the strain only (and not the other one) in some hybrid stress/strain formulation. Another disadvantage is that higher performance comes from increased number of internal parameters in assuming the

stress/strain.

Another important category is assumed strain or related method, such as the Mixed Interpolation of Tensorial Components (MITC), ANS or Discrete Shear/Strain Gap (DSG) methods. Dvorkin and Bathe (1984) applied the MITC method on the 4-node shell element to obtain both efficient and accurate element, the MITC4 shell element [1]. This method of treatment of shear locking has been used extensively along with other techniques, such as assessed by Stander et al. (1989) for finite rotation shell analysis [83]. Choi and Paik (1994) applied the assumed strain method on the membrane part of degenerated shell element to successfully remove the membrane locking while failing the patch test [2]. Koschnick et al. (2005) applied the DSG method for treating membrane locking of quadrilateral elements, but the basic test was not passed for the 4-node shell element [84]. Vampa (2007) [85] developed new MITC shell element by applying QMITC membrane element [86] to in-plane strains of the MITC4 shell element. While the resulting element satisfies basic tests and obtains improved convergence behaviors, the behavior was not perfectly uniformly optimal and the formulation was rather costly computationally.

Secondly, we review the previous studies on the 3-node degenerated shell elements, which pass all the basic tests including isotropy, patch and zero energy mode tests.

Indeed, there are few elements which pass all the basic tests. Argyris et al. (1994) developed triangular shell element based on NMM technique, with improved performance in sake of complexity in formulation [87]. Further improvement in performance was obtained by Lee et al. (2014) [7] which included cubic bubble function for two internal rotation as well as developing new assumed transverse shear strain, based upon the earlier works by Lee et al. (2004) [6]. The resulting element was named MITC3+ shell element. For the shear locking treatment in triangular elements, the techniques used in degenerated shell element can be applied to other types (solid-shell, plate bending and flat shell) of elements and vice versa.

1.3 Type of locking and its treatments

Satisfying the inf-sup condition means behavior of the shell elements converging toward the refer-

ence solution is “uniformly optimal” regardless of the problems considered. That is, the solution error must diminish optimally independent of the shell thickness as the mesh is refined [15-22]. In achieving such behaviors, the major obstacles are shear, membrane and thickness locking.

Shear locking in 4-node quadrilateral and 3-node triangular shell elements have been treated successfully using the MITC (Mixed Interpolation of Tensorial Components) method [1,5-14,31-33], also known as ‘assumed strain’ or ANS (Assumed Natural Strain) method [30,34-42,88-90]. Particularly, the convergence behavior of the 4-node MITC shell element (MITC4) [1] and 3-node MITC shell element (MITC3+) [7] are observed to be close to uniformly optimal due to its effective shear locking treatments. The approach of the MITC4 shell element has been successfully applied to 8-node quadrilateral solid-shell elements [32-37,41]. On the other hand, optimally convergent 6-node triangular solid-shell elements are yet to be found [30,31].

There have been several attempts to alleviate membrane locking of 4-node continuum mechanics based shell elements. Those attempts are sometimes confused with improving the membrane behavior of the shell elements. It is extremely difficult to design an ideal 4-node shell element with reduced membrane locking in bending-dominated problem but having membrane performances retained.

First, disambiguation with “improving the membrane performance” is presented. Improved membrane behavior can slightly delay the emergence of error caused by membrane locking. However, the membrane locking is the phenomenon induced by mesh distortion in case of pure in-extensional bending behavior [91]. As the thickness is decreased, the locking occurs more severely, and hence the error due to the locking mechanism grossly overruns the solution accuracy. The treatments that improve the membrane behavior but do not directly affect membrane locking include ‘drilling degree of freedom’ [51-59] or ‘enhanced assumed strain’ [45,47,92,93].

The techniques improving the performance in bending dominated problems are most important for reducing membrane locking. Reduced integration technique [67,70,73] can greatly alleviate membrane locking, but the elements suffer from rank deficiency and do not properly represent physical rigid body modes, needing undesirable stabilization and displacement projection techniques. Various assumed strain methods were applied to the membrane strains (in-plane strains evaluated at the mid-

surface) to alleviate membrane locking while satisfying the basic tests, but the convergence are not uniformly optimal or vice versa [2-5,84,85].

Thickness locking in low-order solid-shell elements has been effectively reduced by the EAS (Enhanced Assumed Strain) technique [30-34,41]. Compared with the other methods such as ‘plane stress condition’ [35], ‘hybrid stress’ [36] or ‘modified laminated stiffness matrix’ [30,37], the method provides full coupling between membrane and bending behaviors and the fully general constitutive law can be directly used.

In the present study, major research aims are developing new 4-node quadrilateral shell element by reducing membrane locking, and making 6-node quadrilateral solid-shell element based on the 3-node triangular shell element (MITC3+) by alleviating thickness locking.

1.3.1 The membrane locking problem

In this section, membrane locking problem is defined, and previous studies on the membrane locking are reviewed.

The membrane locking problem has been discussed in many literatures, but sometimes its usage was mixed with other type of problem. The first type is the one which occurs for 3-node beam, 9-node shell elements or 4-node shell elements with curved geometries, on the bending problem with the transverse loadings. The second type is simply named from the deteriorated performance of the in-plane (membrane) problems for some finite elements, which are tested for the flat case of the shell elements. In our study, the problem to be remedied is the first type, which is more important for the structural (shell or beam) elements which are designed for effective analysis of the bending problems.

The membrane locking problem has been studied through various finite elements. Prathap et al. (1982) studied the problem on the 3-node beam element and applied the reduced integration or the assumed strain method [94]. Stolarski et al. (1982) applied reduced integration on the beam element [95]. Stolarski et al. (1983) theoretically studied membrane locking on curved C0 beam element [96]. Belytschko et al. (1985) studied the 9-node shell element and applied the stress projec-

tion method on the 9-node shell element [97]. Pitkäranta J (1992) theoretically studied the membrane locking on the cylindrical shell problem [98]. Bucalem et al. (1993) studied the 9-node shell element and applied the assumed strain method [99]. Choi and Paik (1994) studied the 4-node shell element and applied the assumed strain method, although the element did not satisfy consistency condition (patch test) [2]. Belytschko et al (1994) applied the physical stabilization on the reduced integrated 4-node shell element, but the basic membrane behavior and possibly bending behavior was deteriorated, while the stabilization also requiring control parameter [70]. Koschnick et al. (2005) applied the discrete strain gap method on the 4-node and the 9-node shell elements, but membrane patch test was not passed for the 4-node shell element [84]. In summary, the membrane locking on the 4-node shell element with generally warped (curved and distorted) geometry was neither theoretically studied nor successfully removed.

1.3.2 Mathematical derivation of the cause of membrane locking

The purpose of this section is to determine the part of membrane strain of the degenerated 4-node shell element which causes membrane locking, in order to aid in the subsequent development of the 4-node shell element. This study is in accordance with the previous studies on membrane locking problem [10,91,98,99], but extended to general warped and distorted 4-node shell element.

In the thin-shell limit, bending strain energy from Kirchhoff's plate theory (bending behavior in Kirchhoff's hypothesis) [15,60,63,87,91] becomes dominant, which is proportional to the second order derivative of transverse translational displacement in direction of physical bending. This condition is often called 'Kirchhoff limit', and the bending behavior sometimes 'Kirchhoff bending'.

Let us define mid-surface coordinates and mid-surface covariant base vectors of each element

$$\mathbf{x}_m = \sum_{i=1}^4 h_i(r,s) \mathbf{x}_i, \quad (1.1)$$

$$\mathbf{a}_i = \frac{\partial \mathbf{x}_m}{\partial r_i} \quad \text{with } i=1,2, \quad (1.2a)$$

$$\mathbf{a}_3 = \mathbf{a}_1(r,s) \times \mathbf{a}_2(r,s) / \|\mathbf{a}_1(r,s) \times \mathbf{a}_2(r,s)\|. \quad (1.2b)$$

Here \mathbf{a}^1 and \mathbf{a}^2 denote the mid-surface contravariant bases such that $\mathbf{a}_i \cdot \mathbf{a}^j = \delta_{ij}$ in which δ_{ij} is the Kronecker delta, and $\mathbf{a}^i_{,j} = \frac{\partial \mathbf{a}^i}{\partial r_j}$.

Within each element, let us set up in-plane, orthogonal coordinate directions shown in Fig. 1.1 defined by unit vectors \mathbf{e}_L and \mathbf{e}_M , and the corresponding coordinates L and M , such that one of the direction corresponds to physical bending, say \mathbf{e}_L .

$$L\mathbf{e}_L + M\mathbf{e}_M + t\mathbf{a}_3 = r\mathbf{a}_1 + s\mathbf{a}_2 + t\mathbf{a}_3, \quad (1.3)$$

$$\text{in which } \mathbf{e}_L \cdot \mathbf{e}_M = 0, \quad \mathbf{e}_L \cdot \mathbf{a}_3 = 0, \quad \mathbf{e}_M \cdot \mathbf{a}_3 = 0. \quad (1.4)$$

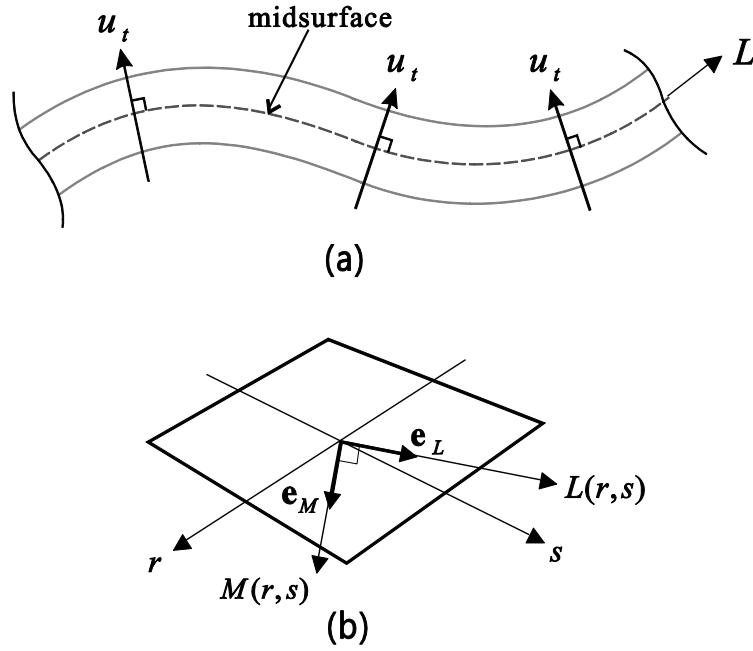


Fig. 1.1. Transverse displacement and coordinate in direction of bending. The transverse displacement (u_t) normal to the mid-surface of the shell is shown in (a). The coordinate in direction of bending (L) on the mid-surface of the shell can be described in terms of the natural coordinates within each element, as shown in (b).

Dominant bending strain $\frac{\partial^2 u_t(r,s)}{\partial L^2}$ in Kirchhoff limit can be expanded as follows,

$$\frac{\partial^2 u_t(r,s)}{\partial L^2} = (\mathbf{e}_L \cdot \mathbf{a}^1)^2 \frac{\partial^2 u_t(r,s)}{\partial r^2} + (\mathbf{e}_L \cdot \mathbf{a}^2)^2 \frac{\partial^2 u_t(r,s)}{\partial s^2} + 2(\mathbf{e}_L \cdot \mathbf{a}^1)(\mathbf{e}_L \cdot \mathbf{a}^2) \frac{\partial^2 u_t(r,s)}{\partial r \partial s}$$

$$\begin{aligned}
& + \left[(\mathbf{e}_L \cdot \mathbf{a}^{1,1})(\mathbf{e}_L \cdot \mathbf{a}^1) + (\mathbf{e}_L \cdot \mathbf{a}^{1,2})(\mathbf{e}_L \cdot \mathbf{a}^2) \right] \frac{\partial u_t(r,s)}{\partial r} \\
& + \left[(\mathbf{e}_L \cdot \mathbf{a}^{2,1})(\mathbf{e}_L \cdot \mathbf{a}^1) + (\mathbf{e}_L \cdot \mathbf{a}^{2,2})(\mathbf{e}_L \cdot \mathbf{a}^2) \right] \frac{\partial u_t(r,s)}{\partial s}, \tag{1.5}
\end{aligned}$$

in which \mathbf{a}_1 and \mathbf{a}_2 are the mid-surface covariant bases in Eq. (1.2a), which are further decomposed as

$$\mathbf{a}_1 = \sum_{k=1}^4 \frac{\partial h_k}{\partial r} \mathbf{x}^k = \mathbf{A}_1 + \mathbf{A}_3 s, \tag{1.6a}$$

$$\mathbf{a}_2 = \sum_{k=1}^4 \frac{\partial h_k}{\partial s} \mathbf{x}^k = \mathbf{A}_2 + \mathbf{A}_3 r, \tag{1.6b}$$

where \mathbf{A}_1 , \mathbf{A}_2 and \mathbf{A}_3 are geometry constants independent of natural coordinates (r , s and t).

As the mesh is refined on the curved surface, following conditions emerge,

$$\|\mathbf{a}^i\| \gg \|\mathbf{a}^{i,j}\|, \tag{1.7}$$

$$\|\mathbf{a}_1(r,s) \times \mathbf{a}_2(r,s)\| = \|(\mathbf{A}_1 + \mathbf{A}_3 s) \times (\mathbf{A}_2 + \mathbf{A}_3 r)\| \approx \|\mathbf{A}_1 \times \mathbf{A}_2\| = \|\mathbf{a}_1(0,0) \times \mathbf{a}_2(0,0)\|. \tag{1.8}$$

For the 4-node degenerated quadrilateral shell element global displacements are interpolated bilinearly in the natural coordinates,

$$\mathbf{u}(r,s) = \sum_{k=1}^4 h_k(r,s) \mathbf{u}^k = \mathbf{B}_0 + \mathbf{B}_1 r + \mathbf{B}_2 s + \mathbf{B}_3 rs, \tag{1.9}$$

Where \mathbf{B}_0 , \mathbf{B}_1 , \mathbf{B}_2 and \mathbf{B}_3 are displacement constants independent of natural coordinates.

Following the Ref. [100], covariant displacements can be written as the following,

$$u_r(r,s) = (\mathbf{A}_1 + \mathbf{A}_3 s) \cdot (\mathbf{B}_0 + \mathbf{B}_1 r + \mathbf{B}_2 s + \mathbf{B}_3 rs), \tag{1.10}$$

$$u_s(r,s) = (\mathbf{A}_2 + \mathbf{A}_3 r) \cdot (\mathbf{B}_0 + \mathbf{B}_1 r + \mathbf{B}_2 s + \mathbf{B}_3 rs), \tag{1.11}$$

$$u_t(r,s) = \left[(\mathbf{A}_1 + \mathbf{A}_3 s) \times (\mathbf{A}_2 + \mathbf{A}_3 r) \cdot (\mathbf{B}_0 + \mathbf{B}_1 r + \mathbf{B}_2 s + \mathbf{B}_3 rs) \right] / \left\| (\mathbf{A}_1 + \mathbf{A}_3 s) \times (\mathbf{A}_2 + \mathbf{A}_3 r) \right\|. \tag{1.12}$$

Using Eq. (1.8), covariant displacements in the Eqs. (1.10) to (1.12) are further expressed as the following,

$$u_r(r, s) = C_0 + C_1 r + C_2 s + C_3 r s + C_4 s^2 + C_5 r s^2, \quad (1.13)$$

$$u_s(r, s) = D_0 + D_1 r + D_2 s + D_3 r^2 + D_4 r s + D_5 r^2 s, \quad (1.14)$$

$$u_t(r, s) = E_0 + E_1 r + E_2 s + E_3 r^2 + E_4 r s + E_5 s^2 + E_6 r^2 s + E_7 r s^2, \quad (1.15)$$

in which constants which depends on both geometry and displacements, C_i ($i = 0, \dots, 5$), D_i ($i = 0, \dots, 5$), and E_i ($i = 0, \dots, 7$) are implicitly introduced. Note that those constants are essentially contains nodal unknowns or DOFs.

Following the notation in the Ref. [100], membrane strains of 4-node quadrilateral shell element are expressed as,

$$\gamma_{rr}(r, s) = u_{r,r}, \quad (1.16)$$

$$\gamma_{ss}(r, s) = u_{s,s}, \quad (1.17)$$

$$\gamma_{rs}(r, s) = \frac{1}{2}(u_{r,s} + u_{s,r}) - \Gamma_{12}^1 u_r - \Gamma_{12}^2 u_s - b_{12} u_t. \quad (1.18)$$

By enforcing the pure in-extensional bending as in the Ref. [91], i.e. vanishing strain energy from the membrane strains in Eqs. (1.16) to (1.18), following conditions are obtained:

$$\begin{aligned} C_1 &\rightarrow 0, \quad C_3 \rightarrow 0, \quad C_5 \rightarrow 0, \\ D_2 &\rightarrow 0, \quad D_4 \rightarrow 0, \quad D_5 \rightarrow 0, \\ C_2 + D_1 - 2\Gamma_{12}^1 C_0 - 2\Gamma_{12}^2 D_0 - 2b_{12} E_0 - 2/3(\Gamma_{12}^2 D_3 + b_{12} E_3 + \Gamma_{12}^1 C_4 + b_{12} E_5) &\rightarrow 0, \\ 2D_3 - 2\Gamma_{12}^2 D_1 - 2b_{12} E_1 - 2/3(b_{12} E_7) &\rightarrow 0, \\ 2C_4 - 2\Gamma_{12}^1 C_2 - 2b_{12} E_2 - 2/3(b_{12} E_6) &\rightarrow 0, \\ E_4 &\rightarrow 0, \\ \Gamma_{12}^2 D_3 + b_{12} E_3 &\rightarrow 0, \\ \Gamma_{12}^1 C_4 + b_{12} E_5 &\rightarrow 0, \\ E_6 &\rightarrow 0, \\ E_7 &\rightarrow 0. \end{aligned} \quad (1.19)$$

If the conditions obtained involve only single term of unknowns, then it acts to ‘constrain’ the corresponding DOFs [91]. Those conditions, which can either slow down the convergence or prevent the expression of physical behaviors, are named ‘spurious constraints’, while those involving two or more terms of unknowns are named actual ‘physical constraints’. In this case, total of nine spurious constraints appear on in-extensional deformation, and one ($E_4 \rightarrow 0$) is related to the membrane

locking problem as discussed next.

From the Eqs. (1.5) and (1.15) the following three dominant terms for representation of Kirchhoff bending are obtained:

$$\frac{\partial^2 u_t(r, s)}{\partial r^2} = E_3, \quad (1.20)$$

$$\frac{\partial^2 u_t(r, s)}{\partial s^2} = E_5, \quad (1.21)$$

$$\frac{\partial^2 u_t(r, s)}{\partial r \partial s} = E_4. \quad (1.22)$$

From the Eq. (1.19) notice that the constraint $E_4 \rightarrow 0$ is enforced as shell thickness decreases, this prevents the pure bending with regard to the Eq. (1.22). This shows that basic displacement-based quadrilateral interpolation as in Eq. (1.1) suffers from the membrane locking. Furthermore, inspecting the Eqs. (1.13) and (1.15) reveals the following relation

$$E_4 \propto \mathbf{A}_1 \times \mathbf{A}_2 \cdot \mathbf{B}_3 + \mathbf{A}_1 \times \mathbf{A}_3 \cdot \mathbf{B}_2 + \mathbf{A}_3 \times \mathbf{A}_2 \cdot \mathbf{B}_1. \quad (1.23)$$

Notice from Eq. (1.23) that if displacement and geometry interpolation does not involve bi-linear (rs) term, \mathbf{A}_3 and \mathbf{B}_3 disappears and the locking-causing unknown constant (E_4) and the spurious constraint ($E_4 \rightarrow 0$) does not appear. However, in a common 4-node quadrilateral element, that part is necessary to correctly represent in-plane bending behavior.

1.3.3 Previous treatments of membrane locking

In this section, we deal with previous treatments of membrane locking of 4-node quadrilateral shell element.

Table 1.1. Comparison of techniques to remedy membrane locking.

Techniques	Strength	Weakness
Reduced integration with stabilization	-Reduced integration itself is a very powerful tool for removing the locking, as well as decreasing the computational cost	-Stabilization of stiffness matrix require control parameter (Hourglass control), which is purely empirical -Convergence on bending problems is not always guaranteed using the displacement projection, which is necessary for representing the physical rigid body modes
Enhanced Assumed Strain	-Able to introduce higher-order modes on the low-order elements so that element performance is better	-The technique delays (does not eliminate) the happening of membrane locking -Cost of statically condensing out the internal parameters is increased, for introducing the more modes
Assumed Stress(Strain) Hybrid	-Able to reformulate stress(strain) so that element performance is better	-The technique delays (does not eliminate) the happening of membrane locking -Cost of calculating the stress(strain) is increased, as more parameters are used Stiffness matrix is not always symmetric
Assumed strain methods (Assumed Natural Strain, Mixed Interpolation of Tensorial Components, Discrete Strain Gap)	-Able to modify the locking mechanism (for an element possibly performing better) without high additional computational cost	-Using this method, pass of basic tests related to consistency are affected (for example, it is not easy to pass the patch test).

In Table 1.1, we showed strength and weakness of the various techniques to remedy membrane locking. Reduced integration is powerful for both eliminating the locking and decreasing the computational cost, but require control parameter and bending convergence is not always guaranteed in general mesh (if physical rigid body modes are correctly expressed). EAS and ASH techniques are similar in that it is easy to make an accurate element in the expense of increasing the computational cost. However, such techniques frequently delays the occurrence of locking, not providing the fundamental solution. Assumed strain methods are not always successful, and pass of basic tests are easily affected. However, it has high potential that the method can potentially eliminate locking without high additional computational cost, which suits our goal of research.

1.3.4 Previous treatments of thickness locking

In this section, we review previous treatments of thickness locking.

There are two kinds of thickness locking: Poisson thickness (or thickness) locking and curvature thickness (or trapezoidal) locking [30-37,41,42,76]. Poisson thickness locking predominantly deteriorates the solution accuracy of solid-shell elements whenever Poisson's ratio is not equal to zero. Curvature thickness locking occurs for curved shell structures when mid-surface normal directions are naturally distorted within solid-shell element models.

Table 1.2. Comparison of techniques to treat thickness locking.

Techniques	Strength	Weakness
Enhanced Assumed Strain	-General three-dimensional constitutive law can be used -Full coupling between membrane and bending behavior can be retained	-Additional unknown is necessary (Increase of computational cost can be minimized by using ‘static condensation’ onto the added DOF)
Enforcement of plane-stress condition	-Simplest method for alleviating thickness locking	-Coupling between membrane and bending behavior is lost
Hybrid Stress method	-Able to reformulate stress(strain) so that element performance is better	-Cost of calculating the stress(strain) is increased, as more parameters are used -Stiffness matrix is not always symmetric -Applying the general constitutive law is involved
Modified generalized laminated stiffness	-Able to modify the locking mechanism (for an element possibly performing better) without high additional computational cost	-Application of general constitutive law is involved -In the stiffness matrix (i.e. the internal virtual work) the coupling of strain energy between thickness normal component and the other components is lost

In Table 1.2, we showed strength and weakness of the various techniques to treat thickness locking. We regard a reliable element to be generally applicable for any types of material law or shell behaviors. Regarding the comparison of various methods in Table 1.2, the EAS method is attractive if additional unknown can be condensed out, keeping the increase of the computational cost at minimum.

1.4 Basic requirements and basic tests

Here the basic requirements of shell elements are presented along with the methods of testing each of the requirements (by the basic tests).

Shell elements should satisfy the isotropy or spatial invariance. This means shell elements should yield identical results for all orientations formed by rigid body motion of the same configuration, and yield identical results for different nodal numberings. This isotropy is important for both triangular and curved quadrilateral shell elements [3,5-9,38].

The ellipticity of the elements directly require that the stiffness matrix to be positive definite. This means that energy stored in the element due to deformations should be positive. Also, symmetry between strains and stresses are also important. In computational sense, this means the resulting matrix is symmetric hence only about half of the matrix needs to be stored during the solution process. Practically this also implies that strains and stresses are directly related to each other by constitutive relation. Disparate treatments of stresses from strains, such as in ‘hybrid stress’ method [36,37,78-82], are avoided at best for direct usage of general constitutive law.

For the elements to be applicable to dynamic analysis, and also not to cause loss in deformation energy in static analysis, zero energy mode tests should be passed. In zero energy mode tests, only six zero energy modes corresponding to the physical rigid body modes should appear in the stiffness matrix of the elements [1,5-9,14,19,31,35,38-40]. For quadrilateral shell elements, the counted zero energy modes are sometimes not the physical rigid body modes that depend on the element geometry. Especially, using the ‘reduced integration’ technique applied to curved 4-node quadrilateral shell element [67,70,73], multiplication of the six rigid body modes to the both sides of the stiffness matrix does not yield zero values as desired.

The consistency condition requires for the elements to satisfy the patch tests [101]. This test is often considered to guarantee the convergence of the finite elements, providing mean to test stability. The patch of elements is subjected to the minimum number of constrains to prevent rigid body motions and the nodal point forces on the boundary corresponding to the constant stress states are applied. The patch tests are passed if the correct values of constant stress fields are calculated for any loca-

tions within the mesh. For shell elements, there are three kinds of patch tests, membrane, bending and shearing patch tests, according to the loading and boundary conditions [1,5-9,14,19,30-34,36-40,102].

Final requirement is simplicity of formulation and computation. The formulation itself need to be physically meaningful and easy to understand, and hence can be simply implemented [10,13,14]. Even though some increase in computation time is sometimes inevitable, it is best to keep it at minimum. Especially, keeping the of number of unknowns the same by using static condensation applied to added degrees of freedom is highly desirable [15].

1.4.1 Pass of patch tests

Here we discuss in more detail with the pass of patch tests. Among low-order shell elements, it is far more difficult to attain a consistent quadrilateral, rather than triangular, shell element passing the patch tests. Among different kinds of strains, membrane, bending and transverse shearing strains within the shell element, the membrane strains are the ones related to membrane locking of 4-node quadrilateral shell elements. However, there are no given ways to satisfy the membrane patch tests for quadrilateral elements. Here, we give detailed condition for quadrilateral elements to pass the patch tests.

Interpolation of 4-node quadrilateral element is given by

$$\mathbf{x}(r, s, t) = \sum_{i=1}^4 h_i(r, s) \mathbf{x}_i, \quad (1.24)$$

where $h_i(r, s)$ is the two-dimensional interpolation function of the standard isoparametric procedure corresponding to node i , \mathbf{x}_i is the position vector of node i in the global Cartesian coordinate system.

The corresponding displacement interpolation of the element is

$$\mathbf{u}(r, s, t) = \sum_{i=1}^4 h_i(r, s) \mathbf{u}_i, \quad (1.25)$$

in which \mathbf{u}_i is the nodal displacement vector in the global Cartesian coordinate system.

The linear terms of the displacement-based covariant strain components are given by

$$e_{ij} = \frac{1}{2}(\mathbf{g}_i \cdot \mathbf{u}_{,j} + \mathbf{g}_j \cdot \mathbf{u}_{,i}), \quad (1.26)$$

in which

$$\mathbf{g}_i = \frac{\partial \mathbf{x}}{\partial r_i}, \quad \mathbf{u}_{,i} = \frac{\partial \mathbf{u}}{\partial r_i} \quad \text{with } r_1 = r, \quad r_2 = s. \quad (1.27)$$

For transforming the strains we define contravariant bases,

$$\mathbf{g}^i = \frac{\partial r_i}{\partial \mathbf{x}} \quad \text{with } \mathbf{g}^i \cdot \mathbf{g}_j = \delta_j^i. \quad (1.28)$$

In the two-dimensional case we define following geometry and displacements in terms of global Cartesian coordinate system

$$\mathbf{x} = x_i \mathbf{i}_i = x \mathbf{i}_x + y \mathbf{i}_y, \quad \mathbf{u} = u_i \mathbf{i}_i = u \mathbf{i}_x + v \mathbf{i}_y \quad \text{with } \mathbf{i}_1 = \mathbf{i}_x, \quad \mathbf{i}_2 = \mathbf{i}_y, \quad (1.29)$$

in which \mathbf{i}_x and \mathbf{i}_y are unit vectors in global x and y directions, respectively.

The covariant strain components in Eq. (1.26) can be transformed into global strains by

$$\begin{aligned} \bar{e}_{ij} &= e_{kl} (\mathbf{i}_i \cdot \mathbf{g}^k) (\mathbf{i}_j \cdot \mathbf{g}^l) \\ &= e_{rr} \frac{\partial r}{\partial x_i} \frac{\partial r}{\partial x_j} + e_{ss} \frac{\partial s}{\partial x_i} \frac{\partial s}{\partial x_j} + e_{rs} \frac{\partial r}{\partial x_i} \frac{\partial s}{\partial x_j} + e_{rs} \frac{\partial r}{\partial x_j} \frac{\partial s}{\partial x_i} \\ &= \frac{1}{2} \left(\frac{\partial u_i}{\partial x_j} + \frac{\partial u_j}{\partial x_i} \right). \end{aligned} \quad (1.30)$$

In order to pass the membrane patch tests, following ‘constant strain conditions’ from Eq. (1.30) must be expressed:

$$\begin{aligned} \bar{e}_{xx}(u = x, v = 0) &= 1, \quad \bar{e}_{yy}(u = x, v = 0) = 0, \quad \bar{e}_{xy}(u = x, v = 0) = 0, \\ \bar{e}_{xx}(u = 0, v = y) &= 0, \quad \bar{e}_{yy}(u = 0, v = y) = 1, \quad \bar{e}_{xy}(u = 0, v = y) = 0, \\ \bar{e}_{xx}(u = y, v = x) &= 0, \quad \bar{e}_{yy}(u = y, v = x) = 0, \quad \bar{e}_{xy}(u = y, v = x) = 1, \end{aligned} \quad (1.31)$$

We are able to reverse the transformation relations in Eq. (1.30) as

$$e_{ij} = \bar{e}_{kl} (\mathbf{g}_i \cdot \mathbf{i}_k) (\mathbf{g}_j \cdot \mathbf{i}_l)$$

$$= \bar{e}_{xx} \frac{\partial x}{\partial r_i} \frac{\partial x}{\partial r_j} + \bar{e}_{yy} \frac{\partial y}{\partial r_i} \frac{\partial y}{\partial r_j} + \bar{e}_{xy} \frac{\partial x}{\partial r_i} \frac{\partial y}{\partial r_j} + \bar{e}_{yx} \frac{\partial y}{\partial r_i} \frac{\partial x}{\partial r_j}. \quad (1.32)$$

Then, substituting Eq. (1.31) to Eq. (1.32), we obtain the following conditions:

$$\begin{aligned} e_{rr}(u = x, v = 0) &= \frac{\partial x}{\partial r} \frac{\partial x}{\partial r}, & e_{rr}(u = 0, v = y) &= \frac{\partial y}{\partial r} \frac{\partial y}{\partial r}, & e_{rr}(u = y, v = x) &= 2 \frac{\partial x}{\partial r} \frac{\partial y}{\partial r}, \\ e_{ss}(u = x, v = 0) &= \frac{\partial x}{\partial s} \frac{\partial x}{\partial s}, & e_{ss}(u = 0, v = y) &= \frac{\partial y}{\partial s} \frac{\partial y}{\partial s}, & e_{ss}(u = y, v = x) &= 2 \frac{\partial x}{\partial s} \frac{\partial y}{\partial s}, \\ e_{rs}(u = x, v = 0) &= \frac{\partial x}{\partial r} \frac{\partial x}{\partial s}, & e_{rs}(u = 0, v = y) &= \frac{\partial y}{\partial r} \frac{\partial y}{\partial s}, & e_{rs}(u = y, v = x) &= \frac{\partial x}{\partial r} \frac{\partial y}{\partial s} + \frac{\partial y}{\partial r} \frac{\partial x}{\partial s}, \end{aligned} \quad (1.33)$$

The relations in Eq. (1.33) constrain the covariant components of strains to satisfy the membrane patch tests. It is evident that displacement-based element in Eq. (1.26) satisfies Eq. (1.33). Also, as long as ‘constant parts’ of the covariant strains which does not vary over element domain (r, s) is preserved, the patch test is passed and vice versa.

Element strains can often be grouped into the constant (e_{ij}^{const}) and linear (e_{ij}^{lin}) parts, in which the ‘linear parts’ of the element strains which vary linearly along r and s :

$$e_{ij}(r, s) = e_{ij}^{const} + e_{ij}^{lin}(r, s). \quad (1.34)$$

Hence, it is more precise that patch test is passed if the following conditions are met:

$$\begin{aligned} e_{ij}^{const}(u = x, v = 0) &= \frac{\partial x}{\partial r_i} \frac{\partial x}{\partial r_j}, & e_{ij}^{lin}(u = x, v = 0) &= 0, \\ e_{ij}^{const}(u = 0, v = y) &= \frac{\partial y}{\partial r_i} \frac{\partial y}{\partial r_j}, & e_{ij}^{lin}(u = 0, v = y) &= 0, \\ e_{ij}^{const}(u = y, v = x) &= \frac{\partial x}{\partial r_i} \frac{\partial y}{\partial r_j} + \frac{\partial y}{\partial r_i} \frac{\partial x}{\partial r_j}, & e_{ij}^{lin}(u = y, v = x) &= 0. \end{aligned} \quad (1.35)$$

Here we show usefulness of Eq. (1.35) using an example. In the developments of quadrilateral elements using enhanced assumed strain methods, the linear parts (e_{ij}^{lin}) of the covariant strains are often assumed in the following form

$$e_{ij}^{lin}(r,s) = c_{ij} r \frac{1}{j(r,s)} + d_{ij} s \frac{1}{j(r,s)} \quad \text{with} \quad j(r,s) = \frac{\partial x}{\partial r} \frac{\partial y}{\partial s} - \frac{\partial y}{\partial r} \frac{\partial x}{\partial s}, \quad (1.36)$$

that devoid of the bilinear term, where c_{ij} and d_{ij} are constant over r and s . The most widely used method for 4-node quadrilateral elements are 2×2 Gauss integration over element domain. Note that Eq. (1.35) actually constrains the numerically integrated strains, see [15].

Applying the 2×2 Gauss integration to linear strains of Eq. (1.36) we obtain

$$\begin{aligned} \int_V e_{ij}^{lin}(r,s) dV &= e_{ij}^{lin}(-a,-a)j(-a,-a) + e_{ij}^{lin}(-a,a)j(-a,a) + \\ &\quad e_{ij}^{lin}(a,-a)j(a,-a) + e_{ij}^{lin}(a,a)j(a,a) \\ &= c_{ij} \cdot 0 + d_{ij} \cdot 0 = 0 \quad \text{with} \quad a = 1/\sqrt{3}, \end{aligned} \quad (1.37)$$

so the strain in Eq. (1.36) obeys Eq. (1.35), satisfying the patch test.

In more general situations with different linear strains, the check of Eq. (1.35) can be difficult. In those cases, comparing the membrane strains with another strain fields satisfying the patch tests (such as that of displacement-based element) can be helpful.

1.4.2 Pass of zero energy mode tests

Here we discuss the conditions to pass the zero energy mode tests.

The zero energy mode tests can be decomposed into two categories: Check of the deformation modes having non-zero (and correct values of) eigenvalues and check of the rigid body modes having the zero eigenvalues.

For the deformation mode tests, deformation modes with correct non-zero eigenvalues are required. Checking whether each modes have correct eigenvalues can be performed using simple convergence tests of displacements. For example, the element should converge toward analytic solution of simple in-plane tests to insures all five in-plane modes shown in Fig. 1.2 (two in-plane stretching, two in-plane bending and one in-plane shearing) are correct. Since the eigenvalues of constant modes, such as in-plane stretching modes, are already tested through pass of patch tests, higher-order modes of in-plane bending and shearing need special considerations. For shell elements, on

the other hand, twisting mode about the direction normal to the thickness are not necessary [7,8], providing an exception to the deformation mode tests.

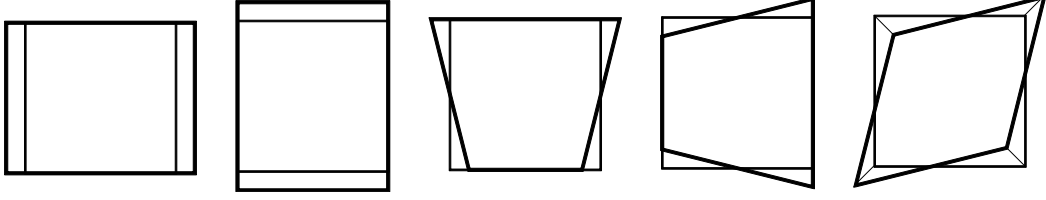


Fig. 1.2. Five in-plane modes of 4-node quadrilateral element.

For the rigid body mode tests, six physical zero energy mode must be present even when element is arbitrarily distorted. For the low-order shell elements in Fig. 1.3, following geometry and displacement interpolations are necessary:

For degenerated shell elements :

$$\mathbf{x}(r, s, t) = \sum_{i=1}^N h_i(r, s) \mathbf{x}_i + \frac{t}{2} \sum_{i=1}^N a_i h_i(r, s) \mathbf{V}_n^i, \quad (1.38a)$$

$$\mathbf{u}(r, s, t) = \sum_{i=1}^N h_i(r, s) \mathbf{u}_i + \frac{t}{2} \sum_{i=1}^N a_i h_i(r, s) (-\mathbf{V}_2^i \alpha_i + \mathbf{V}_1^i \beta_i), \quad (1.38b)$$

and for solid-shell elements :

$$\mathbf{x}(r, s, t) = \frac{1}{2} (1-t) \sum_{i=1}^N h_i(r, s) \mathbf{x}_i^{bot} + \frac{1}{2} (1+t) \sum_{i=1}^N h_i(r, s) \mathbf{x}_i^{top}, \quad (1.38c)$$

$$\mathbf{u}(r, s, t) = \frac{1}{2} (1-t) \sum_{i=1}^N h_i(r, s) \mathbf{u}_i^{bot} + \frac{1}{2} (1+t) \sum_{i=1}^N h_i(r, s) \mathbf{u}_i^{top}, \quad (1.38d)$$

with $N = 4$ and $N = 3$ for quadrilateral and triangular elements, respectively, $h_i(r, s)$ is the two-dimensional interpolation function of the standard isoparametric procedure corresponding to node i . For degenerated shell elements, \mathbf{x}_i is the position vector of node i in the global Cartesian coordinate system, and a_i and \mathbf{V}_n^i denote the shell thickness and the director vector at the node, respectively. For solid-shell elements, \mathbf{x}_i^{top} and \mathbf{x}_i^{bot} are the position vector of node i located at the top and bottom surface of the shell element, respectively. Also, α_i and β_i for degenerated shell elements denote rotations about vector \mathbf{V}_1^i and \mathbf{V}_2^i , each of which normal to the vector \mathbf{V}_n^i and to each other.

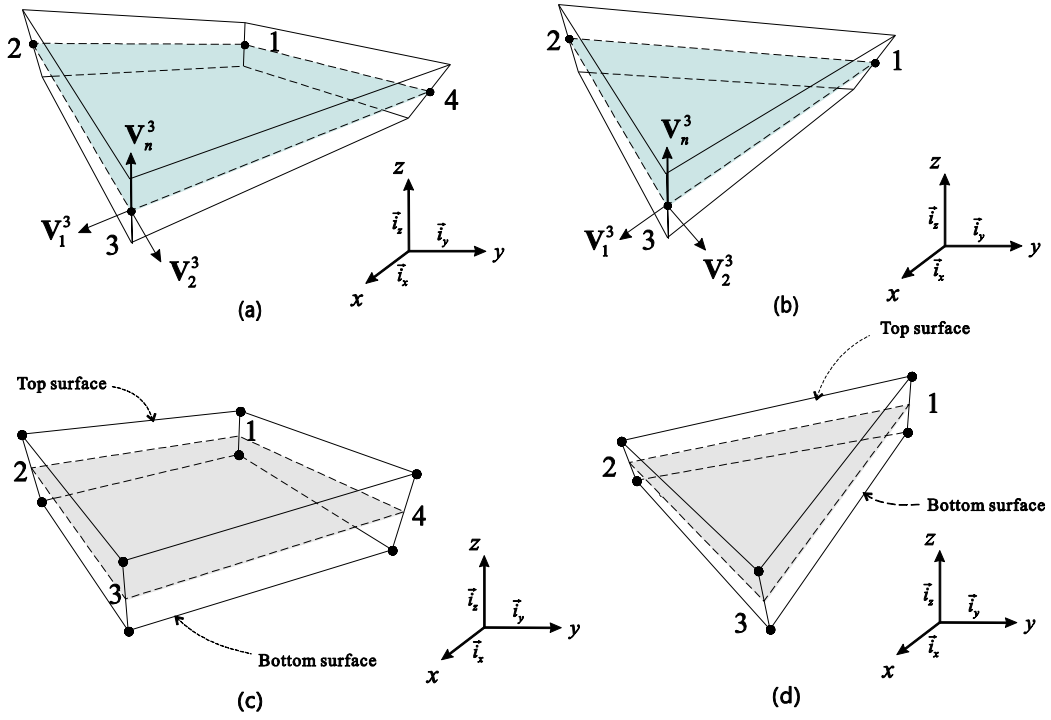


Fig. 1.3. Low-order continuum-mechanics based shell elements. (a) 4-node quadrilateral degenerated shell element. (b) 3-node triangular degenerated shell element. (c) 8-node quadrilateral solid-shell element. (d) 6-node triangular solid-shell element.

Attaining physical rigid body modes for solid-shell elements are straightforward, since the interpolation of displacement in Eq. (1.38d) includes only the nodal translations (\mathbf{u}_i^{top} and \mathbf{u}_i^{bot}). For degenerated shell elements, following rigid body modes must be present:

The three translational rigid body modes :

$$\mathbf{u}_i = \mathbf{c} \quad \text{with constant vector } \mathbf{c} \in \mathbf{R}^3, \quad (1.39a)$$

and the three rotational rigid body modes :

$$\mathbf{u}_i = \boldsymbol{\theta} \times \mathbf{x}_i \quad \text{and} \quad \boldsymbol{\theta} = \alpha_i \mathbf{V}_1^i + \beta_i \mathbf{V}_2^i \quad \text{with constant vector } \boldsymbol{\theta} \in \mathbf{R}^3. \quad (1.39b)$$

In Eq. (1.39b), the values of rotations with given pseudo-rotation vector ($\boldsymbol{\theta}$) are $\alpha_i = \boldsymbol{\theta} \cdot \mathbf{V}_1^i$ and $\beta_i = \boldsymbol{\theta} \cdot \mathbf{V}_2^i$, respectively.

The rotational rigid body modes can be not present along with the modifications introduced to treat locking. Particular case happens while treating membrane locking, when reduced integration applied

to covariant in-plane strains Eq. (1.26). In order to remedy this problem, following displacement projection method has been employed:

$$\begin{aligned}\mathbf{u}_i^{ori} &= [u_i \quad v_i \quad w_i \quad \alpha_i \quad \beta_i]^T, \\ \mathbf{u}_i^{new} &= \mathbf{P}_i \mathbf{u}_i^{ori}, \\ \mathbf{P}_i &= \mathbf{I} - \mathbf{R}_i (\mathbf{R}_i^T \mathbf{R}_i)^{-1} \mathbf{R}_i^T,\end{aligned}\tag{1.40a}$$

with

$$\mathbf{R}_i = \begin{pmatrix} 0 & z_i - z_c & -(y_i - y_c) \\ -(z_i - z_c) & 0 & x_i - x_c \\ y_i - y_c & -(x_i - x_c) & 0 \\ -V_{2i}^x & -V_{2i}^y & -V_{2i}^z \\ V_{1i}^x & V_{1i}^y & V_{1i}^z \end{pmatrix}$$

$$\begin{aligned}\mathbf{x}_i &= x_i \mathbf{i}_x + y_i \mathbf{i}_y + z_i \mathbf{i}_z, \quad \mathbf{u}_i = u_i \mathbf{i}_x + v_i \mathbf{i}_y + w_i \mathbf{i}_z, \\ \mathbf{V}_1^i &= V_{1i}^x \mathbf{i}_x + V_{1i}^y \mathbf{i}_y + V_{1i}^z \mathbf{i}_z, \quad \mathbf{V}_2^i = V_{2i}^x \mathbf{i}_x + V_{2i}^y \mathbf{i}_y + V_{2i}^z \mathbf{i}_z, \\ \mathbf{x}_c &= \frac{1}{N} \sum_{i=1}^N \mathbf{x}_i \quad \text{and} \quad \mathbf{x}_c = x_c \mathbf{i}_x + y_c \mathbf{i}_y + z_c \mathbf{i}_z.\end{aligned}\tag{1.40b}$$

In Eq. (1.40a), the original displacements (translations and rotations) \mathbf{u}_i^{ori} are projected using the matrix $\mathbf{P}_i = \mathbf{I} - \mathbf{R}_i (\mathbf{R}_i^T \mathbf{R}_i)^{-1} \mathbf{R}_i^T$ to form the new nodal displacement vector \mathbf{u}_i^{new} that replaces \mathbf{u}_i^{ori} at each node i . This procedure is not only costly, but mixes the translation and rotations for curved quadrilateral shell elements, thereby deteriorating the quality of strains and stresses. Ideally, projection schemes applied on geometry or displacement should be avoided during locking treatments of quadrilateral shell elements, and physical rigid body modes as well as physical nature of displacement unknowns should be preserved thoroughly.

1.5 Outline of the paper

Here, organization of the paper is presented.

In Chapter 1, brief overview of the present research was introduced. The previous studies of the low-order shell elements were investigated to set two different goals of the present study: remedy-membrane locking of 4-node quadrilateral shell element and alleviating thickness locking of 6-

node triangular solid-shell element. Previous studies regarding each goal were presented. Original theoretical study investigating the cause of membrane locking of 4-node quadrilateral shell element was presented.

In Chapter 2, the new 4-node degenerated shell elements are presented in the subsequent order of developments (MITC4+, MITC4+N and new MITC4+). The formulations of the three elements are firstly presented and the performance of the elements is shown through basic tests, benchmark tests and convergence studies on linear analysis. For the latest (new MITC4+) shell element, performance in geometric nonlinear analysis is also presented.

In Chapter 3, the new 6-node triangular solid-shell element (MITC-S6) is presented. The formulation is presented and the performance of the element is examined through basic tests, convergence studies and geometric nonlinear problems.

In Chapter 4, conclusion of the present study is stated.

Chapter 2. The improved 4-node quadrilateral shell elements

2.1 The formulations of the developed 4-node quadrilateral shell elements

In this section, the formulations of newly developed 4-node quadrilateral shell elements, the MITC4+ [5], MITC4+N and new MITC4+ [103] shell elements, are presented. The geometry and displacement interpolations of the new shell elements are as for the MITC4 shell element.

2.1.1 Basic 4-node quadrilateral shell element, MITC4

In this section, we present basic 4-node quadrilateral shell element used for further development in this study. It has to satisfy all the basic tests while transverse shear strain is optimally treated against shear locking. For that purpose, the MITC4 shell element is chosen, and its formulation is briefly reviewed here.

The geometry of a standard 4-node continuum mechanics based quadrilateral shell element is interpolated using [1,5,15]

$$\mathbf{x}(r, s, t) = \sum_{i=1}^4 h_i(r, s) \mathbf{x}_i + \frac{t}{2} \sum_{i=1}^4 a_i h_i(r, s) \mathbf{V}_n^i, \quad (2.1)$$

where $h_i(r, s)$ is the two-dimensional interpolation function of the standard isoparametric procedure corresponding to node i , \mathbf{x}_i is the position vector of node i in the global Cartesian coordinate system, and a_i and \mathbf{V}_n^i denote the shell thickness and the director vector at the node, respectively, see Fig. 2.1.

It is useful to note the following representation of interpolation function $h_i(r, s)$:

$$h_i(r, s) = \frac{1}{4} (1 + \xi_i r)(1 + \eta_i s) \quad \text{with } i = 1, 2, 3, 4,$$

$$\begin{bmatrix} \xi_1 & \xi_2 & \xi_3 & \xi_4 \end{bmatrix} = [1 \quad -1 \quad -1 \quad 1],$$

$$\begin{bmatrix} \eta_1 & \eta_2 & \eta_3 & \eta_4 \end{bmatrix} = [1 \quad 1 \quad -1 \quad -1], \quad (2.2)$$

in which the signs ζ_i and η_i are allowed to be permuted together.

The corresponding displacement interpolation of the element is

$$\mathbf{u}(r, s, t) = \sum_{i=1}^4 h_i(r, s) \mathbf{u}_i + \frac{t}{2} \sum_{i=1}^4 a_i h_i(r, s) (-\mathbf{V}_2^i \alpha_i + \mathbf{V}_1^i \beta_i), \quad (2.3)$$

in which \mathbf{u}_i is the nodal displacement vector in the global Cartesian coordinate system, \mathbf{V}_1^i and \mathbf{V}_2^i are unit vectors orthogonal to \mathbf{V}_n^i and to each other, and α_i and β_i are the rotations of the director vector \mathbf{V}_n^i about \mathbf{V}_1^i and \mathbf{V}_2^i , respectively, at node i .

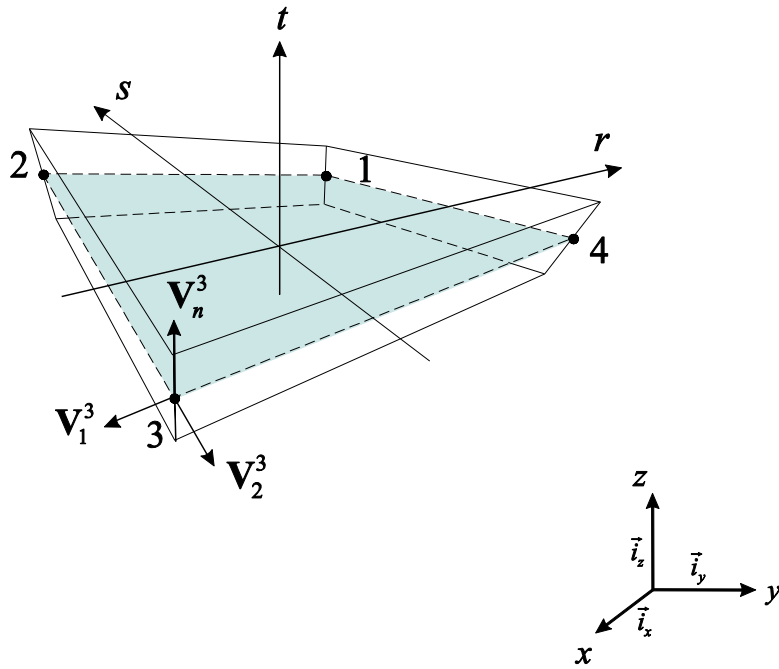


Fig. 2.1. A standard 4-node quadrilateral continuum mechanics based shell element.

The linear terms of the displacement-based covariant strain components are given by

$$e_{ij} = \frac{1}{2} (\mathbf{g}_i \cdot \mathbf{u}_{,j} + \mathbf{g}_j \cdot \mathbf{u}_{,i}), \quad (2.4)$$

in which

$$\mathbf{g}_i = \frac{\partial \mathbf{x}}{\partial r_i}, \quad \mathbf{u}_{,i} = \frac{\partial \mathbf{u}}{\partial r_i} \quad \text{with } r_1 = r, \quad r_2 = s, \quad r_3 = t. \quad (2.5)$$

For the MITC4 shell element, the covariant in-plane strain components are calculated using Eqs. (2.1) to (2.3) without any modification. The transverse shear strain field is based on assuming con-

stant covariant transverse shear strain conditions along the edges, see Ref. [6]

$$\tilde{e}_{rt} = \frac{1}{2}(1+s)e_{rt}^{(A)} + \frac{1}{2}(1-s)e_{rt}^{(B)}, \quad \tilde{e}_{st} = \frac{1}{2}(1+r)e_{st}^{(C)} + \frac{1}{2}(1-r)e_{st}^{(D)}, \quad (2.6)$$

where the tying points are shown in Fig. 2.2 [1,13].

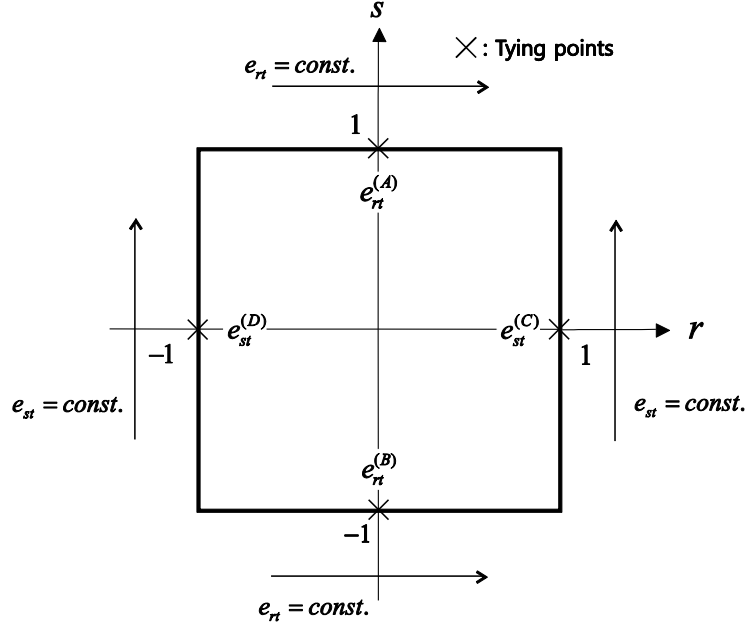


Fig. 2.2. Tying positions (A), (B), (C) and (D) for the assumed transverse shear strain field of the MITC4 shell element. The constant transverse shear strain conditions are imposed along its edges.

The covariant in-plane strain in Eq. (2.4) can be written as

$$e_{ij} = e_{ij}^m + t e_{ij}^{b1} + t^2 e_{ij}^{b2} \quad \text{with} \quad i, j = 1, 2, \quad (2.7a)$$

$$e_{ij}^m = \frac{1}{2} \left(\frac{\partial \mathbf{x}_m}{\partial r_i} \cdot \frac{\partial \mathbf{u}_m}{\partial r_j} + \frac{\partial \mathbf{x}_m}{\partial r_j} \cdot \frac{\partial \mathbf{u}_m}{\partial r_i} \right), \quad (2.7b)$$

$$e_{ij}^{b1} = \frac{1}{2} \left(\frac{\partial \mathbf{x}_m}{\partial r_i} \cdot \frac{\partial \mathbf{u}_b}{\partial r_j} + \frac{\partial \mathbf{x}_m}{\partial r_j} \cdot \frac{\partial \mathbf{u}_b}{\partial r_i} + \frac{\partial \mathbf{x}_b}{\partial r_i} \cdot \frac{\partial \mathbf{u}_m}{\partial r_j} + \frac{\partial \mathbf{x}_b}{\partial r_j} \cdot \frac{\partial \mathbf{u}_m}{\partial r_i} \right), \quad (2.7c)$$

$$e_{ij}^{b2} = \frac{1}{2} \left(\frac{\partial \mathbf{x}_b}{\partial r_i} \cdot \frac{\partial \mathbf{u}_b}{\partial r_j} + \frac{\partial \mathbf{x}_b}{\partial r_j} \cdot \frac{\partial \mathbf{u}_b}{\partial r_i} \right), \quad (2.7d)$$

with

$$\mathbf{x}_m = \sum_{i=1}^4 h_i(r, s) \mathbf{x}_i, \quad \mathbf{x}_b = \frac{1}{2} \sum_{i=1}^4 a_i h_i(r, s) \mathbf{V}_n^i, \quad (2.8a)$$

$$\mathbf{u}_m = \sum_{i=1}^4 h_i(r, s) \mathbf{u}_i, \quad \mathbf{u}_b = \frac{1}{2} \sum_{i=1}^4 a_i h_i(r, s) (-\mathbf{V}_2^i \alpha_i + \mathbf{V}_1^i \beta_i), \quad (2.8b)$$

The first term e_{ij}^m in Eq. (2.7a) is the covariant in-plane membrane strain at the shell mid-surface ($t = 0$), and the remaining terms are the covariant in-plane strains due to bending. The in-plane membrane strain, see Eq. (2.7b), can in general induce locking.

2.1.2 The MITC4+ shell element

In the formulation of the MITC4+ shell element [5] the mid-surface of the element is subdivided into four non-overlapping 3-node triangular domains, and the assumed membrane strain field is constructed using the membrane strains of the flat triangular domains.

Let us define the center point denoted by '5' in the mid-surface of the 4-node shell element as shown in Fig. 2.3

$$\mathbf{x}_5 = \sum_{i=1}^4 \gamma_i \mathbf{x}_i, \quad (2.9)$$

where the constants γ_i are used to determine the position of the center point. The choice of constants is important for the element isotropy and the membrane patch tests.

As shown in Fig. 2.4, the geometric centroid of triangle 1 defined by nodes 1-2-4 is

$$\mathbf{x}_{T1} = \frac{1}{3}\mathbf{x}_1 + \frac{1}{3}\mathbf{x}_2 + \frac{1}{3}\mathbf{x}_4 = \begin{bmatrix} \frac{1}{3} & \frac{1}{3} & 0 & \frac{1}{3} \end{bmatrix} [\mathbf{x}_1 \quad \mathbf{x}_2 \quad \mathbf{x}_3 \quad \mathbf{x}_4]^T, \quad (2.10)$$

and, similarly, the geometric centroid of triangle 2 is given by

$$\mathbf{x}_{T2} = \begin{bmatrix} 0 & \frac{1}{3} & \frac{1}{3} & \frac{1}{3} \end{bmatrix} [\mathbf{x}_1 \quad \mathbf{x}_2 \quad \mathbf{x}_3 \quad \mathbf{x}_4]^T. \quad (2.11)$$

Then, the geometric centroid of triangles 1 and 2 is calculated using the following equation

$$\mathbf{x}_{T12} = \frac{A_1}{A_1 + A_2} \mathbf{x}_{T1} + \frac{A_2}{A_1 + A_2} \mathbf{x}_{T2}, \quad (2.12)$$

where A_1 and A_2 are the areas of triangles 1 and 2 shown in Fig. 2.4.

Similarly, the geometric centroid of triangles 3 and 4 is

$$\mathbf{x}_{T34} = \frac{A_3}{A_3 + A_4} \mathbf{x}_{T3} + \frac{A_4}{A_3 + A_4} \mathbf{x}_{T4} \quad (2.13)$$

with

$$\mathbf{x}_{T3} = \left[\frac{1}{3} \quad \frac{1}{3} \quad \frac{1}{3} \quad 0 \right] [\mathbf{x}_1 \quad \mathbf{x}_2 \quad \mathbf{x}_3 \quad \mathbf{x}_4]^T, \quad \mathbf{x}_{T4} = \left[\frac{1}{3} \quad 0 \quad \frac{1}{3} \quad \frac{1}{3} \right] [\mathbf{x}_1 \quad \mathbf{x}_2 \quad \mathbf{x}_3 \quad \mathbf{x}_4]^T, \quad (2.14)$$

in which A_3 and A_4 are the areas of triangles 3 and 4.

Finally, the mean position of two geometric centroids is simply obtained by

$$\mathbf{x}_5 = \frac{1}{2} (\mathbf{x}_{T12} + \mathbf{x}_{T34}) = [\gamma_1 \quad \gamma_2 \quad \gamma_3 \quad \gamma_4] [\mathbf{x}_1 \quad \mathbf{x}_2 \quad \mathbf{x}_3 \quad \mathbf{x}_4]^T = \sum_{i=1}^4 \gamma_i \mathbf{x}_i \quad (2.15a)$$

$$\begin{aligned} \text{with } [\gamma_1 \quad \gamma_2 \quad \gamma_3 \quad \gamma_4] &= \frac{1}{2} \frac{A_1}{A_1 + A_2} \left[\frac{1}{3} \quad \frac{1}{3} \quad 0 \quad \frac{1}{3} \right] + \frac{1}{2} \frac{A_2}{A_1 + A_2} \left[0 \quad \frac{1}{3} \quad \frac{1}{3} \quad \frac{1}{3} \right] \\ &+ \frac{1}{2} \frac{A_3}{A_3 + A_4} \left[\frac{1}{3} \quad \frac{1}{3} \quad \frac{1}{3} \quad 0 \right] + \frac{1}{2} \frac{A_4}{A_3 + A_4} \left[\frac{1}{3} \quad 0 \quad \frac{1}{3} \quad \frac{1}{3} \right]. \end{aligned} \quad (2.15b)$$

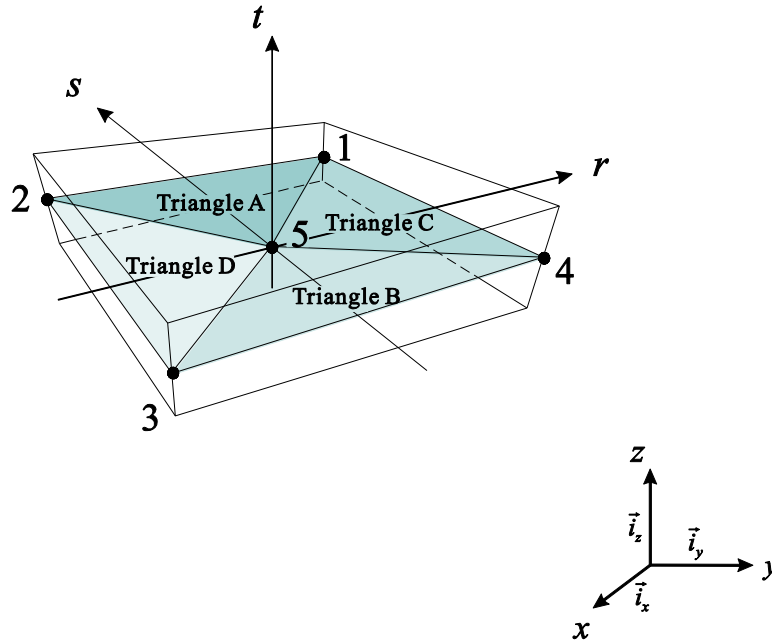


Fig. 2.3. Triangular subdivision of the mid-surface of the 4-node shell element.

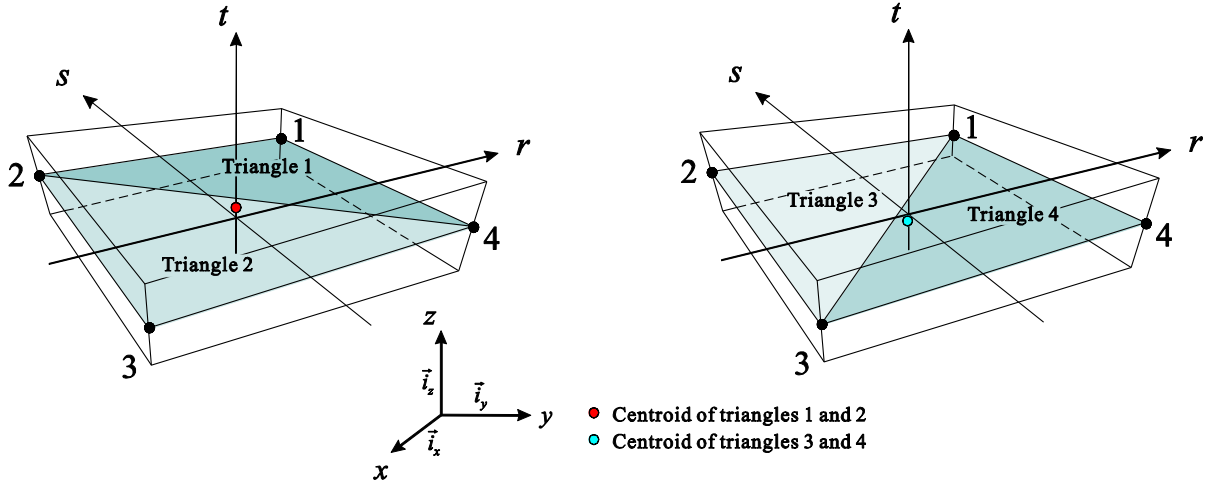


Fig. 2.4. Four triangles to determine the center point of the MITC4+ shell element.

Using the defined center point, the mid-surface of the 4-node shell element is divided into four flat triangular domains, see Fig. 2.3. Each triangular domain can be interpolated using the following geometry interpolation function

$$\bar{\mathbf{x}}(r, s, t) = \sum_{i=1}^3 \hat{h}_i(r, s) \bar{\mathbf{x}}_i \quad \text{with} \quad \hat{h}_1(r, s) = r, \quad \hat{h}_2(r, s) = s, \quad \hat{h}_3(r, s) = 1 - r - s, \quad (2.16)$$

and

$$\bar{\mathbf{x}}_1 = \mathbf{x}_1, \quad \bar{\mathbf{x}}_2 = \mathbf{x}_2, \quad \bar{\mathbf{x}}_3 = \mathbf{x}_5 \quad \text{for triangle A,} \quad \bar{\mathbf{x}}_1 = \mathbf{x}_3, \quad \bar{\mathbf{x}}_2 = \mathbf{x}_4, \quad \bar{\mathbf{x}}_3 = \mathbf{x}_5 \quad \text{for triangle B,}$$

$$\bar{\mathbf{x}}_1 = \mathbf{x}_4, \quad \bar{\mathbf{x}}_2 = \mathbf{x}_1, \quad \bar{\mathbf{x}}_3 = \mathbf{x}_5 \quad \text{for triangle C,} \quad \bar{\mathbf{x}}_1 = \mathbf{x}_2, \quad \bar{\mathbf{x}}_2 = \mathbf{x}_3, \quad \bar{\mathbf{x}}_3 = \mathbf{x}_5 \quad \text{for triangle D,}$$

in which $\hat{h}_i(r, s)$ is the two-dimensional interpolation function of the 3-node triangular element corresponding to node i , and $\bar{\mathbf{x}}_i$ is the position vector at node i . Note that the subdivision into two non-overlapping triangular domains is also possible, but then the element isotropy cannot be satisfied.

The interpolation of the corresponding translational displacement vector is given by

$$\hat{\mathbf{u}}(r, s, t) = \sum_{i=1}^3 \hat{h}_i(r, s) \hat{\mathbf{u}}_i, \quad (2.17)$$

where $\hat{\mathbf{u}}_i$ is the translational displacement vector at node i .

In the MITC4+ shell element, the displacement vector at the center point is represented by the displacement vectors at the corner nodes

$$\mathbf{u}_5 = \sum_{i=1}^4 \gamma_i \mathbf{u}_i. \quad (2.18)$$

Note that the isoparametric relation between Eq. (2.9) and Eq. (2.18) is important to correctly represent rigid body modes in the 4-node shell element. Note that the displacements at the center point are not degrees of freedom in the element formulation.

The covariant membrane strain in the triangular domains is given by

$$\bar{e}_{ij}^m = \frac{1}{2} \left(\frac{\partial \bar{\mathbf{x}}}{\partial r_i} \cdot \frac{\partial \bar{\mathbf{u}}}{\partial r_j} + \frac{\partial \bar{\mathbf{x}}}{\partial r_j} \cdot \frac{\partial \bar{\mathbf{u}}}{\partial r_i} \right) \quad \text{with } i, j = 1, 2. \quad (2.19)$$

The covariant membrane strain in Eq. (2.19) has two covariant base vectors,

$$\hat{\mathbf{g}}_i = \frac{\partial \bar{\mathbf{x}}}{\partial r_i} \quad \text{with } i = 1, 2, \quad (2.20a)$$

which are supplemented with the third covariant base vector of

$$\hat{\mathbf{g}}_3 = \mathbf{g}_3. \quad (2.20b)$$

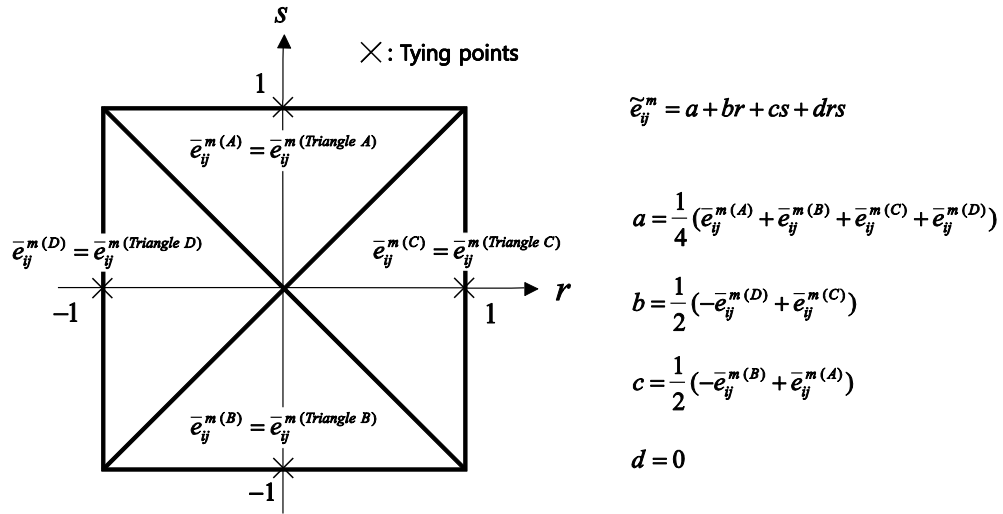


Fig. 2.5. Tying positions (A), (B), (C) and (D) for the assumed membrane strain field of the MITC4+ shell element.

In order to apply the assumed strain method, the covariant membrane strain from each triangular domain must be transported to the natural coordinate system of the 4-node shell element. The strain transformation is given by ($i, j = 1, 2$ and $k, l = 1, 2$),

$$\bar{e}_{ij}^m = \bar{e}_{kl}^m (\mathbf{g}_i \cdot \hat{\mathbf{g}}^k) (\mathbf{g}_j \cdot \hat{\mathbf{g}}^l), \quad (2.21)$$

in which $\widehat{\mathbf{g}}^i \cdot \widehat{\mathbf{g}}_j = \delta_{ij}$ with δ_{ij} the Kronecker delta.

Using the covariant membrane strains evaluated from the four triangular domains, constructing a new assumed strain field which alleviates the locking is necessary. It starts with the following assumption

$$\tilde{e}_{ij}^m = a + br + cs + drs \quad \text{with } i, j = 1, 2, \quad (2.22)$$

in which the coefficients a , b , c and d are determined using the covariant membrane strains evaluated in the triangular domains.

While the strains are constant within each triangular domain, the tying positions symmetric about the element center are chosen, see Fig. 2.5. Then the following tying conditions are employed

$$\tilde{e}_{ij}^m(0, 1) = \bar{e}_{ij}^{m(A)}, \quad \tilde{e}_{ij}^m(0, -1) = \bar{e}_{ij}^{m(B)}, \quad \tilde{e}_{ij}^m(1, 0) = \bar{e}_{ij}^{m(C)}, \quad \tilde{e}_{ij}^m(-1, 0) = \bar{e}_{ij}^{m(D)}, \quad (2.23)$$

The four coefficients in Eq. (2.22) are thus obtained as

$$a = \frac{1}{4}(\bar{e}_{ij}^{m(A)} + \bar{e}_{ij}^{m(B)} + \bar{e}_{ij}^{m(C)} + \bar{e}_{ij}^{m(D)}), \quad b = \frac{1}{2}(-\bar{e}_{ij}^{m(D)} + \bar{e}_{ij}^{m(C)}), \quad c = \frac{1}{2}(-\bar{e}_{ij}^{m(B)} + \bar{e}_{ij}^{m(A)}),$$

$$d = 0. \quad (2.24)$$

Finally, the new assumed strain field for the membrane strains is given as

$$\tilde{e}_{ij}^m = \frac{1}{4}(\bar{e}_{ij}^{m(A)} + \bar{e}_{ij}^{m(B)} + \bar{e}_{ij}^{m(C)} + \bar{e}_{ij}^{m(D)}) + \frac{1}{2}(-\bar{e}_{ij}^{m(D)} + \bar{e}_{ij}^{m(C)})r + \frac{1}{2}(-\bar{e}_{ij}^{m(B)} + \bar{e}_{ij}^{m(A)})s, \quad (2.25)$$

Note that the assumed membrane strains in Eq. (2.25) do not have the bi-linear term (rs) which causes membrane locking of the MITC4 element when geometrically distorted, see Section 2.3.

The MITC4+ shell element alleviates membrane locking while satisfying the basic tests, but has slight disadvantages on reduced membrane behaviors and approximate pass of membrane patch tests. In order to retain membrane behaviors, the MITC4+N shell element is developed.

2.1.3 The MITC4+N shell element

In order to improve the membrane behavior of the MITC4+ shell element, the basic interpolation

used for the assumed membrane strain is modified.

Firstly, the center point for the subdivision of the mid-surface shown in Fig. 2.3 is redefined. Let us consider two lines in Fig. 2.6(a): line 24 (connecting the nodes 2 and 4), and line 13 (connecting the nodes 1 and 3). A line segment which is orthogonal to both lines 24 and 13 can be defined. The line segment represents the shortest distance between the lines 24 and 13. The new center point is located on the midpoint of the line segment, as shown in Fig. 2.6(a) and (b). When the element geometry is flat, the center point becomes the point of intersection of the two diagonals, see Fig. 2.6(c). This choice is very important for the satisfaction of the isotropy and the membrane patch tests.

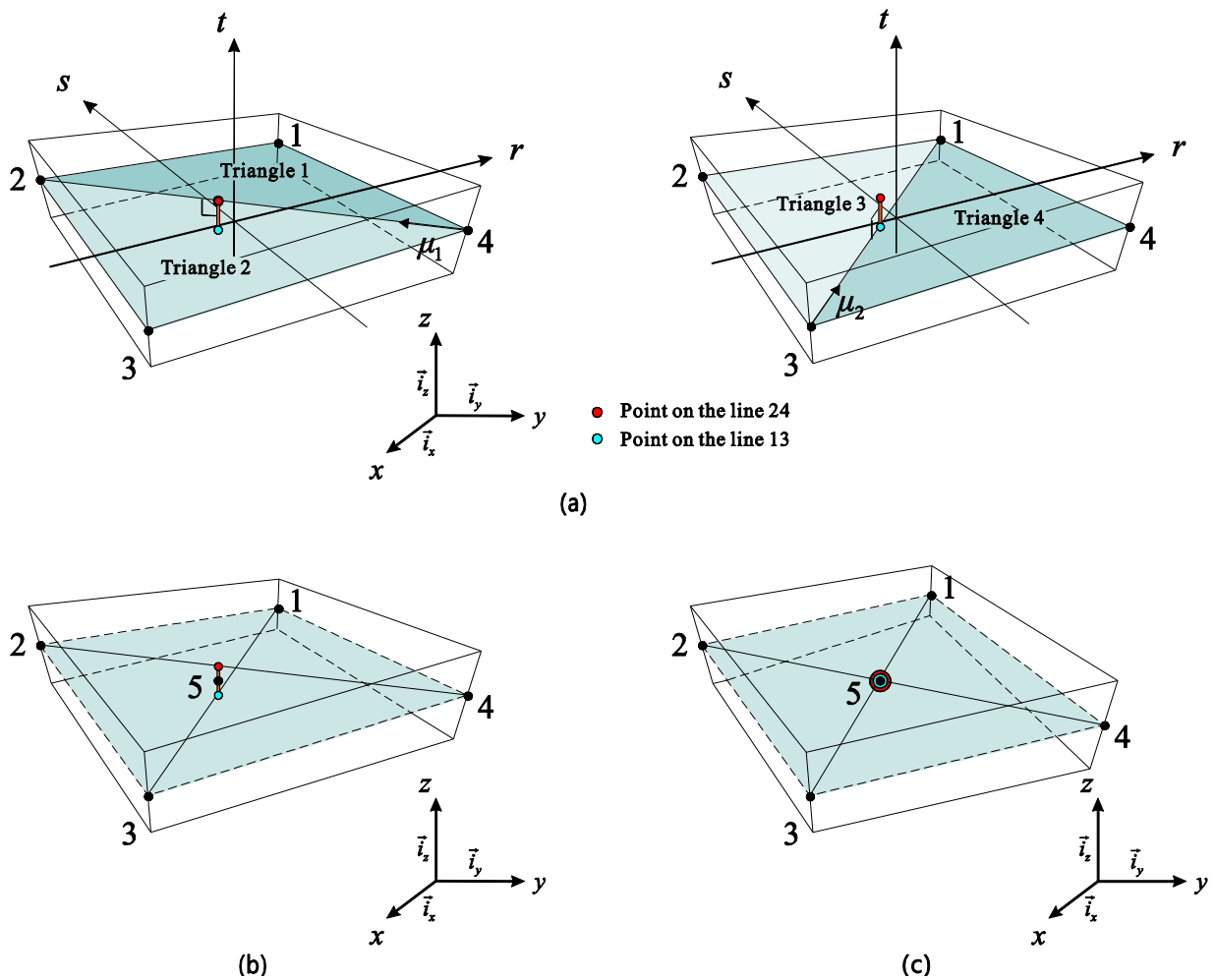


Fig. 2.6. The construction of center points. (a) Four triangles to determine the center points of the original and the MITC4+N shell elements. (b) The new center point ('5') for the MITC4+N shell element. (c) Location of the new center point for flat geometry.

A simple procedure for obtaining the location of the new center point is derived for arbitrary geome-

try of the MITC4+N shell element.

Let us denote the vectors representing the line 13 and 24 in Fig. 2.6(a) by $\mathbf{x}_{13} = \mathbf{x}_1 - \mathbf{x}_3$ and $\mathbf{x}_{24} = \mathbf{x}_2 - \mathbf{x}_4$, respectively. Two ends points of the line segment are defined,

$$\mathbf{p}_{24} = \mu_1 \mathbf{x}_2 + (1 - \mu_1) \mathbf{x}_4, \quad \mathbf{p}_{13} = \mu_2 \mathbf{x}_1 + (1 - \mu_2) \mathbf{x}_3, \quad (2.26)$$

on the line 24 and 13, respectively, with $\mu_1, \mu_2 \in [0,1]$.

Then, the center point is defined by

$$\mathbf{x}_5 = \frac{1}{2}(\mathbf{p}_{13} + \mathbf{p}_{24}), \quad (2.27)$$

where the values of μ_1 and μ_2 need to be solved from the orthogonality of the line segment to the line 13 and 24,

$$\mathbf{x}_{24} \cdot (\mathbf{p}_{13} - \mathbf{p}_{24}) = \mathbf{x}_{13} \cdot (\mathbf{p}_{13} - \mathbf{p}_{24}) = 0. \quad (2.28)$$

In the special case of $\mathbf{x}_{24} \cdot \mathbf{x}_{13} = 0$, the solution of Eq. (2.28) is given by

$$\mu_2 = -(\mathbf{x}_{34} \cdot \mathbf{x}_{13}) / (\mathbf{x}_{13} \cdot \mathbf{x}_{13}), \quad \mu_1 = (\mathbf{x}_{34} \cdot \mathbf{x}_{24}) / (\mathbf{x}_{24} \cdot \mathbf{x}_{24}), \quad (2.29)$$

where $\mathbf{x}_{34} = \mathbf{x}_3 - \mathbf{x}_4$.

In the case of $\mathbf{x}_{24} \cdot \mathbf{x}_{13} \neq 0$, the solution of Eq. (2.28) is given by

$$\mu_2 = -(\mathbf{w}_2 \cdot \mathbf{w}_1) / (\mathbf{w}_1 \cdot \mathbf{w}_1), \quad \mu_1 = c_1 \mu_2 + c_2, \quad (2.30)$$

in which

$$\begin{aligned} \mathbf{w}_1 &= \mathbf{x}_{13} - c_1 \mathbf{x}_{24}, \quad \mathbf{w}_2 = \mathbf{x}_{34} - c_2 \mathbf{x}_{24}, \\ c_1 &= (\mathbf{x}_{13} \cdot \mathbf{x}_{13}) / (\mathbf{x}_{24} \cdot \mathbf{x}_{13}), \quad c_2 = (\mathbf{x}_{34} \cdot \mathbf{x}_{13}) / (\mathbf{x}_{24} \cdot \mathbf{x}_{13}). \end{aligned} \quad (2.31)$$

Next, the new interpolation function which is used for the assumed membrane strain is defined. Note that in Eqs. (2.16) and (2.17), the interpolation function as well as the resulting membrane interpolation resides within each triangular domains. In the MITC4+N shell element, the tying membrane strains are constructed from the whole quadrilateral domain in aim of improving the membrane performances. This concept is naturally related to the quadrilateral area coordinate methods, see Refs. [104-107], which use areas of subdivided triangular domains [5,104,107] to represent the interpolation functions for the quadrilateral domain.

Using the defined center point, four characteristic constants related to the area ratio of the triangles in Fig. 2.3 are obtained,

$$\begin{aligned} G_1 &= (A_A + A_C) / A, & G_2 &= (A_A + A_D) / A, \\ G_3 &= (A_D + A_B) / A, & G_4 &= (A_B + A_C) / A, \end{aligned} \quad (2.32)$$

with $A = A_A + A_B + A_C + A_D$, where A_A , A_B , A_C and A_D denote the areas of triangles A, B, C, and D shown in Fig. 2.3.

The new interpolation functions are defined as in Ref. [107],

$$\begin{aligned} \hat{h}_1 &= \frac{G_3}{2} - q_1 + G_3 p, & \hat{h}_2 &= \frac{G_4}{2} - q_2 - G_4 p, \\ \hat{h}_3 &= \frac{G_1}{2} + q_1 + G_1 p, & \hat{h}_4 &= \frac{G_2}{2} + q_2 - G_2 p, \end{aligned} \quad (2.33)$$

with

$$q_1 = \frac{1}{4} [r + s + (G_3 - G_1)(1 + rs)], \quad q_2 = \frac{1}{4} [-r + s + (G_4 - G_2)(1 - rs)], \quad (2.34)$$

$$p = \left[3(q_1^2 - q_2^2) + 2(G_1 - G_3)q_1 + (G_4 - G_2)q_2 + \frac{(G_2 G_4 - G_1 G_3)}{2} \right] / (1 + G_1 G_3 + G_2 G_4). \quad (2.35)$$

The ‘area coordinates’ q_1 and q_2 newly defined on the subdivided quadrilateral mid-surface are shown in Fig. 2.7.

The derivatives of the new interpolation functions in Eq. (2.33) can be calculated from the chain rule,

$$\frac{\partial \hat{h}_i}{\partial r} = \frac{\partial \hat{h}_i}{\partial q_k} \frac{\partial q_k}{\partial r}, \quad \frac{\partial \hat{h}_i}{\partial s} = \frac{\partial \hat{h}_i}{\partial q_k} \frac{\partial q_k}{\partial s}, \quad (2.36)$$

for $i = 1, \dots, 4$ and $k = 1, 2$. The explicit forms of the derivatives $\frac{\partial \hat{h}_i}{\partial q_k}$, $\frac{\partial q_k}{\partial r}$ and $\frac{\partial q_k}{\partial s}$ are given

as follows.

$$\begin{bmatrix} \frac{\partial q_1}{\partial r} \\ \frac{\partial q_2}{\partial r} \end{bmatrix} = \begin{bmatrix} \frac{1}{4}(1 + (G_3 - G_1)s) \\ \frac{1}{4}(-1 - (G_4 - G_2)s) \end{bmatrix}, \quad \begin{bmatrix} \frac{\partial q_1}{\partial s} \\ \frac{\partial q_2}{\partial s} \end{bmatrix} = \begin{bmatrix} \frac{1}{4}(1 + (G_3 - G_1)r) \\ \frac{1}{4}(1 - (G_4 - G_2)r) \end{bmatrix}, \quad (2.37)$$

$$\begin{bmatrix} \frac{\partial \hat{h}_1}{\partial q_1} & \frac{\partial \hat{h}_1}{\partial q_2} \\ \frac{\partial \hat{h}_2}{\partial q_1} & \frac{\partial \hat{h}_2}{\partial q_2} \\ \frac{\partial \hat{h}_3}{\partial q_1} & \frac{\partial \hat{h}_3}{\partial q_2} \\ \frac{\partial \hat{h}_4}{\partial q_1} & \frac{\partial \hat{h}_4}{\partial q_2} \end{bmatrix} = \begin{bmatrix} -1+G_3 \frac{\partial p}{\partial q_1} & G_3 \frac{\partial p}{\partial q_2} \\ -G_4 \frac{\partial p}{\partial q_1} & -1-G_4 \frac{\partial p}{\partial q_2} \\ 1+G_1 \frac{\partial p}{\partial q_1} & G_1 \frac{\partial p}{\partial q_2} \\ -G_2 \frac{\partial p}{\partial q_1} & 1-G_2 \frac{\partial p}{\partial q_2} \end{bmatrix}, \quad (2.38)$$

with

$$\begin{bmatrix} \frac{\partial p}{\partial q_1} & \frac{\partial p}{\partial q_2} \end{bmatrix}^T = \frac{1}{1+G_1G_3+G_2G_4} \begin{bmatrix} 6q_1+2(G_1-G_3) \\ -6q_2+2(G_4-G_2) \end{bmatrix}. \quad (2.39)$$

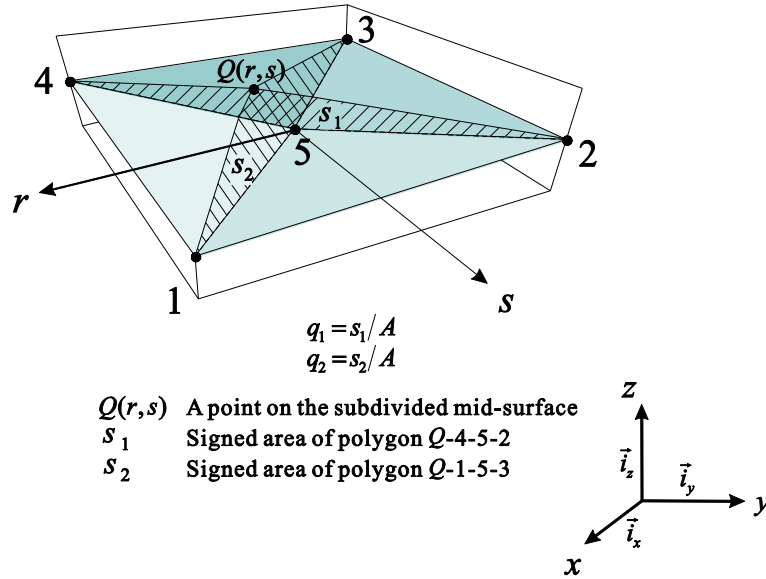


Fig. 2.7. Area coordinates (q_1 and q_2) used for the MITC4+N shell element. The polygons are formed by shortest paths between the nodes and an arbitrary point $Q(r,s)$ on the subdivided mid-surface.

Finally, the geometry and displacement interpolations used for the membrane strain of the MITC4+N shell element is given by

$$\bar{\mathbf{x}}(r,s,t) = \sum_{i=1}^4 \hat{h}_i(r,s) \mathbf{x}_i, \quad \bar{\mathbf{u}}(r,s,t) = \sum_{i=1}^4 \hat{h}_i(r,s) \mathbf{u}_i. \quad (2.40)$$

The corresponding covariant membrane strains are given by

$$\hat{e}_{ij}^m = \frac{1}{2}(\hat{\mathbf{g}}_i \cdot \hat{\mathbf{u}}_{,j} + \hat{\mathbf{g}}_j \cdot \hat{\mathbf{u}}_{,i}) \quad \text{with } i, j = 1, 2, \quad (2.41)$$

where

$$\hat{\mathbf{g}}_i = \frac{\partial \hat{\mathbf{x}}}{\partial r_i}, \quad \hat{\mathbf{u}}_{,i} = \frac{\partial \hat{\mathbf{u}}}{\partial r_i} \quad \text{and} \quad \hat{\mathbf{g}}_3 = \mathbf{g}_3. \quad (2.42)$$

The new membrane strains are transformed into fixed coordinate system located at the element center [86],

$$\bar{e}_{ij}^m = \hat{e}_{kl}^m (\mathbf{g}_i^c \cdot \hat{\mathbf{g}}^k)(\mathbf{g}_j^c \cdot \hat{\mathbf{g}}^l). \quad (2.43)$$

in which covariant base vectors are,

$$\hat{\mathbf{g}}_i = \frac{\partial \hat{\mathbf{x}}_m}{\partial r_i} \quad \text{with } i, j = 1, 2, \quad (2.44a)$$

$$\hat{\mathbf{g}}_3 = \mathbf{g}_3, \quad (2.44b)$$

and from covariant base vectors fixed in the in-plane directions,

$$\mathbf{g}_i^c = \frac{\partial \mathbf{x}}{\partial r_i}(0, 0, t), \quad (2.45)$$

the following contravariant base vectors are obtained,

$$\hat{\mathbf{g}}^i \cdot \hat{\mathbf{g}}_j = \delta_{ij}. \quad (2.46)$$

This replaces the covariant membrane strains obtained by Eq. (2.21) in the MITC4+ shell element. The resulting MITC4+N shell element has identical bending performances with the MITC4+ shell element, including the alleviation of membrane locking. The MITC4+N shell element exactly passes the membrane patch tests, and the membrane behavior is slightly improved. However, it is necessary to develop an ideal 4-node quadrilateral shell element showing nearly uniformly optimal convergence behavior. Therefore, the new MITC4+ shell element is developed.

2.1.4 The new MITC4+ shell element

The formulation of the new MITC4+ shell element [103] is presented here. The covariant membrane strains are represented using characteristic geometry and displacement vectors.

Using Eq. (2.2) in Eqs. (2.8a) and (2.8b), the following relations are obtained:

$$\frac{\partial \mathbf{x}_m}{\partial r} = \mathbf{x}_r + s\mathbf{x}_d, \quad \frac{\partial \mathbf{x}_m}{\partial s} = \mathbf{x}_s + r\mathbf{x}_d, \quad \frac{\partial \mathbf{u}_m}{\partial r} = \mathbf{u}_r + s\mathbf{u}_d, \quad \frac{\partial \mathbf{u}_m}{\partial s} = \mathbf{u}_s + r\mathbf{u}_d,$$

with

$$\begin{aligned} \mathbf{x}_r &= \frac{1}{4} \sum_{i=1}^4 \zeta_i \mathbf{x}_i, & \mathbf{x}_s &= \frac{1}{4} \sum_{i=1}^4 \eta_i \mathbf{x}_i, & \mathbf{x}_d &= \frac{1}{4} \sum_{i=1}^4 \zeta_i \eta_i \mathbf{x}_i, \\ \mathbf{u}_r &= \frac{1}{4} \sum_{i=1}^4 \zeta_i \mathbf{u}_i, & \mathbf{u}_s &= \frac{1}{4} \sum_{i=1}^4 \eta_i \mathbf{u}_i, & \mathbf{u}_d &= \frac{1}{4} \sum_{i=1}^4 \zeta_i \eta_i \mathbf{u}_i, \end{aligned} \quad (2.47)$$

in which the characteristic geometry vectors \mathbf{x}_r , \mathbf{x}_s and \mathbf{x}_d arise naturally from the nodal point positions, see Fig. 2.8, and the corresponding displacement vectors are \mathbf{u}_r , \mathbf{u}_s and \mathbf{u}_d .

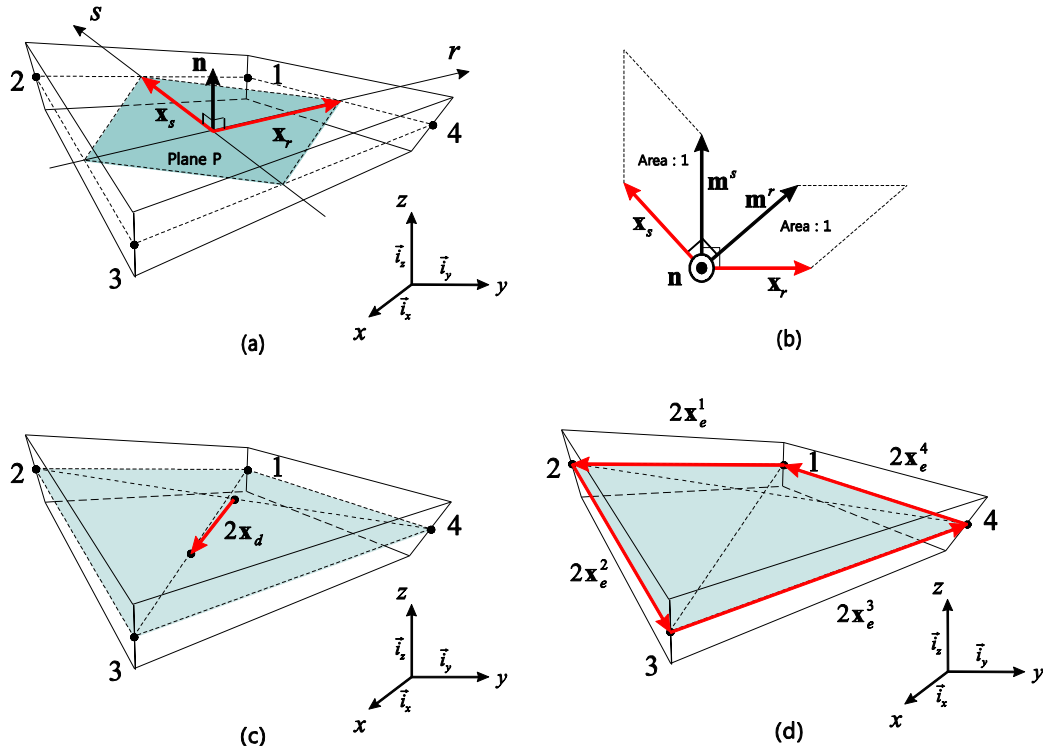


Fig. 2.8. The representative vectors from the element geometry. (a) The two in-plane vectors \mathbf{x}_r and \mathbf{x}_s , and the plane P with normal vector \mathbf{n} . (b) The two in-plane vectors \mathbf{m}^r and \mathbf{m}^s . (c) The distortion vector \mathbf{x}_d . (d) The four edge vectors \mathbf{x}_e^1 , \mathbf{x}_e^2 , \mathbf{x}_e^3 and \mathbf{x}_e^4 .

The two vectors \mathbf{x}_r and \mathbf{x}_s form the flat plane P with the normal vector

$$\mathbf{n} = \frac{\mathbf{x}_r \times \mathbf{x}_s}{\|\mathbf{x}_r \times \mathbf{x}_s\|}, \quad (2.48)$$

as shown in Fig. 2.8(a). For an arbitrarily distorted shell element, the plane P is the only flat surface that can be defined by equally accounting for the geometry of each nodal point, as required for passing the isotropy test. Since the two in-plane vectors, \mathbf{x}_r and \mathbf{x}_s , are not orthogonal, it is convenient to define their dual basis vectors, \mathbf{m}^r and \mathbf{m}^s on the plane P , such that

$$\mathbf{m}^{r_i} \cdot \mathbf{x}_{r_j} = \delta_j^i, \quad \mathbf{m}^{r_i} \cdot \mathbf{n} = 0 \quad \text{with } r_1 = r, \quad r_2 = s, \quad (2.49)$$

as shown in Fig. 2.8(b).

Since membrane locking occurs due to out-of-plane distortions of the element geometry, the ‘distortion vector’ \mathbf{x}_d , shown in Fig. 2.8(c), is of particular interest. The length of the distortion vector becomes nonzero for both in-plane and out-of-plane distortions of the element geometry. Note that the distortion vector can be decomposed into in-plane and out-of-plane components using the geometry vectors ($\mathbf{x}_r, \mathbf{x}_s$ and \mathbf{n}):

$$\mathbf{x}_d = (\mathbf{x}_d \cdot \mathbf{m}^r) \mathbf{x}_r + (\mathbf{x}_d \cdot \mathbf{m}^s) \mathbf{x}_s + (\mathbf{x}_d \cdot \mathbf{n}) \mathbf{n}, \quad (2.50)$$

in which the dual basis vectors \mathbf{m}^r and \mathbf{m}^s ‘measure’ the distortion in the direction of in-plane vectors \mathbf{x}_r and \mathbf{x}_s , the values $\mathbf{m}^r \cdot \mathbf{x}_d$ and $\mathbf{m}^s \cdot \mathbf{x}_d$ are the corresponding in-plane distortions, and $\mathbf{x}_d \cdot \mathbf{n}$ corresponds to the out-of-plane distortion.

In addition, the ‘edge vectors’ which lie along the element edges are

$$\begin{aligned} \mathbf{x}_e^1 &= \frac{\mathbf{x}_2 - \mathbf{x}_1}{2} = -\mathbf{x}_r - \mathbf{x}_d = -\frac{\partial \mathbf{x}_m}{\partial r}(0,1), \quad \mathbf{x}_e^2 = \frac{\mathbf{x}_3 - \mathbf{x}_2}{2} = -\mathbf{x}_s + \mathbf{x}_d = -\frac{\partial \mathbf{x}_m}{\partial s}(-1,0), \\ \mathbf{x}_e^3 &= \frac{\mathbf{x}_4 - \mathbf{x}_3}{2} = \mathbf{x}_r - \mathbf{x}_d = \frac{\partial \mathbf{x}_m}{\partial r}(0,-1), \quad \mathbf{x}_e^4 = \frac{\mathbf{x}_1 - \mathbf{x}_4}{2} = \mathbf{x}_s + \mathbf{x}_d = \frac{\partial \mathbf{x}_m}{\partial s}(1,0), \end{aligned} \quad (2.51)$$

see Fig. 2.8(d). The edge vectors form the corresponding edge strains,

$$e_{rr}^m(0,1) = \mathbf{x}_e^1 \cdot \mathbf{u}_e^1, \quad e_{rr}^m(0,-1) = \mathbf{x}_e^3 \cdot \mathbf{u}_e^3, \quad e_{ss}^m(1,0) = \mathbf{x}_e^4 \cdot \mathbf{u}_e^4, \quad e_{ss}^m(-1,0) = \mathbf{x}_e^2 \cdot \mathbf{u}_e^2, \quad (2.52)$$

in which each strain contains only two nodal displacements.

In the original displacement-based element formulation, four nodal displacements arise in the ‘ rr ’- and ‘ ss ’- membrane strains. However, constraints arise from the condition of vanishing membrane strains in pure bending situations. The use of edge strains in Eq. (2.52) is important to establish an improved behavior in bending-dominated problems.

The membrane strains in Eq. (2.7b) can be expressed using the characteristic geometry and displacement vectors

$$\begin{aligned}
e_{rr}^m &= e_{rr}^m|_{\text{con.}} + e_{rr}^m|_{\text{lin.}} \cdot s + e_{rs}^m|_{\text{bil.}} \cdot s^2, \\
e_{ss}^m &= e_{ss}^m|_{\text{con.}} + e_{ss}^m|_{\text{lin.}} \cdot r + e_{rs}^m|_{\text{bil.}} \cdot r^2, \\
e_{rs}^m &= e_{rs}^m|_{\text{con.}} + \frac{1}{2} e_{rr}^m|_{\text{lin.}} \cdot r + \frac{1}{2} e_{ss}^m|_{\text{lin.}} \cdot s + e_{rs}^m|_{\text{bil.}} \cdot rs
\end{aligned} \tag{2.53}$$

with

$$\begin{aligned}
e_{rr}^m|_{\text{con.}} &= \mathbf{x}_r \cdot \mathbf{u}_r, & e_{ss}^m|_{\text{con.}} &= \mathbf{x}_s \cdot \mathbf{u}_s, & e_{rs}^m|_{\text{con.}} &= \frac{1}{2} (\mathbf{x}_r \cdot \mathbf{u}_s + \mathbf{x}_s \cdot \mathbf{u}_r), \\
e_{rr}^m|_{\text{lin.}} &= \mathbf{x}_r \cdot \mathbf{u}_d + \mathbf{x}_d \cdot \mathbf{u}_r, & e_{ss}^m|_{\text{lin.}} &= \mathbf{x}_s \cdot \mathbf{u}_d + \mathbf{x}_d \cdot \mathbf{u}_s, & e_{rs}^m|_{\text{bil.}} &= \mathbf{x}_d \cdot \mathbf{u}_d.
\end{aligned} \tag{2.54}$$

in which the subscripts ‘con.’, ‘lin.’ and ‘bil.’ denote constant, linear and bilinear terms, respectively.

The following five strain components obtained at tying points are used to construct the assumed membrane strain field [2-5,84,85]

$$\begin{aligned}
e_{rr}^{m(A)} &= e_{rr}^m(0,1) = e_{rr}^m|_{\text{con.}} + e_{rr}^m|_{\text{lin.}} + e_{rs}^m|_{\text{bil.}}, & e_{rr}^{m(B)} &= e_{rr}^m(0,-1) = e_{rr}^m|_{\text{con.}} - e_{rr}^m|_{\text{lin.}} + e_{rs}^m|_{\text{bil.}}, \\
e_{ss}^{m(C)} &= e_{ss}^m(1,0) = e_{ss}^m|_{\text{con.}} + e_{ss}^m|_{\text{lin.}} + e_{rs}^m|_{\text{bil.}}, & e_{ss}^{m(D)} &= e_{ss}^m(-1,0) = e_{ss}^m|_{\text{con.}} - e_{ss}^m|_{\text{lin.}} + e_{rs}^m|_{\text{bil.}}, \\
e_{rs}^{m(E)} &= e_{rs}^m(0,0) = e_{rs}^m|_{\text{con.}},
\end{aligned} \tag{2.55}$$

which are effective to reduce membrane locking. The tying points (A), (B), (C), (D) and (E) as well as the corresponding strain components are shown in Fig. 2.9.

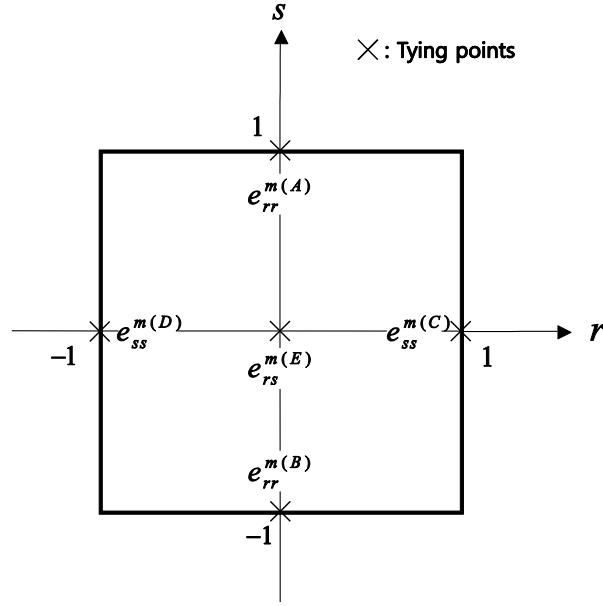


Fig. 2.9. Tying positions (A), (B), (C), (D) and (E) for the assumed membrane shear strain field.

Among the assumed membrane strain methods to alleviate membrane locking, membrane strain field proposed by Choi and Paik [2] is of particular interest, which was subsequently applied to an exact geometry shell element by Cho and Roh [4]

$$\begin{aligned}\bar{e}_{rr}^m &= \frac{1}{2}(e_{rr}^{m(A)} + e_{rr}^{m(B)}) + \frac{1}{2}(e_{rr}^{m(A)} - e_{rr}^{m(B)}) \cdot s = \left(e_{rr}^m \Big|_{\text{con.}} + e_{rs}^m \Big|_{\text{bil.}} \right) + e_{rr}^m \Big|_{\text{lin.}} \cdot s, \\ \bar{e}_{ss}^m &= \frac{1}{2}(e_{ss}^{m(C)} + e_{ss}^{m(D)}) + \frac{1}{2}(e_{ss}^{m(C)} - e_{ss}^{m(D)}) \cdot r = \left(e_{ss}^m \Big|_{\text{con.}} + e_{rs}^m \Big|_{\text{bil.}} \right) + e_{ss}^m \Big|_{\text{lin.}} \cdot r, \\ \bar{e}_{rs}^m &= \frac{1}{4}(e_{rs}^{m(A)} + e_{rs}^{m(B)} + e_{rs}^{m(C)} + e_{rs}^{m(D)}) = e_{rs}^{m(E)} = e_{rs}^m \Big|_{\text{con.}},\end{aligned}\tag{2.56}$$

That is, Choi and Paik used the five sampled strains in Eq. (2.55) to assume the membrane strain field to be one order lower than implicitly given in the original displacement-based element.

Linear terms are included in the covariant in-plane shear strain in Eq. (2.56) to obtain the following assumed membrane strain field

$$\hat{e}_{rr}^m = \bar{e}_{rr}^m, \quad \hat{e}_{ss}^m = \bar{e}_{ss}^m, \quad \hat{e}_{rs}^m = \bar{e}_{rs}^m + \frac{1}{2} e_{rr}^m \Big|_{\text{lin.}} \cdot r + \frac{1}{2} e_{ss}^m \Big|_{\text{lin.}} \cdot s.\tag{2.57}$$

Those linear terms are necessary for the shell element to pass the patch test.

Comparing the strain field in Eq. (2.57) with the strain field of the displacement-based element (giv-

en in Eq. (2.53)), the following relations are identified

$$e_{rr}^m = \hat{e}_{rr}^m - e_{rs}^m|_{\text{bil.}} + e_{rs}^m|_{\text{bil.}} \cdot s^2, \quad e_{ss}^m = \hat{e}_{ss}^m - e_{rs}^m|_{\text{bil.}} + e_{rs}^m|_{\text{bil.}} \cdot r^2, \quad e_{rs}^m = \hat{e}_{rs}^m + e_{rs}^m|_{\text{bil.}} \cdot rs, \quad (2.58)$$

from which the strain components added to the strain field in Eq. (2.57) (to complete the strain field of the displacement-based element) are identified to cause membrane locking. Note that all the added strain components contain the same term, $e_{rs}^m|_{\text{bil.}} = \mathbf{x}_d \cdot \mathbf{u}_d$ (given in Eq. (2.54)).

In order to establish an appropriate value for $e_{rs}^m|_{\text{bil.}}$, the idea of Kulikov and Plotnikova [3] are

adopted. Namely, the assumed membrane strain field is constructed by the linear combination of the five strain coefficients in Eq. (2.56) such as to keep the improved bending performance with the membrane locking alleviated

$$\tilde{e}_{rs}^m|_{\text{bil.}} = A \cdot (e_{rr}^m|_{\text{con.}} + e_{rs}^m|_{\text{bil.}}) + B \cdot (e_{ss}^m|_{\text{con.}} + e_{rs}^m|_{\text{bil.}}) + C \cdot e_{rs}^m|_{\text{con.}} + D \cdot e_{rr}^m|_{\text{lin.}} + E \cdot e_{ss}^m|_{\text{lin.}}, \quad (2.59)$$

where the coefficients (A, B, C, D and E) need to be determined. Note that the five strain coefficients can be easily obtained from the sampled strain components in Eq. (2.55).

To pass the membrane patch tests, the new membrane strain field should satisfy the following condition:

$$\tilde{e}_{rs}^m|_{\text{bil.}} = e_{rs}^m|_{\text{bil.}} \quad \text{when the element geometry is flat } (\mathbf{x}_d \cdot \mathbf{n} = 0) \quad (2.60)$$

for arbitrary in-plane deformation modes in the flat geometry.

For a flat element geometry with $\mathbf{x}_d \cdot \mathbf{n} = 0$ in the plane P defined in Eq. (2.48), the distortion vector in Eq. (2.50) becomes

$$\mathbf{x}_d = (\mathbf{x}_d \cdot \mathbf{m}^r) \mathbf{x}_r + (\mathbf{x}_d \cdot \mathbf{m}^s) \mathbf{x}_s. \quad (2.61)$$

Here, Eq. (2.60) are solved for arbitrary in-plane modes along with Eq. (2.61) to determine the five coefficients in Eq. (2.59).

The term $e_{rs}^m|_{\text{bil.}} = \mathbf{x}_d \cdot \mathbf{u}_d$ should become zero in the following deformation mode

$$\mathbf{u}_r = \mathbf{a}_r, \quad \mathbf{u}_s = \mathbf{a}_s, \quad \mathbf{u}_d = \mathbf{0}, \quad (2.62)$$

in which \mathbf{a}_r and \mathbf{a}_s are arbitrary constant vectors placed in the flat plane P .

From the condition in Eq. (2.60), the assumed membrane strain field in Eq. (2.59) also should be zero,

$$\tilde{e}_{rs}^m \Big|_{\text{bil.}} = 0 \quad (2.63)$$

in the deformation mode in Eq. (2.60).

Using Eq. (2.62) in Eq. (2.54), the five strain coefficients in Eq. (2.56) become

$$\begin{aligned} \left(e_{rr}^m \Big|_{\text{con.}} + e_{rs}^m \Big|_{\text{bil.}} \right) &= \mathbf{x}_r \cdot \mathbf{a}_r, \quad \left(e_{ss}^m \Big|_{\text{con.}} + e_{rs}^m \Big|_{\text{bil.}} \right) = \mathbf{x}_s \cdot \mathbf{a}_s, \quad e_{rs}^m \Big|_{\text{con.}} = \frac{1}{2} (\mathbf{x}_r \cdot \mathbf{a}_s + \mathbf{x}_s \cdot \mathbf{a}_r), \\ e_{rr}^m \Big|_{\text{lin.}} &= \mathbf{x}_d \cdot \mathbf{a}_r, \quad e_{ss}^m \Big|_{\text{lin.}} = \mathbf{x}_d \cdot \mathbf{a}_s. \end{aligned} \quad (2.64)$$

Substituting Eqs. (2.63) and (2.64) into Eq. (2.59), the following equation is obtained

$$\left(A \cdot \mathbf{x}_r + C \cdot \mathbf{x}_s / 2 + D \cdot \mathbf{x}_d \right) \cdot \mathbf{a}_r + \left(C \cdot \mathbf{x}_r / 2 + B \cdot \mathbf{x}_s + E \cdot \mathbf{x}_d \right) \cdot \mathbf{a}_s = 0$$

for arbitrary constant vectors \mathbf{a}_r and \mathbf{a}_s ,

and thus

$$A \cdot \mathbf{x}_r + C \cdot \mathbf{x}_s / 2 + D \cdot \mathbf{x}_d = \mathbf{0}, \quad C \cdot \mathbf{x}_r / 2 + B \cdot \mathbf{x}_s + E \cdot \mathbf{x}_d = \mathbf{0}. \quad (2.66)$$

Comparing Eq. (2.66) with Eq. (2.61), following constants are easily identified

$$A = c_r^2 / d, \quad B = c_s^2 / d, \quad C = 2c_r c_s / d, \quad D = -c_r / d, \quad E = -c_s / d \quad (2.67)$$

with $c_r = \mathbf{x}_d \cdot \mathbf{m}^r$, $c_s = \mathbf{x}_d \cdot \mathbf{m}^s$ and a new constant d . The values c_r and c_s denote the in-plane distortions of the element geometry.

Consequently,

$$\tilde{e}_{rs}^m \Big|_{\text{bil.}} = \frac{c_r^2}{d} \left(e_{rr}^m \Big|_{\text{con.}} + e_{rs}^m \Big|_{\text{bil.}} \right) + \frac{c_s^2}{d} \left(e_{ss}^m \Big|_{\text{con.}} + e_{rs}^m \Big|_{\text{bil.}} \right) + \frac{2c_r c_s}{d} e_{rs}^m \Big|_{\text{con.}} - \frac{c_r}{d} e_{rr}^m \Big|_{\text{lin.}} - \frac{c_s}{d} e_{ss}^m \Big|_{\text{lin.}}. \quad (2.68)$$

If another condition of $e_{rs}^m \Big|_{\text{bil.}} = \mathbf{x}_d \cdot \mathbf{x}_d$ in the following deformation mode

$$\mathbf{u}_r = \mathbf{0}, \quad \mathbf{u}_s = \mathbf{0}, \quad \mathbf{u}_d = \mathbf{x}_d, \quad (2.69)$$

is used for solving Eq. (2.60), the following equation should be satisfied,

$$\tilde{e}_{rs}^m \Big|_{\text{bil.}} = \mathbf{x}_d \cdot \mathbf{x}_d. \quad (2.70)$$

Using Eq. (2.69) in Eq. (2.54), the five strain coefficients in Eq. (2.56) become

$$\begin{aligned} \left(e_{rr}^m \Big|_{\text{con.}} + e_{rs}^m \Big|_{\text{bil.}} \right) &= \mathbf{x}_d \cdot \mathbf{x}_d, \quad \left(e_{ss}^m \Big|_{\text{con.}} + e_{rs}^m \Big|_{\text{bil.}} \right) = \mathbf{x}_d \cdot \mathbf{x}_d, \quad e_{rs}^m \Big|_{\text{con.}} = 0, \\ e_{rr}^m \Big|_{\text{lin.}} &= \mathbf{x}_r \cdot \mathbf{x}_d, \quad e_{ss}^m \Big|_{\text{lin.}} = \mathbf{x}_s \cdot \mathbf{x}_d. \end{aligned} \quad (2.71)$$

Substituting Eqs. (2.70) and (2.71) into Eq. (2.68), the constant d is determined as

$$d = c_r^2 + c_s^2 - 1, \quad (2.72)$$

which can be rewritten as

$$\begin{aligned} d &= (c_r + 1)(c_r - 1) + (c_s + 1)(c_s - 1) + 1 \\ &= [(\mathbf{x}_d + \mathbf{x}_r) \cdot \mathbf{m}^r][(\mathbf{x}_d - \mathbf{x}_r) \cdot \mathbf{m}^r] + [(\mathbf{x}_d + \mathbf{x}_s) \cdot \mathbf{m}^s][(\mathbf{x}_d - \mathbf{x}_s) \cdot \mathbf{m}^s] + 1. \end{aligned} \quad (2.73)$$

Using Eq. (2.51) in Eq. (2.73), the constant d becomes

$$d = (\mathbf{x}_e^2 \cdot \mathbf{m}^s)(\mathbf{x}_e^4 \cdot \mathbf{m}^s) + (\mathbf{x}_e^3 \cdot \mathbf{m}^r)(\mathbf{x}_e^1 \cdot \mathbf{m}^r) + 1. \quad (2.74)$$

The value d measures the distortion of pairs of edges within the element.

Substituting the obtained assumed strain term (given in Eq. (2.68)) into all added strain components in Eq. (2.58), the new assumed membrane strain field for the 4-node continuum mechanics based shell element are finally obtained,

$$\tilde{e}_{rr}^m = \hat{e}_{rr}^m - \tilde{e}_{rs}^m \Big|_{\text{bil.}} + \tilde{e}_{rs}^m \Big|_{\text{bil.}} \cdot s^2, \quad \tilde{e}_{ss}^m = \hat{e}_{ss}^m - \tilde{e}_{rs}^m \Big|_{\text{bil.}} + \tilde{e}_{rs}^m \Big|_{\text{bil.}} \cdot r^2, \quad \tilde{e}_{rs}^m = \hat{e}_{rs}^m + \tilde{e}_{rs}^m \Big|_{\text{bil.}} \cdot rs. \quad (2.75)$$

For an efficient implementation in computer codes, the assumed strain field in Eq. (2.75) can be rewritten as

$$\begin{aligned} \tilde{e}_{rr}^m &= \frac{1}{2}(1 - 2a_A + s + 2a_A \cdot s^2)e_{rr}^{m(A)} + \frac{1}{2}(1 - 2a_B - s + 2a_B \cdot s^2)e_{rr}^{m(B)} + a_C(-1 + s^2)e_{ss}^{m(C)} + \\ & a_D(-1 + s^2)e_{ss}^{m(D)} + a_E(-1 + s^2)e_{rs}^{m(E)}, \end{aligned} \quad (2.76a)$$

$$\begin{aligned}\tilde{e}_{ss}^m &= a_A(-1+r^2)e_{rr}^{m(A)} + a_B(-1+r^2)e_{rr}^{m(B)} + \frac{1}{2}(1-2a_C+r+2a_C \cdot r^2)e_{ss}^{m(C)} + \\ &\frac{1}{2}(1-2a_D-r+2a_D \cdot r^2)e_{ss}^{m(D)} + a_E(-1+r^2)e_{rs}^{m(E)},\end{aligned}\quad (2.76b)$$

$$\begin{aligned}\tilde{e}_{rs}^m &= \frac{1}{4}(r+4a_A \cdot rs)e_{rr}^{m(A)} + \frac{1}{4}(-r+4a_B \cdot rs)e_{rr}^{m(B)} + \frac{1}{4}(s+4a_C \cdot rs)e_{ss}^{m(C)} + \\ &\frac{1}{4}(-s+4a_D \cdot rs)e_{ss}^{m(D)} + (1+a_E \cdot rs)e_{rs}^{m(E)},\end{aligned}\quad (2.76c)$$

with

$$a_A = \frac{c_r(c_r-1)}{2d}, \quad a_B = \frac{c_r(c_r+1)}{2d}, \quad a_C = \frac{c_s(c_s-1)}{2d}, \quad a_D = \frac{c_s(c_s+1)}{2d}, \quad a_E = \frac{2c_r c_s}{d}.$$

Although the overall form of the assumed membrane strain resembles those previously published [2-5], Eq. (2.76) represents the formulation of a new continuum-mechanics based degenerated shell element, which is generally applicable for arbitrary geometry of the shell structure. In the next sections, excellent performances of the new MITC4+ shell element are presented.

Note that the membrane part of the new MITC4+ shell element is identical to that of the displacement-based element when the element geometry is flat. That is, in two-dimensional plane stress problems, both shell elements always yield the identical solutions. The computational cost of the new MITC4+ shell element increase slightly from that of the original MITC4 shell element. However, solution time does not change, and only the assembly cost is increased, see Table 2.1 for rough comparison.

Table 2.1. Relative comparison of assembly time.

Element	MITC4	MITC4+	New MITC4+
time	5.0	6.0	5.5

In the numerical analysis, $2 \times 2 \times 2$ Gauss integration over the element domain are used for the all the shell elements considered.

2.2 Basic tests

Here, results of the basic numerical tests to examine the MITC4+, MITC4+N and new MITC4+ shell element are presented. The isotropy, zero energy mode and patch tests are considered.

The spatially isotropic behavior is an important requirement for any shell elements. The element behavior should not depend on the sequence of node numbering, i.e. the element orientation [3,5-9,38]. All three elements pass this test.

Three patch tests of the membrane, bending and shearing patch tests are performed, see Refs. [1,5-9,14,19,30-34,36-40,101,102]. The mesh geometry is shown in Fig. 2.10. The patch of elements is subjected to the minimum number of constraints to prevent rigid body motions and the nodal point forces on the boundary corresponding to the constant stress states are applied. The patch tests are passed if the correct values of constant stress fields are calculated at any location within the mesh. Since the elements modify the membrane strain in Eq. (2.7b), membrane patch tests shown in Fig. 2.11 need special consideration.

For the MITC4+ shell element, bending and shearing while the membrane patch test is approximately passed, see Fig. 2.12. The MITC4+N and new MITC4+ elements pass all membrane, bending and shearing patch tests. It is already shown that the new MITC4+ shell element passes membrane patch test because it is identical to the displacement-based element for flat geometry. For other elements, pass membrane patch test can be proven through the methodology presented in Section 1.4.2.

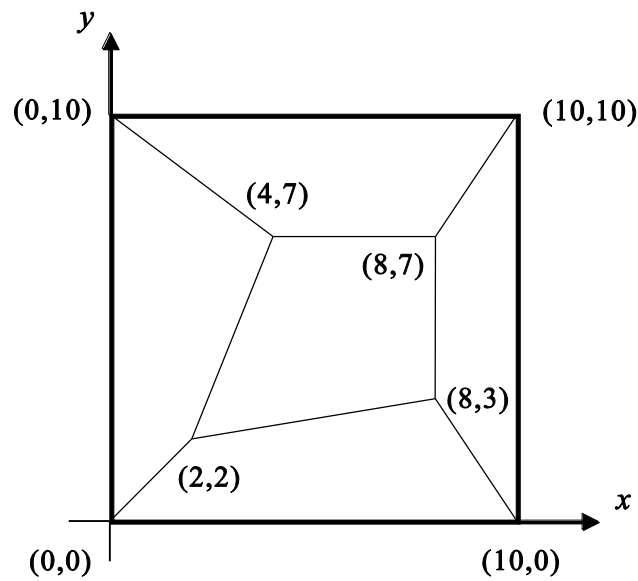


Fig. 2.10. Mesh geometry used for the patch tests.

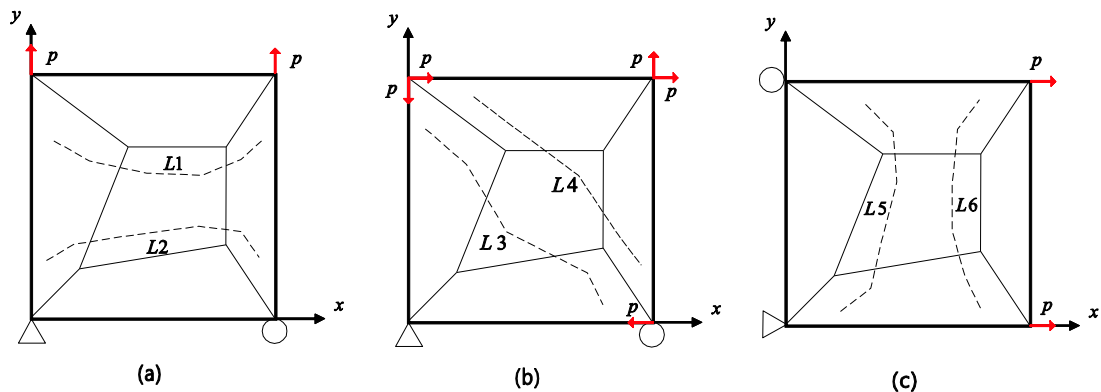


Fig. 2.11. Mesh geometry, loading and boundary conditions used for the membrane patch tests. The tensile patch tests are shown in (a) and (c), and shear patch test is shown in (b). The lines through element Gauss points for stress evaluation are shown in (a) to (c) ($p = 1.0$, thickness=1.0, $E = 2.1 \times 10^6$, $\nu = 0.3$).

In the zero energy mode tests, the number of zero eigenvalues of the stiffness matrix of a single unsupported element are counted [1,5-9,14,19,31,35,38-40]. For the new elements only the six zero eigenvalues corresponding to the six rigid body modes are obtained. That is, all three elements pass the zero energy mode tests.

In order to test the in-plane shearing mode of the shell elements, Cook's problem shown in Fig. 2.13 is considered. The results of tip displacements are shown in Table 2.2. While all shell elements con-

verges accurately toward the reference solution, the original MITC4 and the new MITC4+ shell element perform the best. We test in-plane bending modes of the shell elements under regular and distorted mesh using cantilever problem and thick curved beam problem shown in Fig. 2.14 and Fig. 2.15, respectively. The results of tip displacements are presented in Table 2.3 and Table 2.4. While all elements converges accurately toward the exact solutions, the original MITC4 and the new MITC4+ shell elements performs identically and better than the other elements.

All three shell elements does not have additional unknowns, and hence computationally efficient. Formulations of all three shell elements are relatively simple to implement and physically understandable. Note also that all three shell elements yield symmetric and positive definite stiffness matrices.

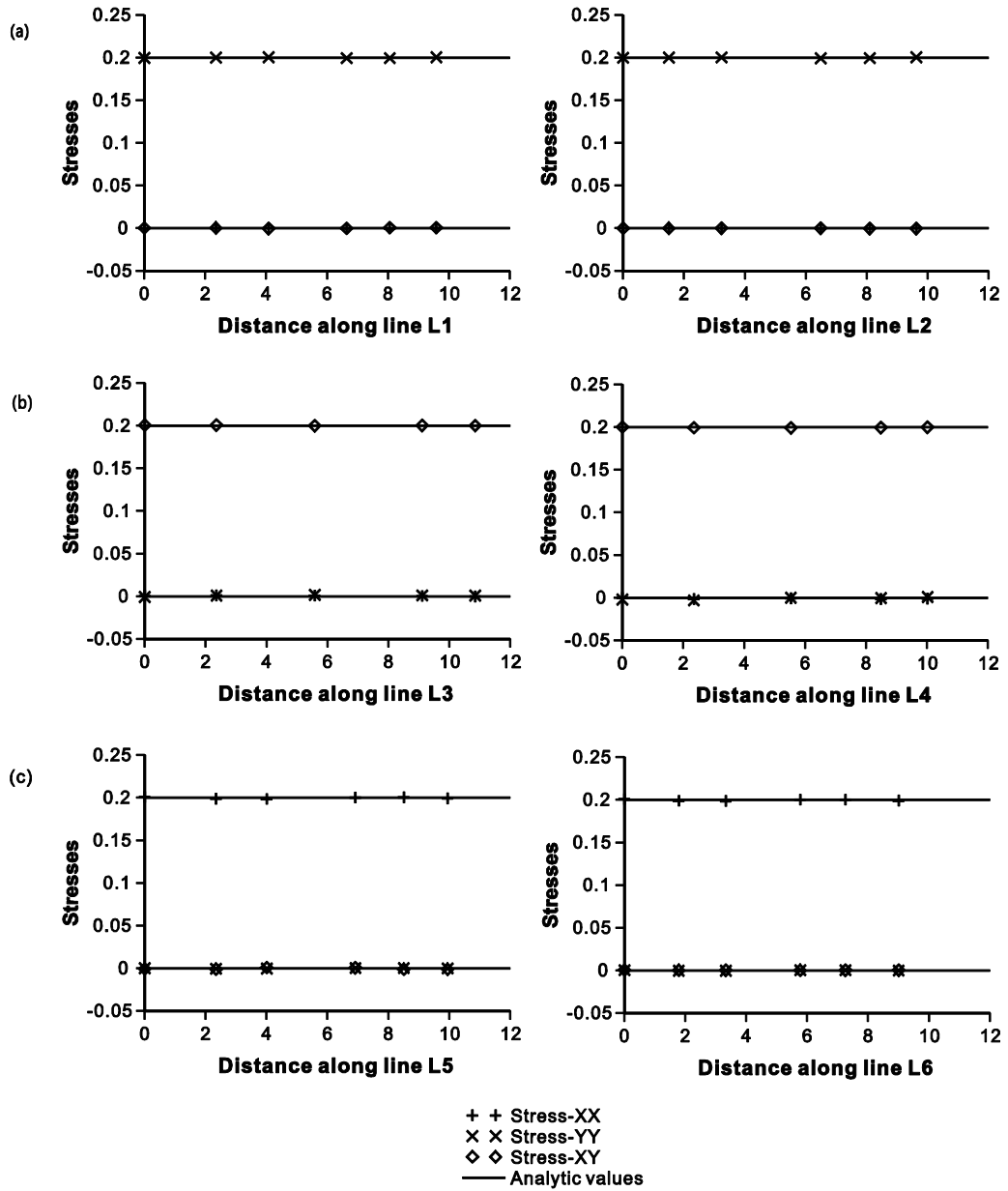


Fig. 2.12. Stresses along lines L1 to L6 for the membrane patch tests of the MITC4+ shell element.

Results of the patch tests in Fig. 2.11(a), (b) and (c) are shown in (a), (b) and (c), respectively.

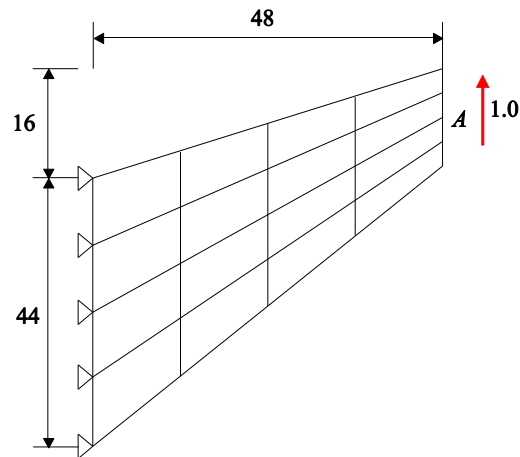


Fig. 2.13. Cook's problem. Plane stress condition is considered with $E = 1.0$ and $\nu = 1/3$. Geometry including the 4×4 mesh division, loading and boundary conditions are shown.

Table 2.2. Vertical displacements at the center of tip A for Cook's problem.

Elements	Mesh					Reference
	2x2	4x4	8x8	16x16	32x32	
MITC4	11.8452	18.2992	22.0792	23.4304	23.8176	23.9642
MITC4+	11.7291	18.2662	22.0751	23.4301	23.8176	
MITC4+N	11.8200	18.2934	22.0786	23.4304	23.8176	
New MITC4+	11.8452	18.2992	22.0792	23.4304	23.8176	

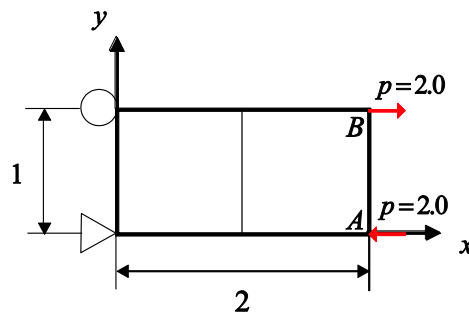


Fig. 2.14. Cantilever problem. Plane stress condition is considered with $E = 2.0 \times 10^5$ and $\nu = 0.0$. Geometry including the 1×2 mesh division, loading and boundary conditions are shown.

Table 2.3. Vertical displacements ($\times 10^{-4}$) at the tip A for cantilever problem.

Elements	Mesh			Exact
	1×2	1×4	1×8	
MITC4	-1.60	-2.13333	-2.32727	-2.40
MITC4+	-1.60	-2.13333	-2.32727	
MITC4+N	-1.60	-2.13333	-2.32727	
New MITC4+	-1.60	-2.13333	-2.32727	

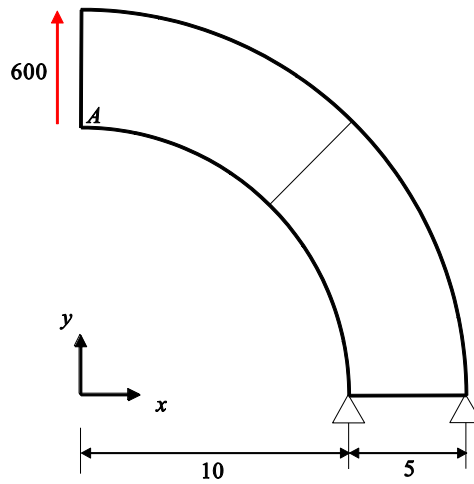


Fig. 2.15. Thick curved beam problem. Plane stress condition is considered with $E = 1.0 \times 10^3$ and $\nu = 0.0$. Geometry including the 1×2 mesh division, loading and boundary conditions are shown.

Table 2.4. Vertical displacements at the tip A for thick curved beam problem.

Elements	Mesh			Exact
	1×2	1×4	1×8	
MITC4	22.5988	57.9325	79.9218	90.1
MITC4+	22.7608	56.6258	76.5462	
MITC4+N	22.4383	57.6903	79.8095	
New MITC4+	22.5988	57.9325	79.9218	

2.3 Convergence studies

In this section, convergence studies are performed using appropriate and well-established benchmark problems to study the behavior of shell elements: a clamped square plate problem, cylindrical shell problems, and hyperboloid shell problems [5-9,11,12,18,19,22,60,100,108]. In addition, spherical shell problems newly established in our study is considered. The solution errors are measured in an appropriate norm considering membrane and bending-dominated shell problems with various curvatures, thicknesses, and boundary conditions. Hence the chosen problems are encompassing the typical difficulties encountered in shell analyses.

To measure the error in the finite element solution, the s-norm proposed by Hiller and Bathe [18] is employed

$$\|\mathbf{u} - \mathbf{u}_h\|_s^2 = \int_{\Omega} \Delta \boldsymbol{\varepsilon}^T \Delta \boldsymbol{\tau} d\Omega \quad \text{with} \quad \Delta \boldsymbol{\varepsilon} = \boldsymbol{\varepsilon} - \boldsymbol{\varepsilon}_h, \quad \Delta \boldsymbol{\tau} = \boldsymbol{\tau} - \boldsymbol{\tau}_h, \quad (2.77)$$

where \mathbf{u} is the exact solution, \mathbf{u}_h is the solution of the finite element discretization, and $\boldsymbol{\varepsilon}$ and $\boldsymbol{\tau}$ are the strain and stress vectors. This is a proper norm for investigating whether the finite element formulation satisfies the consistency and inf-sup conditions [12,16,18,21].

Since many good benchmark shell problems designed to detect locking have no analytical solution, an accurate finite element solution using a very fine mesh \mathbf{u}_{ref} is used to replace the exact solution \mathbf{u} . Hence the s-norm in Eq. (2.77) is modified to be

$$\|\mathbf{u}_{ref} - \mathbf{u}_h\|_s^2 = \int_{\Omega_{ref}} \Delta \boldsymbol{\varepsilon}^T \Delta \boldsymbol{\tau} d\Omega_{ref} \quad \text{with} \quad \Delta \boldsymbol{\varepsilon} = \boldsymbol{\varepsilon}_{ref} - \boldsymbol{\varepsilon}_h, \quad \Delta \boldsymbol{\tau} = \boldsymbol{\tau}_{ref} - \boldsymbol{\tau}_h. \quad (2.78)$$

To study the solution convergence of shell elements with decreasing thicknesses, the normalized relative error E_h are employed

$$E_h = \frac{\|\mathbf{u}_{ref} - \mathbf{u}_h\|_s^2}{\|\mathbf{u}_{ref}\|_s^2}. \quad (2.79)$$

The theoretical convergence behavior, which corresponds to the optimal convergence, is given by

$$E_h \cong Ch^k, \quad (2.80)$$

in which C is a constant independent of the shell thickness and h is the element size. For 4-node shell elements, $k = 2$.

In this study, well-converged reference solutions calculated using fine meshes of the MITC9 shell elements are used. The MITC9 shell element is known to satisfy the ellipticity and consistency conditions and to show good convergence behavior [12,18,108].

In each of the problem analyses the results obtained using the classical MITC4 shell element, the previously published and the new MITC4+ shell elements are given for the practical range of thickness of the shell element. Either uniformly regular or distorted meshes are employed to check sensitivity on the mesh distortion.

2.3.1 Fully clamped square plate problem

The plate bending problem [5-9,11,60,108] shown in Fig. 2.16 is considered. A square plate of dimensions $2L \times 2L$ and uniform thickness t is subjected to a uniform pressure. Utilizing the symmetry condition, only a one-quarter model is considered, with the following boundary conditions: $u_x = \theta_y = 0$ along BC, $u_y = \theta_x = 0$ along DC and $u_x = u_y = u_z = \theta_x = \theta_y = 0$ along AB and AD. In addition to the regular mesh in Fig. 2.16, the same plate bending problem with distorted meshes shown in Fig. 2.17 is considered. In $N \times N$ distorted mesh, each edge is discretized in the following ratio: $L_1 : L_2 : L_3 : \dots : L_N = 1 : 2 : 3 : \dots : N$.

Fig. 2.18 gives the convergence curves of the three shell elements. A 72×72 element mesh of the MITC9 shell element is used to obtain the reference solution. $N \times N$ element meshes are used with $N = 4, 8, 16, 32,$ and 64 to calculate the solutions. The element size in the convergence curves is $h = L / N$. The performance of the elements is uniformly optimal in both the regular and distorted meshes. Note that membrane locking is inherently not present in this plate bending problem.

2.3.2 Cylindrical shell problems

Cylindrical shell of length $2L$, radius R and uniform thickness t are considered as shown in Fig. 2.19(a), see Refs. [5-9,22]. The loading is a smoothly varying pressure $p(\theta)$

$$p(\theta) = p_0 \cos(2\theta), \quad (2.81)$$

see Fig. 2.19(b).

This shell structure shows two different asymptotic behaviors depending on the boundary conditions at its ends: bending-dominated behavior when both ends are free and membrane-dominated behavior when both ends are clamped.

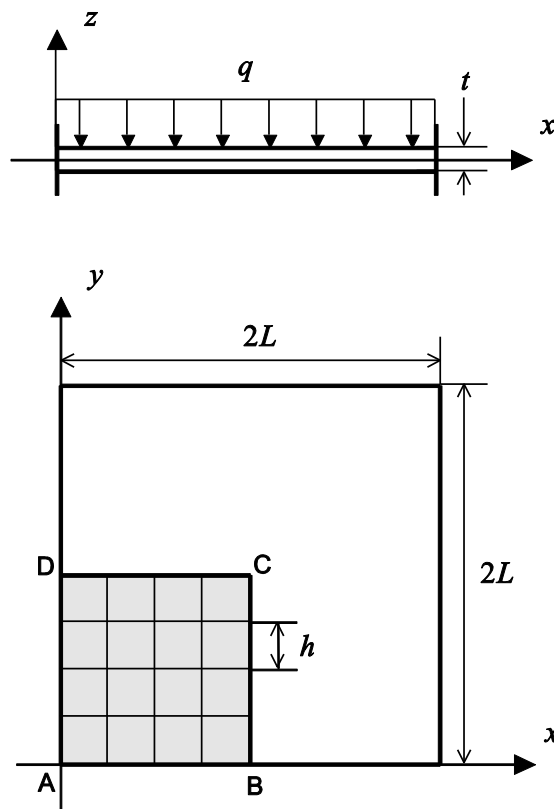


Fig. 2.16. Fully clamped square plate under uniform pressure ($L=1.0$, $E=1.7472 \times 10^7$, $q=1.0$ and $\nu=0.3$).

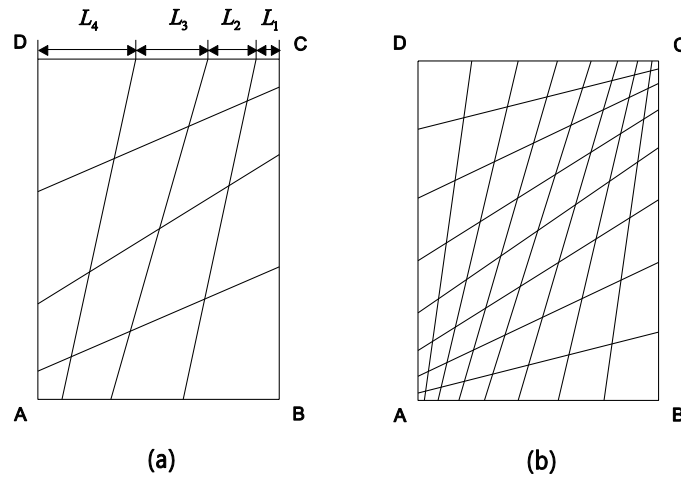
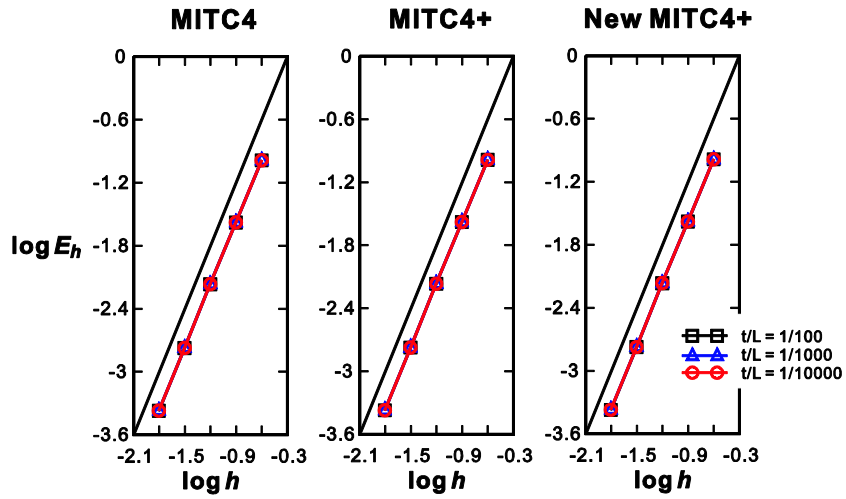
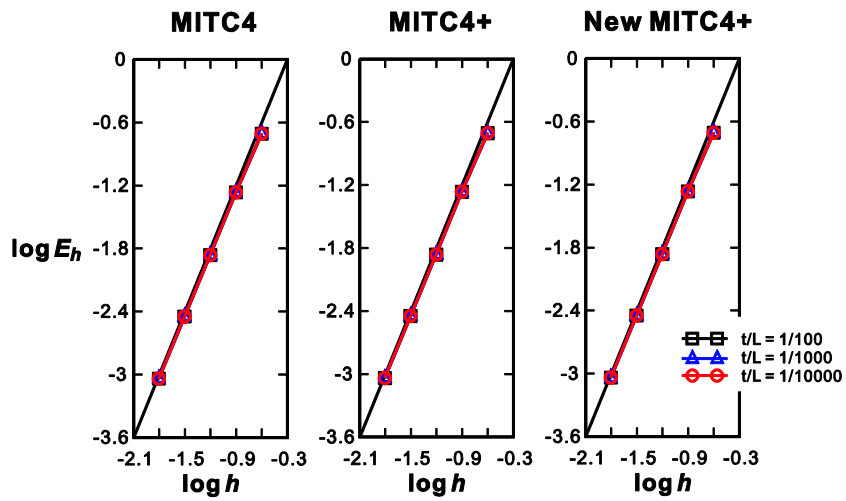


Fig. 2.17. Distorted mesh patterns for (a) $N = 4$ and (b) $N = 8$.

Using symmetry, only the region ABCD in Fig. 2.19(a) is modeled. For the membrane-dominated problem, the clamped boundary condition is imposed: For the membrane-dominated case, the clamped boundary condition is imposed: $u_z = \beta = 0$ along DC, $u_y = \beta = 0$ along AB, $u_x = \alpha = 0$ along AD, and $u_x = u_y = u_z = \alpha = \beta = 0$ along BC. For the bending-dominated case, the free boundary condition is imposed: $u_z = \beta = 0$ along DC, $u_y = \beta = 0$ along AB, and $u_x = \alpha = 0$ along AD. When using the clamped boundary condition, the regular mesh is graded with a boundary layer of width $2\sqrt{t}$, see Refs. [21,22] for details. In the free boundary condition, the graded mesh with a boundary layer of width $0.5\sqrt{t}$ is considered. The convergence studies using the distorted meshes shown in Fig. 2.19(c) are also performed.



(a)



(b)

Fig. 2.18. Convergence curves for the fully clamped square plate problem with (a) the regular and (b) distorted meshes shown in Fig. 2.17. The bold line represents the optimal convergence rate.

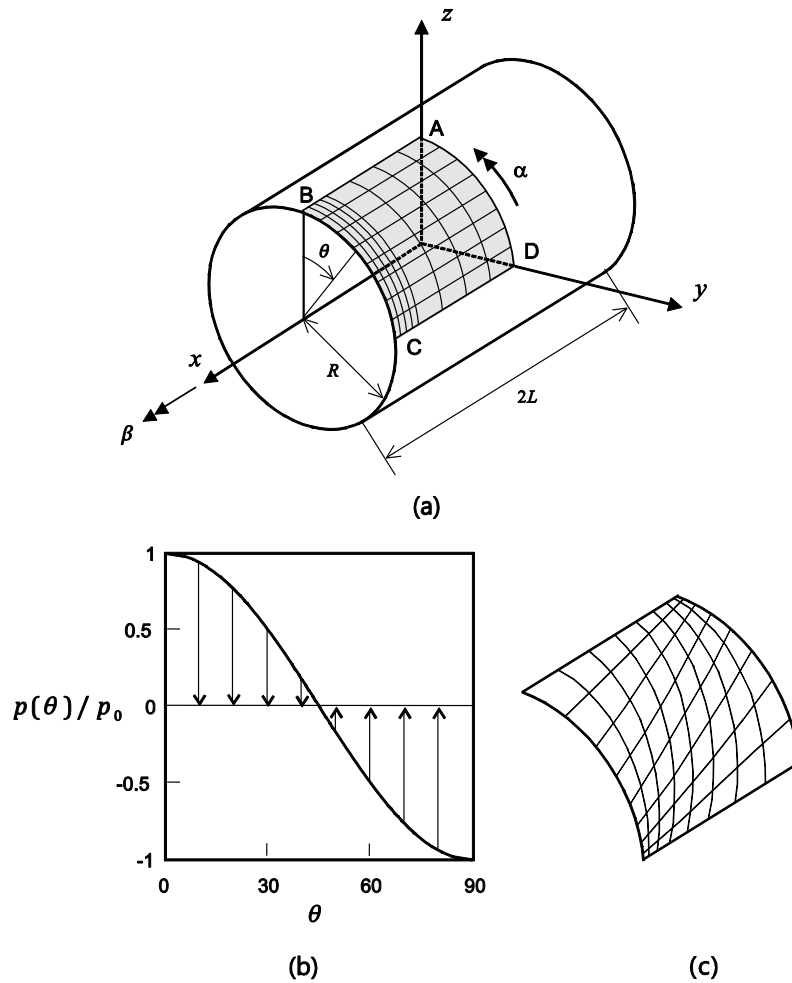


Fig. 2.19. Cylindrical shell problem ($L = R = 1.0$, $E = 2.0 \times 10^5$, $\nu = 1/3$ and $p_0 = 1.0$). (a) Problem description with graded mesh for the clamped case (8×8 mesh, $t/L = 1/100$). (b) Pressure loading. (c) Distorted mesh in Fig. 2.17 applied.

Fig. 2.20 gives the convergence curves in the solution of the clamped cylindrical shell problems. The reference solutions are calculated using a 72×72 element mesh of MITC9 shell elements. The solutions are obtained with $N \times N$ element meshes ($N = 4, 8, 16, 32$, and 64). The element size is $h = L/N$. In this problem, all shell elements present similarly good convergence behaviors.

Fig. 2.21 shows the convergence curves for the free cylindrical shell problems. Note that, in the regular meshes, all 4-node shell elements have a flat geometry, and thus membrane locking does not occur. However, in the distorted meshes, the element geometry is not flat, which induces membrane locking. In those cases, the performance of the MITC4 shell element severely deteriorates. The new MITC4+ shell element shows an excellent performance.

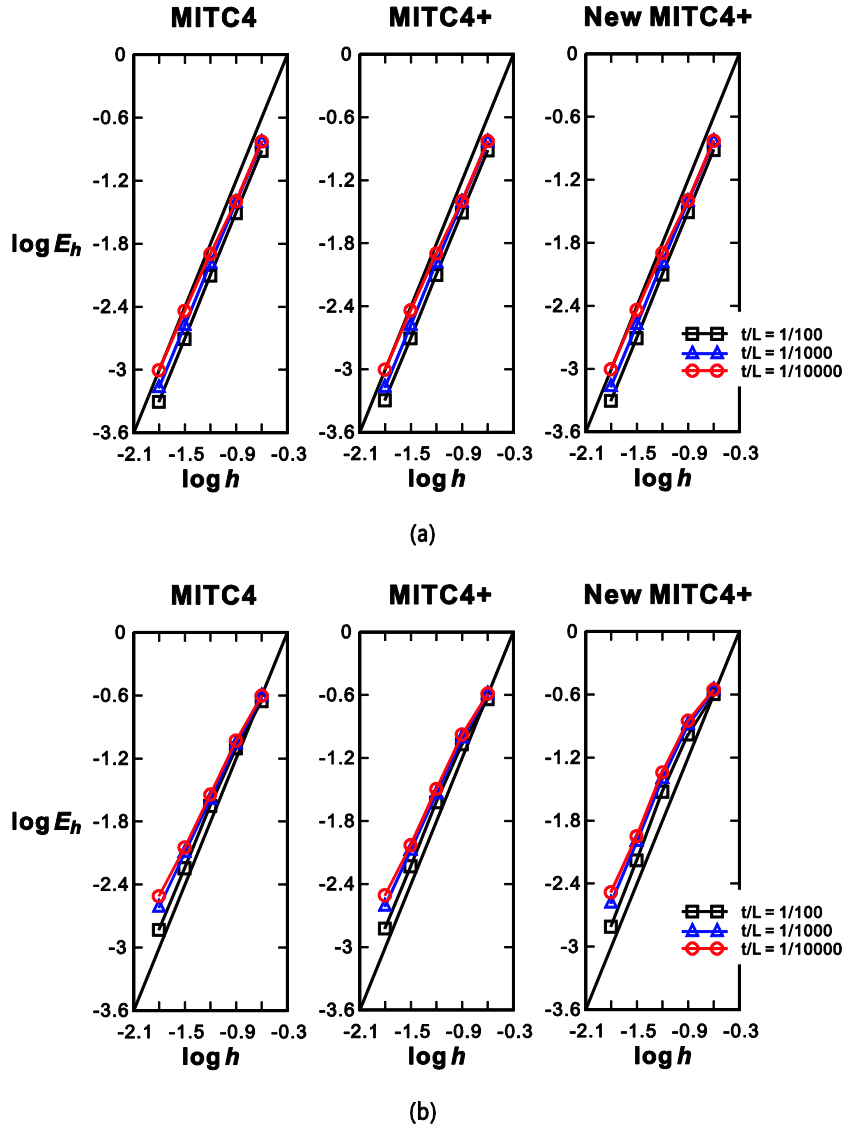


Fig. 2.20. Convergence curves for the clamped cylindrical shell problem with (a) the regular or (b) distorted meshes. The bold line represents the optimal convergence rate.

2.3.3 Hyperboloid shell problems

Here, the hyperboloid shell shown in Fig. 2.22(a) is considered, see Refs. [5-9,12,18,100]. The mid-surface of the shell structure is given by

$$x^2 + z^2 = 1 + y^2; \quad y \in [-1, 1]. \quad (2.82)$$

As for the cylindrical shell problems, a smoothly varying pressure in Eq. (2.81) is applied.

A bending-dominated behavior is obtained with free ends and a membrane-dominated behavior is

given with clamped ends, similar to the cases of the cylindrical shell.

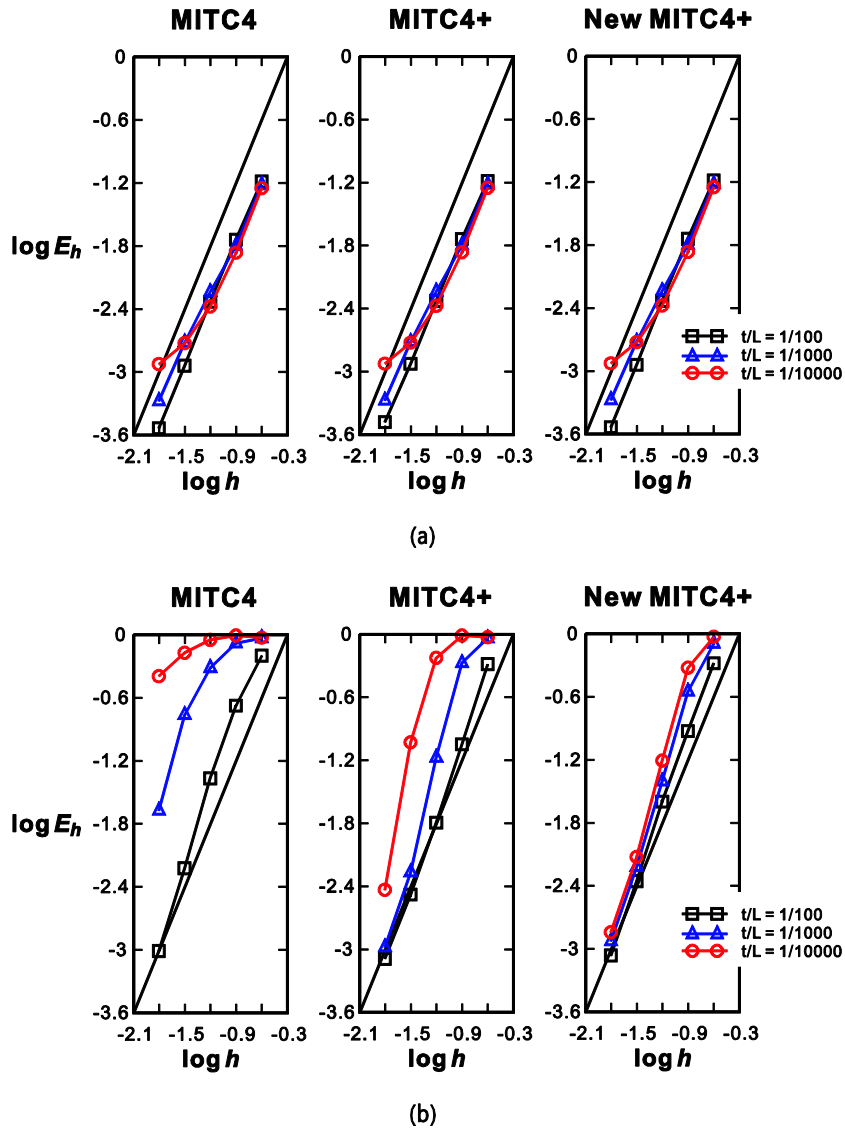


Fig. 2.21. Convergence curves for the free cylindrical shell problem with (a) the regular and (b) distorted meshes. The bold line represents the optimal convergence rate.

Due to symmetry, only one-eighth of the structure corresponding to the shaded region ABCD in Fig. 2.22(a) is modeled for the analysis. For the membrane-dominated case, the clamped boundary condition is imposed: $u_z = \beta = 0$ along DC, $u_x = \beta = 0$ along AB, $u_y = \alpha = 0$ along AD, and $u_x = u_y = u_z = \alpha = \beta = 0$ along BC. For the bending-dominated case, the free boundary condition is imposed: $u_z = \beta = 0$ along DC, $u_x = \beta = 0$ along AB, and $u_y = \alpha = 0$ along AD.

In both cases, a 72×72 element mesh of MITC9 shell elements is used to obtain the reference solu-

tions. The solutions are calculated using $N \times N$ element meshes ($N = 4, 8, 16, 32$ and 64). The element size is $h = L/N$. For the clamped boundary condition, the regular mesh graded in a boundary layer of width $6\sqrt{t}$ shown in Fig. 2.22(b) is considered, see Refs. [7,18,21]. For the free boundary condition, the regular mesh is graded in a boundary layer of width $0.5\sqrt{t}$ [18,21]. The convergence studies with the distorted meshes shown in Fig. 2.22(c) are also performed.

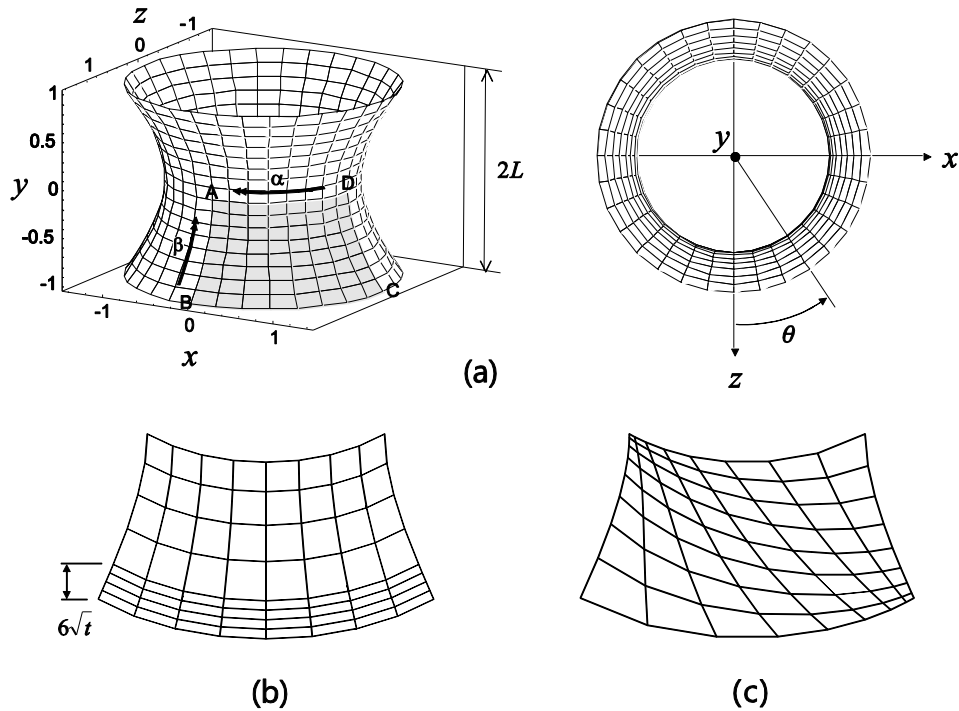


Fig. 2.22. Hyperboloid shell problem ($E = 2.0 \times 10^{11}$, $\nu = 1/3$, $L = 1.0$ and $p_0 = 1.0$). (a) Problem description. (b) Graded mesh for the clamped case (8×8 mesh, $t/L = 1/1000$). (c) Distorted mesh in Fig. 2.17 applied.

Fig. 2.23 shows the good convergence behavior of all elements in the solution of the clamped hyperboloid shell problem. Fig. 2.24 shows the convergence curves for the solution of the free hyperboloid shell problem. While all shell elements behave well when using the regular meshes, the convergence behavior of the MITC4 and previously published MITC4+ shell element deteriorate when using the distorted meshes. However, the new MITC4+ shell element shows an almost uniformly optimal and thus ideal convergence behavior.

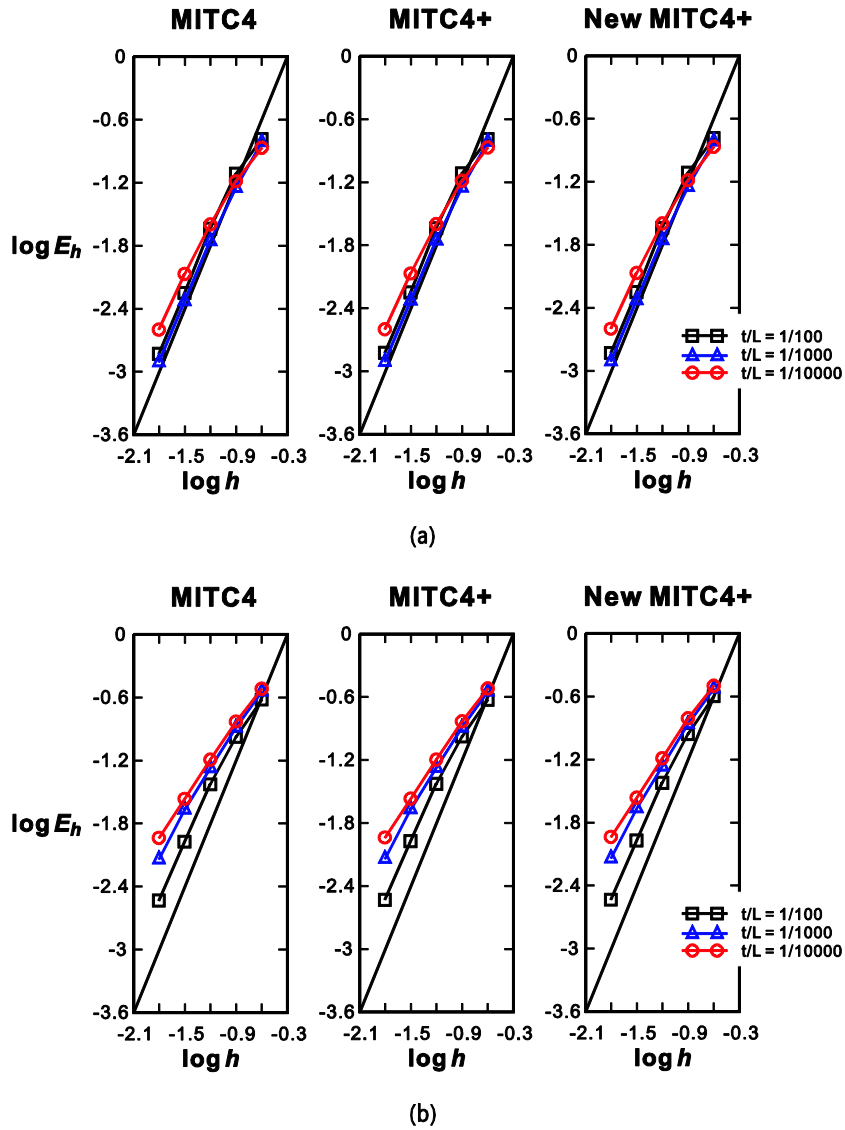


Fig. 2.23. Convergence curves for the clamped hyperboloid shell problem with (a) the regular and (b) distorted meshes. The bold line represents the optimal convergence rate.

2.3.4 Spherical shell problems

Finally, the spherical shell of radius R shown in Fig. 2.25(a) is considered. The spherical shell has 18° circular cutouts at its top and bottom. The varying pressure in Eq. (2.81) with the azimuthal angle θ is applied.

A bending-dominated behavior is obtained with free ends and a membrane-dominated behavior is given with clamped ends, similar to the cylindrical and hyperboloid shell problems.

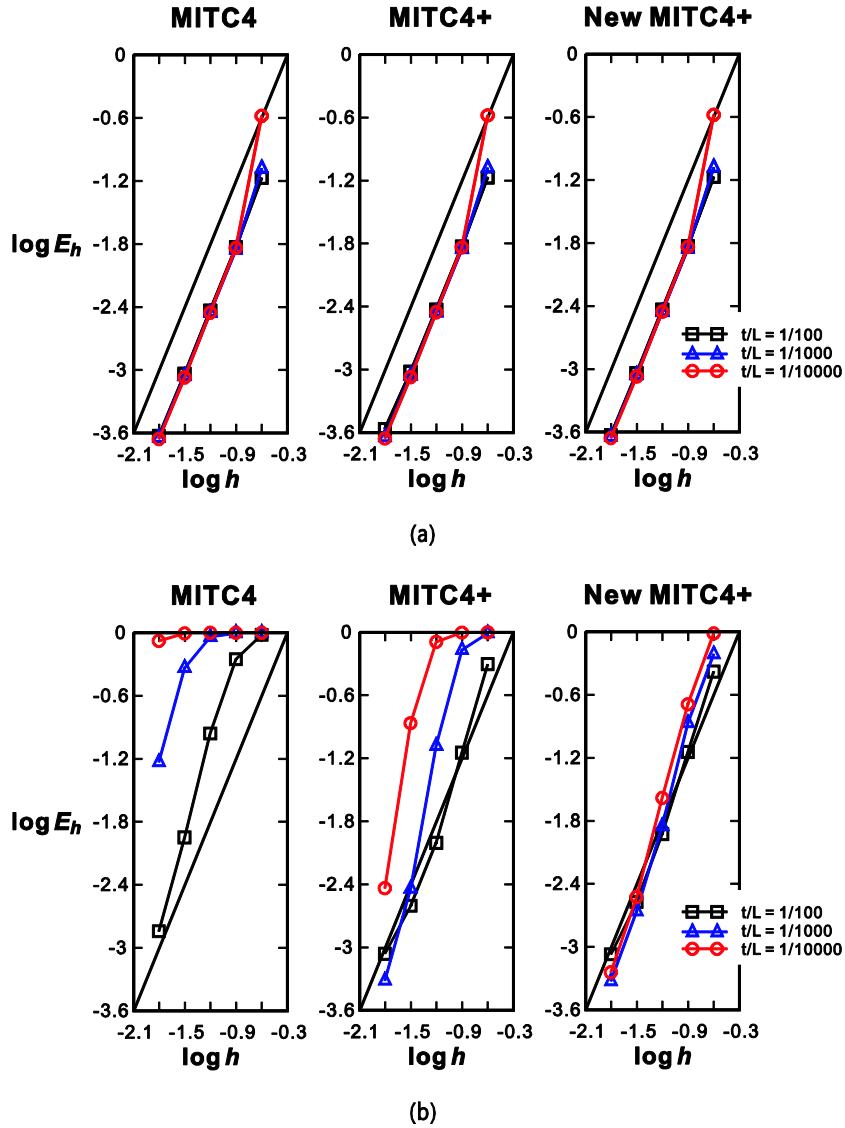


Fig. 2.24. Convergence curves for the free hyperboloid shell problem with (a) the regular and (b) distorted meshes. The bold line represents the optimal convergence rate.

Utilizing the symmetry, only one-eighth of the structure corresponding to the shaded region ABCD in Fig. 2.25(a) is modeled for the analysis. For the membrane-dominated case, the clamped boundary condition is imposed: $u_x = \beta = 0$ along BC, $u_y = \beta = 0$ along AD, $u_z = \alpha = 0$ along AB, and $u_x = u_y = u_z = \alpha = \beta = 0$ along DC. For the bending-dominated case, the free boundary condition is imposed: $u_x = \beta = 0$ along BC, $u_y = \beta = 0$ along AD, and $u_z = \alpha = 0$ along AB. In the free boundary condition, the regular mesh graded in a boundary layer of angle $\varphi_1 = 2.5^\circ t^{-0.2}$ shown in Fig. 2.25(b) is considered. The convergence studies with the distorted meshes shown in Fig. 2.25(c) are also performed.

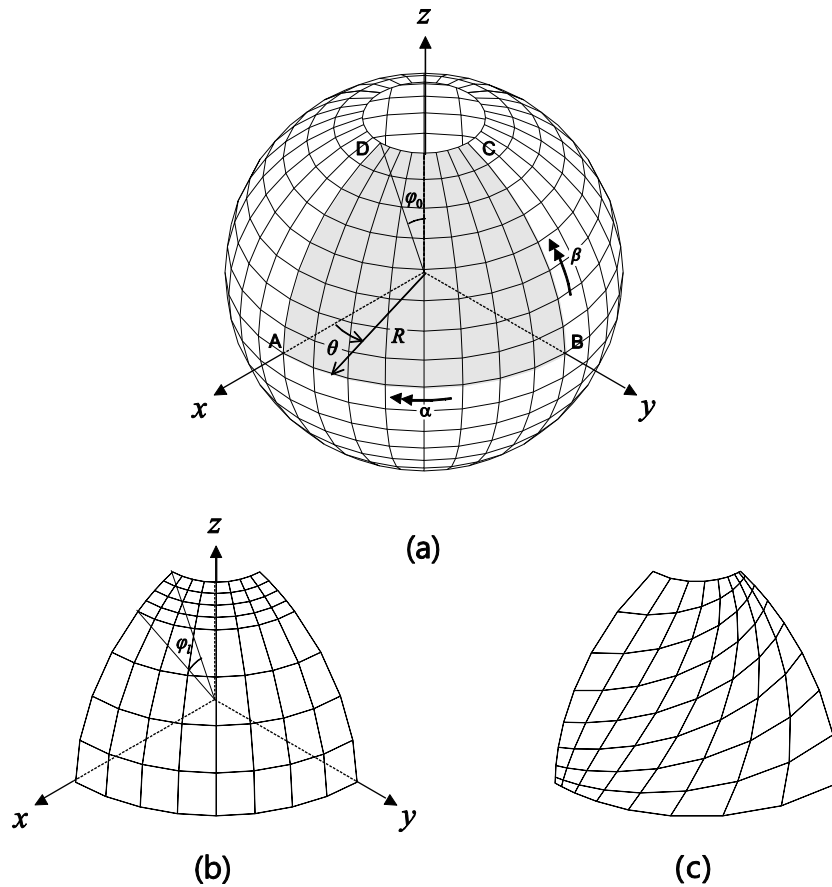
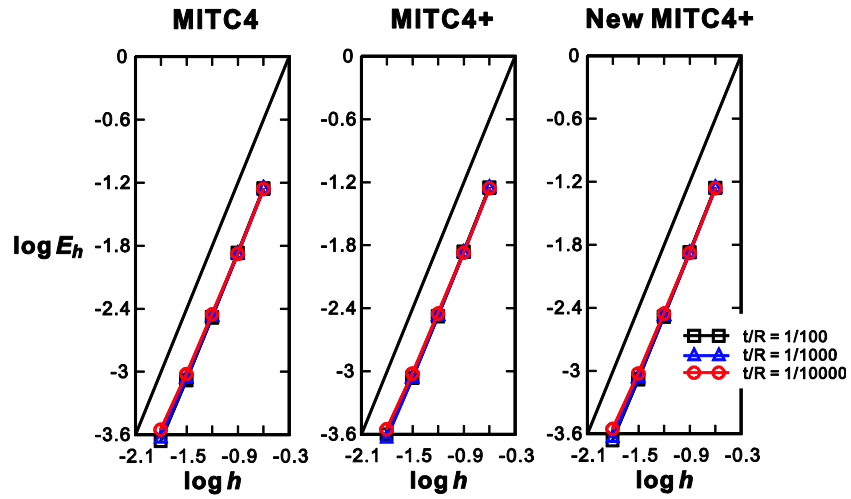


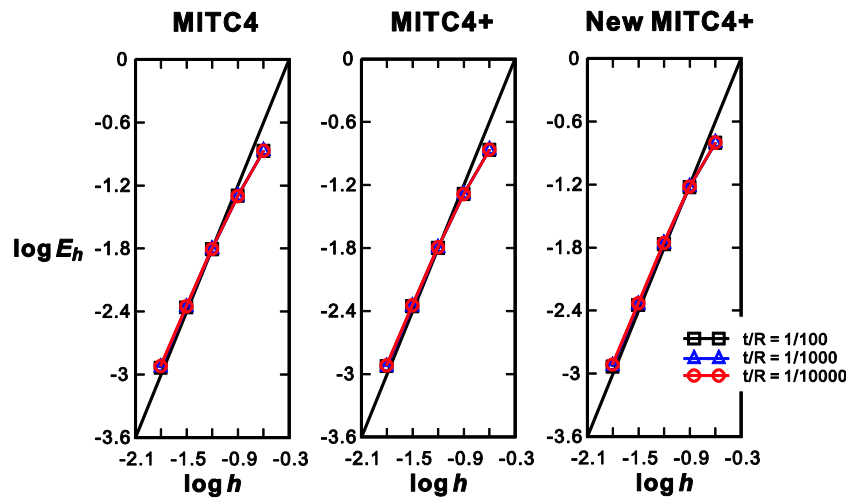
Fig. 2.25. Spherical shell problem ($E = 2.0 \times 10^{11}$, $\nu = 1/3$, $R = 1.0$, $\phi_0 = 18^\circ$ and $p_0 = 1.0$). (a) Problem description. (b) Graded mesh for the free case (8×8 mesh, $t/R = 1/10000$). (c) Distorted mesh in Fig. 2.17 applied.

Fig. 2.26 presents the convergence curves in the solution of the clamped spherical shell problem. The reference solutions are calculated using a 72×72 element mesh of MITC9 shell elements. The solutions are obtained with $N \times N$ element meshes ($N = 4, 8, 16, 32$, and 64). The element size is $h = R/N$. All shell elements present similarly good convergence behaviors.

Fig. 2.27 shows the convergence curves for the free spherical shell problem. In the regular meshes, all elements perform equally very well. However, in the distorted meshes, the convergence behavior of the MITC4 and previously published MITC4+ shell elements deteriorate. In this problem, the new MITC4+ shell element still shows an excellent performance.



(a)



(b)

Fig. 2.26. Convergence curves for the clamped spherical shell problem with (a) the regular and (b) distorted meshes. The bold line represents the optimal convergence rate.

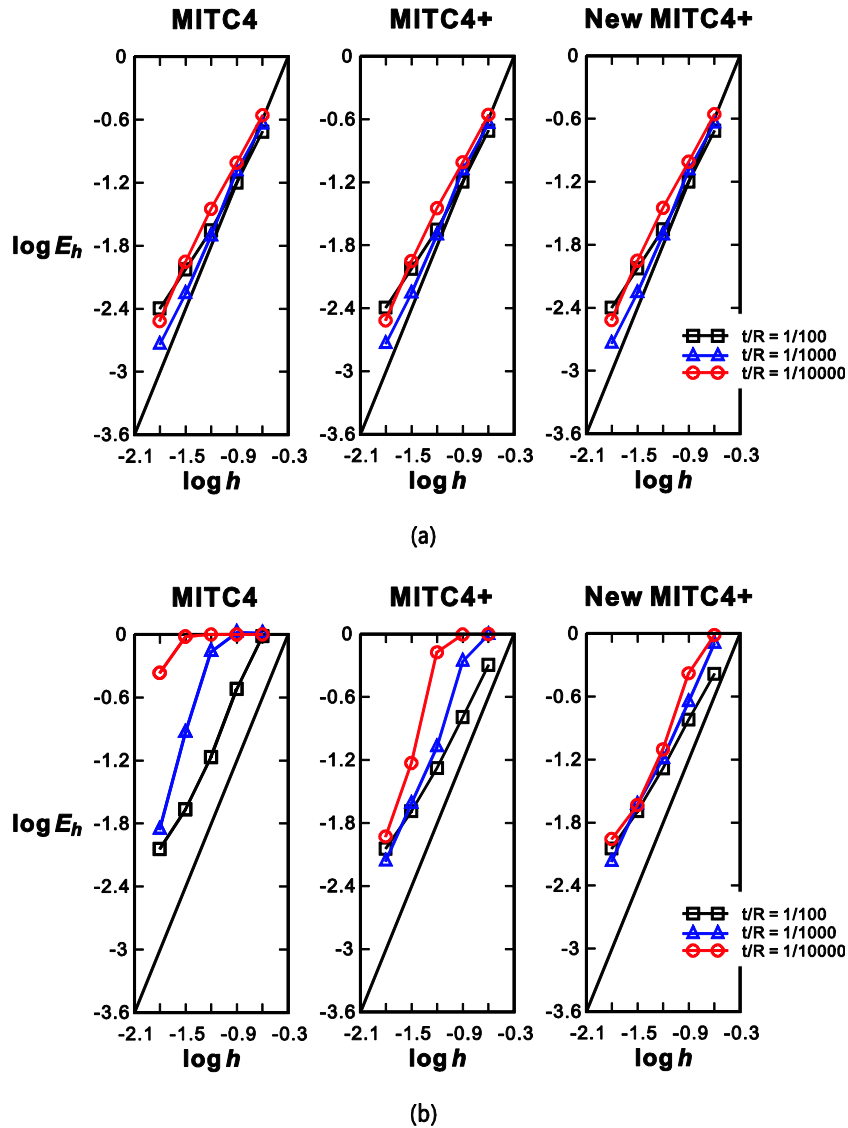


Fig. 2.27. Convergence curves for the free spherical shell problem with (a) the regular and (b) distorted meshes. The bold line represents the optimal convergence rate.

2.4 Classical benchmark tests

Here, a set of widely-used linear benchmark problems are presented to test the proposed shell elements. The problems considered are the twisted beam problem, hemispherical shell problem and pinched cylinder problem. As in the literature, convergence is measured using a representative displacement in a specific location of the shell structure.

The solutions of the new 4-node quadrilateral shell element are compared with the 4-node S4 and S4R shell elements used in the commercial software ABAQUS [109]. Note that unlike the S4 ele-

ment employing the full numerical integration ($2 \times 2 \times 2$ Gauss integration), the S4R element require undesirable stabilization matrix as well as displacement projection method because of the reduced integration applied.

2.4.1 Twisted beam problem

The twisted beam problem [34,36,38,40,110,111] shown in Fig. 2.28 is considered. A cantilever beam of length $L=12$, width $w=1.1$, and twist of 90° is loaded by concentrated out-of-plane load P at the center of free tip, point A. The material properties are $E = 2.9 \times 10^7$ and $\nu = 0.22$. The two different thicknesses, $t=0.32$ and $t=0.0032$ are considered.

The whole beam is modeled with $N \times 6N$ meshes are used with $N = 4, 8, 16, 32$ and 64 . For $t=0.32$ and $t=0.0032$, $P=1.0$ and $P=1.0 \times 10^{-6}$ are respectively used and the reference deflections at point A are $w_{ref} = 0.1754 \times 10^{-2}$ and $w_{ref} = 0.1294 \times 10^{-2}$, respectively [110].

Fig. 2.29 shows the convergence of the normalized vertical deflections (w_A / w_{ref}) according to the mesh division N . All shell elements show nearly identical performances.

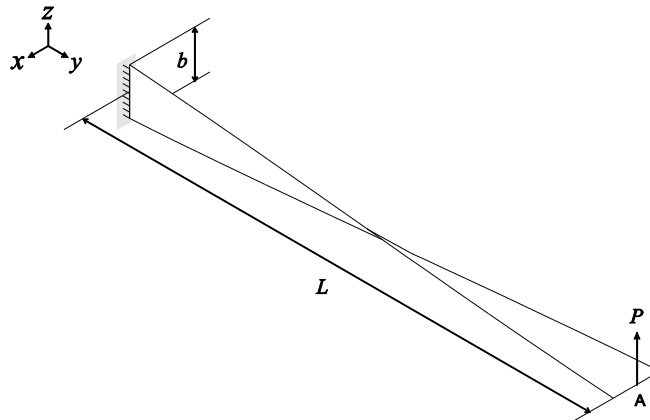


Fig. 2.28. Twisted beam problem.

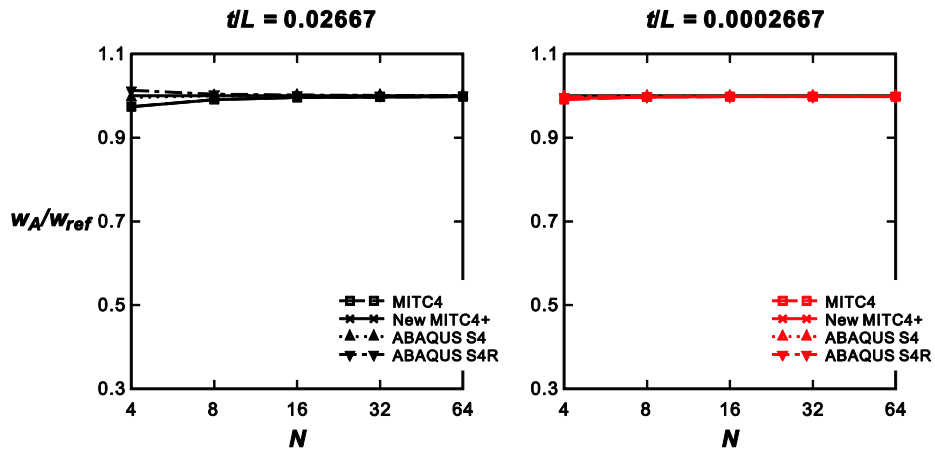


Fig. 2.29. Convergence of the normalized vertical deflections for the twisted beam problem. The horizontal lines represent the exact vertical deflection.

2.4.2 Pinched cylinder problem

The pinched cylinder problem [1,10,30,35,36,38,39,97,110,111], shown in Fig. 2.30, is considered. The cylinder structure of length $L = 600$, radius $R = 300$ and thickness $t = 3$ is supported by rigid diaphragms along its ends and is subjected to a pair of pinching forces, $F = 1.0$. The material properties used are $E = 3.0 \times 10^6$ and $\nu = 0.3$.

Only one-eighth of the structure corresponding to the shaded region ABCD in Fig. 2.30 is modeled. The boundary conditions are $u = 0$ along the edge AB, $v = 0$ along the edge AD, $w = 0$ along the edge CD, and $u = w = 0$ along the edge BC. $N \times N$ meshes are used with $N = 4, 8, 16, 32$ and 64 . The reference deflections at point A is $w_{ref} = 1.825 \times 10^{-5}$.

Fig. 2.31 shows the convergence of the normalized vertical deflections (w_A / w_{ref}) according to the mesh division N . The performance of reduced integrated shell element (S4R) is slightly better than other full-integrated shell elements.

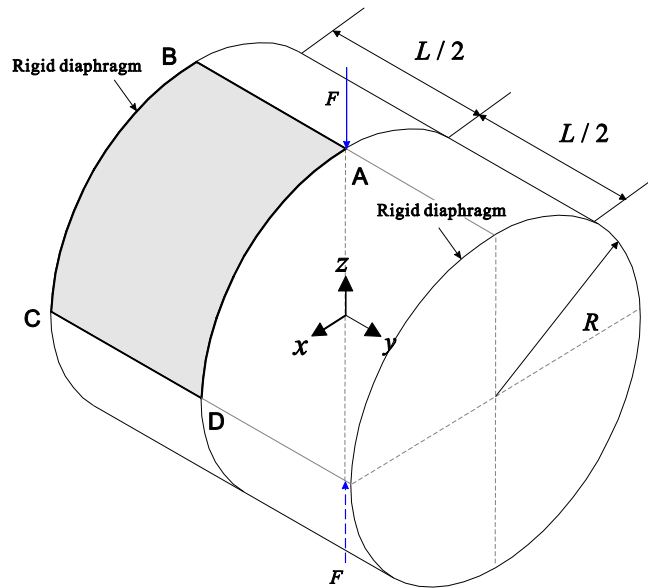


Fig. 2.30. Pinched cylinder problem.

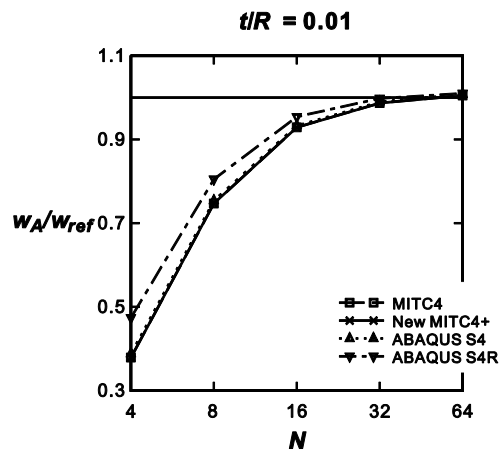


Fig. 2.31. Convergence of the normalized vertical deflections for the pinched cylinder problem. The horizontal lines represent the exact vertical deflection.

2.4.3 Hemispherical shell problem

We solve hemispherical shell problem [10,14] shown in Fig. 2.32. The spherical shell with radius $R=10.0$, thickness $t=0.04$ and 18° cutout at its pole is subjected to alternating radial forces $P=2.0$ s at its equator. The material properties used are $E=6.825 \times 10^7$ and $\nu=0.3$. In this bending problem, the shell structure undergoes almost inextensional deformation, hence providing a

mean to test membrane locking.

Due to symmetry, only one quarter of the structure corresponding to the shaded region ABCD in Fig. 2.32 is modeled, using $N \times N$ meshes with $N = 4, 8, 16, 32$ and 64 . We use the following boundary conditions: $u = \beta = 0$ along BC, $v = \beta = 0$ along AD, and $w = 0$ at any single node. The reference deflections at point A is $u_{ref} = 0.0924$.

Fig. 2.33 shows the convergence of the normalized deflections (u_A / u_{ref}) according to the mesh division N . While the reduced integrated shell element (S4R) shows fastest convergence of displacement, the new MITC4+ shell element performs slightly better than the S4 shell element.

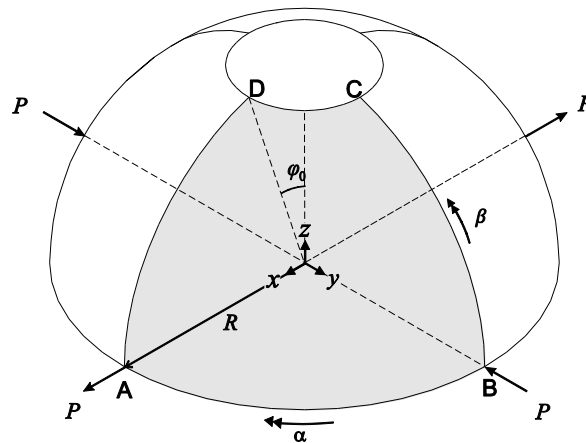


Fig. 2.32. Hemispherical shell problem.

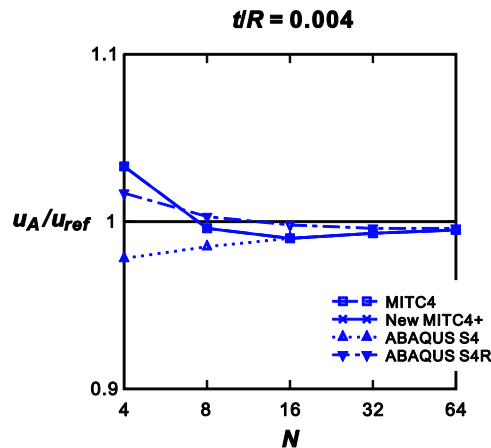


Fig. 2.33. Convergence of the normalized vertical deflections for the hemispherical shell problem.

The horizontal lines represent the exact vertical deflection.

2.5 Geometric nonlinear analysis

Here we present performance of new MITC4+ shell element in geometric nonlinear analysis [112]. We use the solutions obtained from fine mesh of the MITC9 shell element as the reference. The numerical results are compared with the classical MITC4 shell element. Here, new MITC4+ shell element is simply referred as MITC4+ shell element.

2.5.1 Cantilever bending problem

Bending problem of cantilever [1,13,32,113-116] is considered, see Fig. 2.34. The cantilever fully clamped at one end is subjected to either shearing force P or bending moment M at free tip. The cantilever is modeled with 16×1 meshes of the shell elements. The material properties are $E = 1.2 \times 10^6$ and $\nu = 0.0$. The cantilever has width $b = 1.0$, thickness $h = 0.1$, and length $L = 10.0$ for shearing load and $L = 12.0$ for moment load case.

For the shearing load case, the reference solution is obtained by fine 32×1 mesh of the MITC9 shell elements. We consider maximum load of $P_{\max} = 4P_0$ with $P_0 = EI/L$ and $I = bt^3/12$.

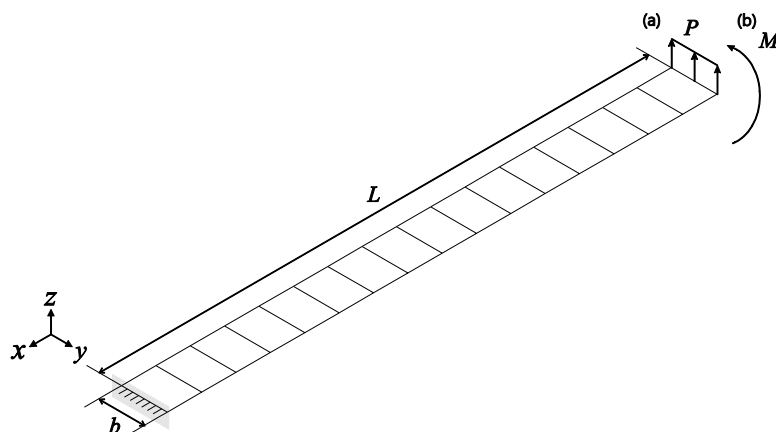


Fig. 2.34. Cantilever bending problem (16×1 mesh). (a) Case of tip shearing force. (b) Case of tip moment.

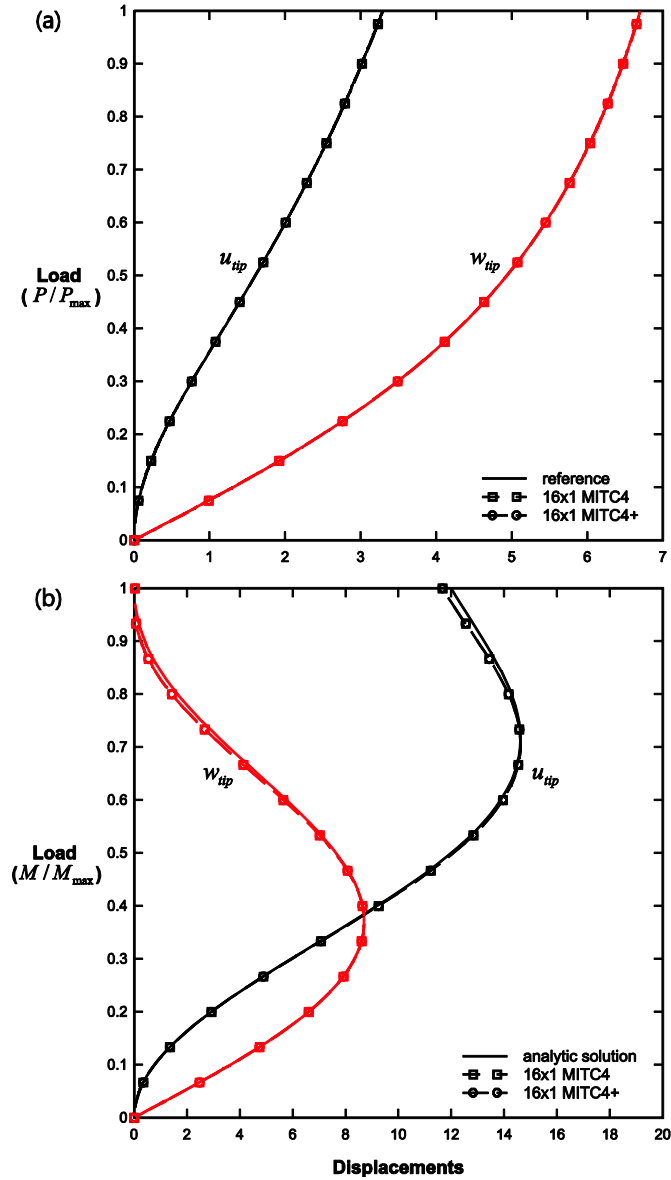


Fig. 2.35. Load-displacement curves for the cantilever (a) under tip shearing force and (b) under tip moment.

For the moment load case, the cantilever forms a circular arc with its radius R from the flexural formula $R = EI / M$ with $I = bt^3 / 12$. Using this formula, the following analytical tip displacements are obtained [115,116]

$$\frac{u_{tip}}{L} = \frac{M_0}{M} \sin \frac{M}{M_0} - 1, \quad \frac{w_{tip}}{L} = \frac{M_0}{M} \left(1 - \cos \frac{M}{M_0} \right), \quad M_0 = \frac{EI}{L}. \quad (2.83)$$

The cantilever should bend into complete circle when the maximum tip moment $M_{max} = 2\pi M_0$ is applied.

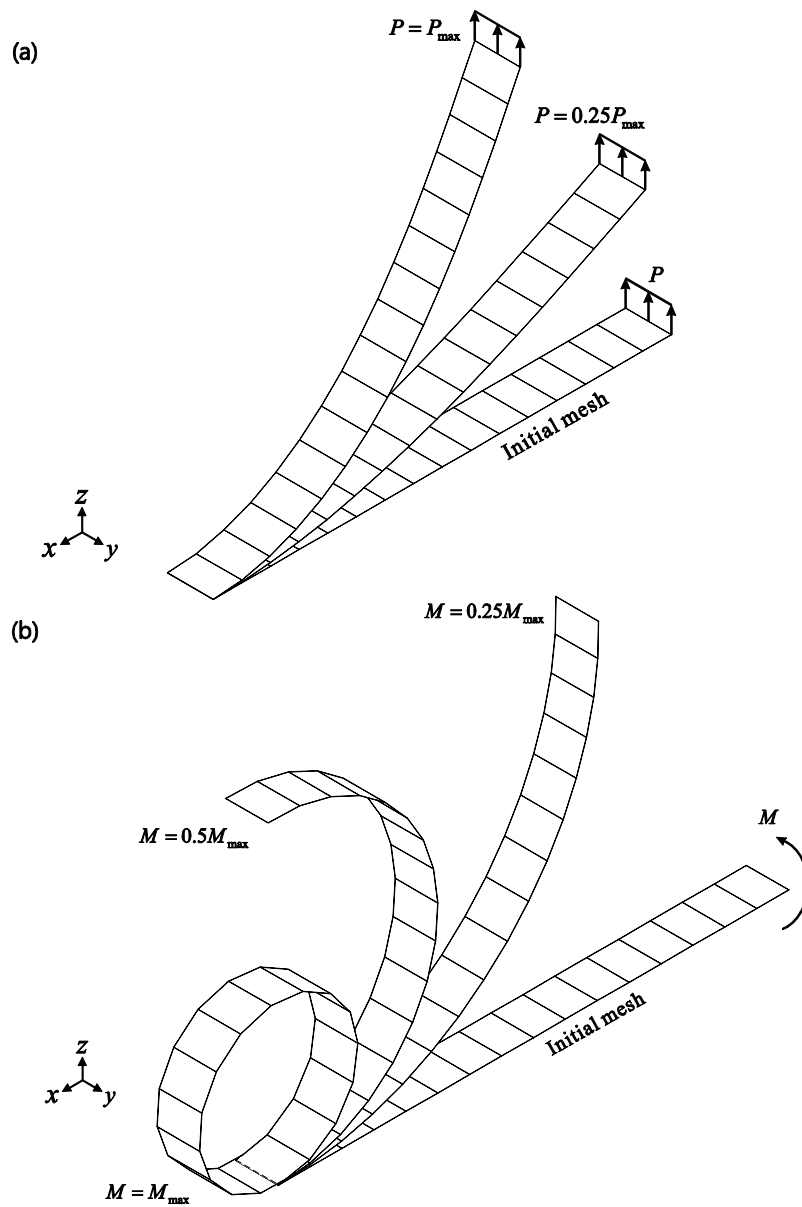


Fig. 2.36. Deformed shapes of the cantilever (a) under tip shearing force and (b) under tip moment.

Fig. 2.35 shows the load-displacement curves of the MITC4 and MITC4+ shell elements. The solutions agree well with the reference and analytic solution in Eq. (2.83). Fig. 2.36 presents the deformed shapes at load levels $P/P_{max} = 0.25$ and 1.0 for shearing load case and $M/M_{max} = 0.25$, 0.5 and 1.0 for moment load case.

2.5.2 Hemispherical shell problem

Hemispherical shell problem [10,14,32,111,115] shown in Fig. 2.37(a) is considered. The spherical

shell with cutout angle $\varphi_0 = 18^\circ$ at its pole is subjected to alternating radial forces P at its equator. The hemisphere has radius $R = 10.0$ and thickness $h = 0.04$. The material properties are $E = 6.825 \times 10^7$ and $\nu = 0.3$. Due to symmetry, only one quarter of the structure corresponding to the shaded region ABCD in Fig. 2.37(a) is modeled, using either 8×8 or 12×12 meshes of the MITC4 and MITC4+ shell elements. We use the following boundary conditions: $u = \beta = 0$ along BC, $v = \beta = 0$ along AD, and $w = 0$ at any single node. Maximum load of $P_{\max} = 400$ is considered.

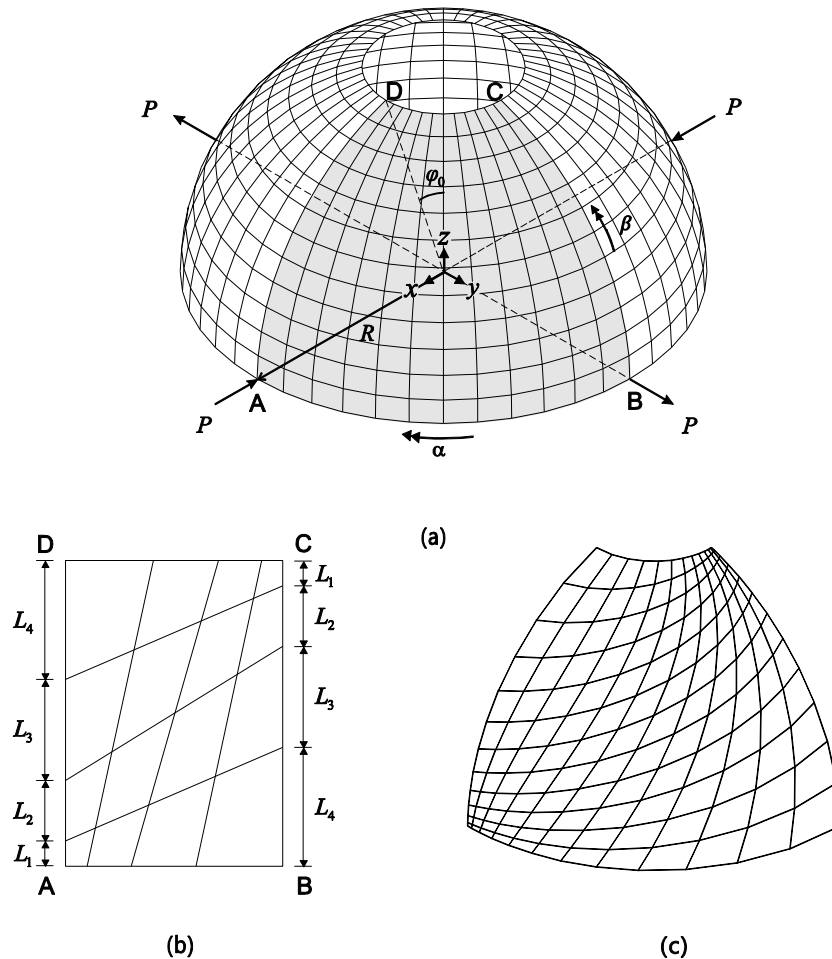


Fig. 2.37. Hemispherical shell problem. (a) Problem description (12×12 uniform mesh). (b) Distorted mesh pattern (4×4 mesh). (c) Distorted mesh pattern applied (12×12 mesh).

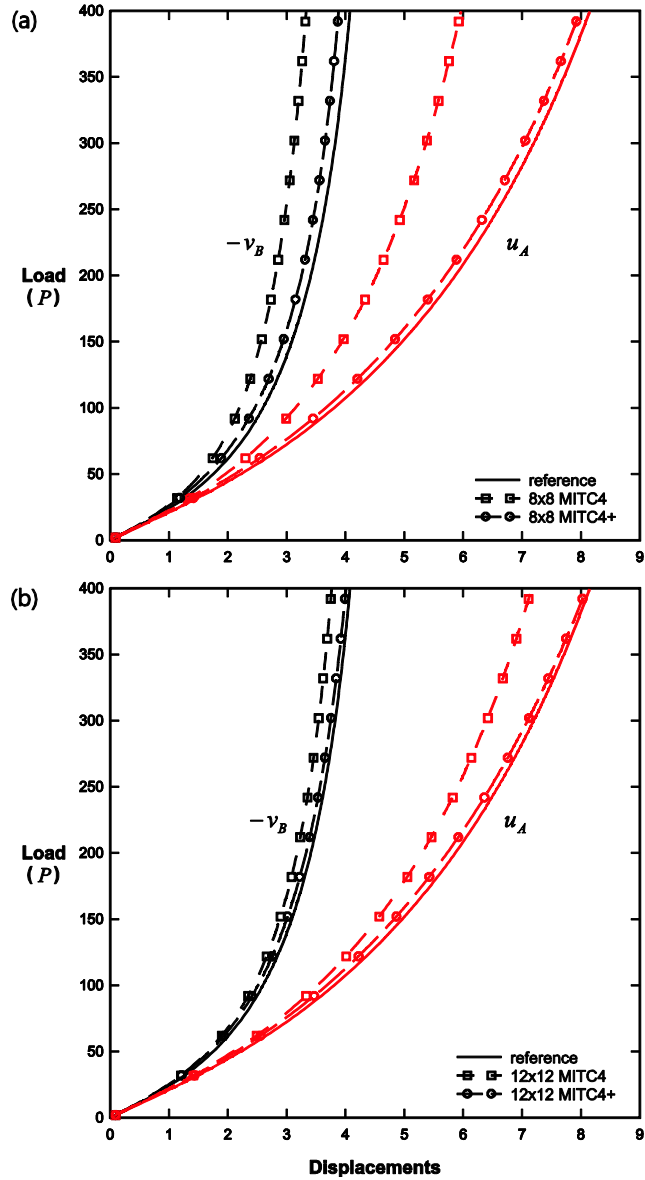


Fig. 2.38. Load-displacement curves for the hemispherical shell problem with the uniform mesh. (a) 8×8 mesh. (b) 12×12 mesh.

In addition to the uniform mesh in Fig. 2.37(a), we consider distorted mesh pattern shown in Fig. 2.37(b). Then, when we use an $N \times N$ element mesh, each edges are discretized in the following ratio: $L_1 : L_2 : L_3 : \dots : L_N = 1 : 2 : 3 : \dots : N$. The applied distorted mesh is shown in Fig. 2.37(c). The reference 32×32 mesh of MITC9 shell elements is employed.

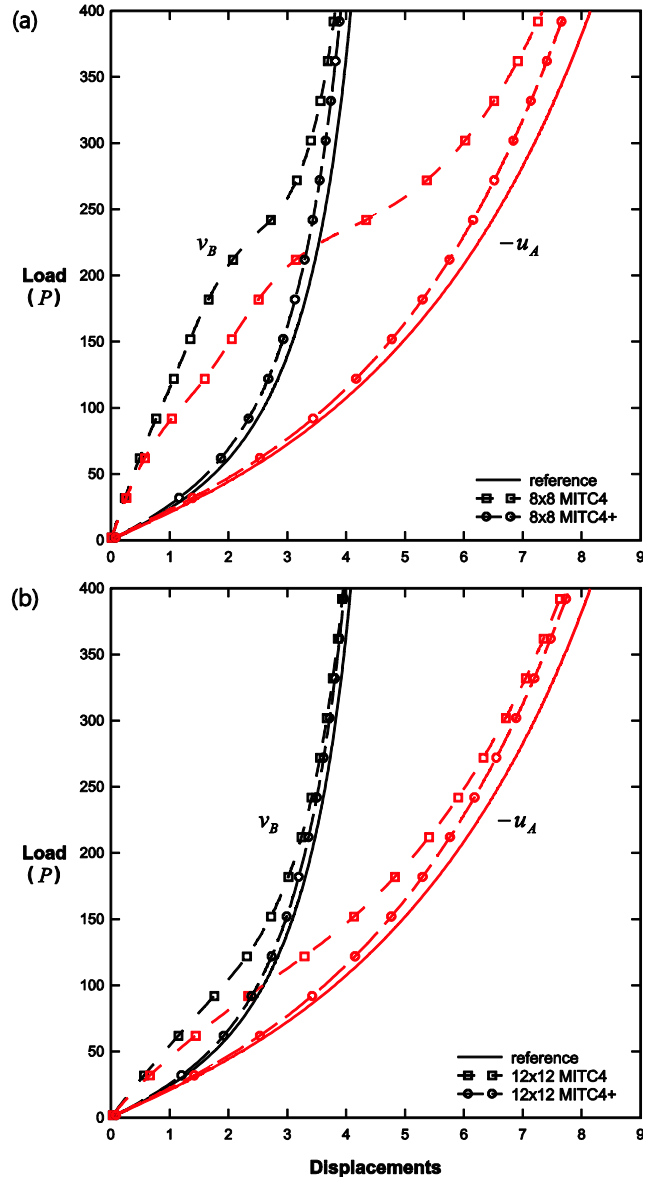


Fig. 2.39. Load-displacement curves for the hemispherical shell problem with the distorted mesh. (a) 8×8 mesh. (b) 12×12 mesh.

Fig. 2.38 and 2.39 present the load-displacement curves for the uniform and distorted mesh, respectively. As the mesh is refined, the solution obtained using the MITC4+ shell element converges quickly than that of the MITC4 shell element. For the distorted mesh cases, the MITC4 shell element behaves erroneously with large deviation from the reference. For the shell element, converging performance is decreased slightly when using distorted mesh with no significant error.

2.5.3 Bending of cylindrical shell structure

Bending problem of cylindrical shell structure [10,13,14,114] shown in Fig. 2.40(a) is considered. The cylindrical shell structure with radius $R = 10.0$, length $L = 20.0$ and angle $\theta = 30^\circ$ is clamped at one side and is subjected to uniform bending moment M the opposite side, which varies with thickness h according to $M = M_0 h^3$. The three thickness to dimension ratio of $h/R = 1/100$, $h/R = 1/1000$ and $h/R = 1/10000$ are tested. The material properties are $E = 2.1 \times 10^6$ and $\nu = 0.0$. For each thickness, we consider load level up to $(M_0)_{\max} = 4.0 \times 10^4$.

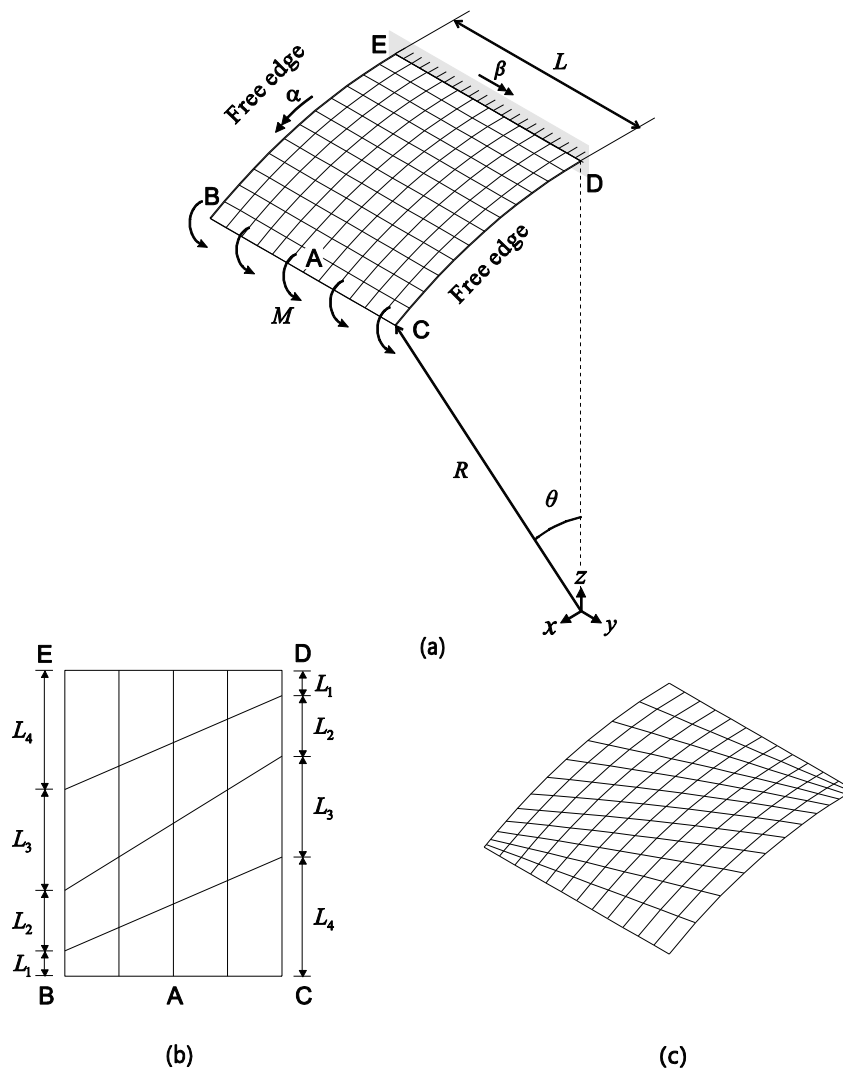


Fig. 2.40. Bending of cylindrical shell structure. (a) Problem description (12×12 uniform mesh). (b) Distorted mesh pattern (4×4 mesh). (c) Distorted mesh pattern applied (12×12 mesh).

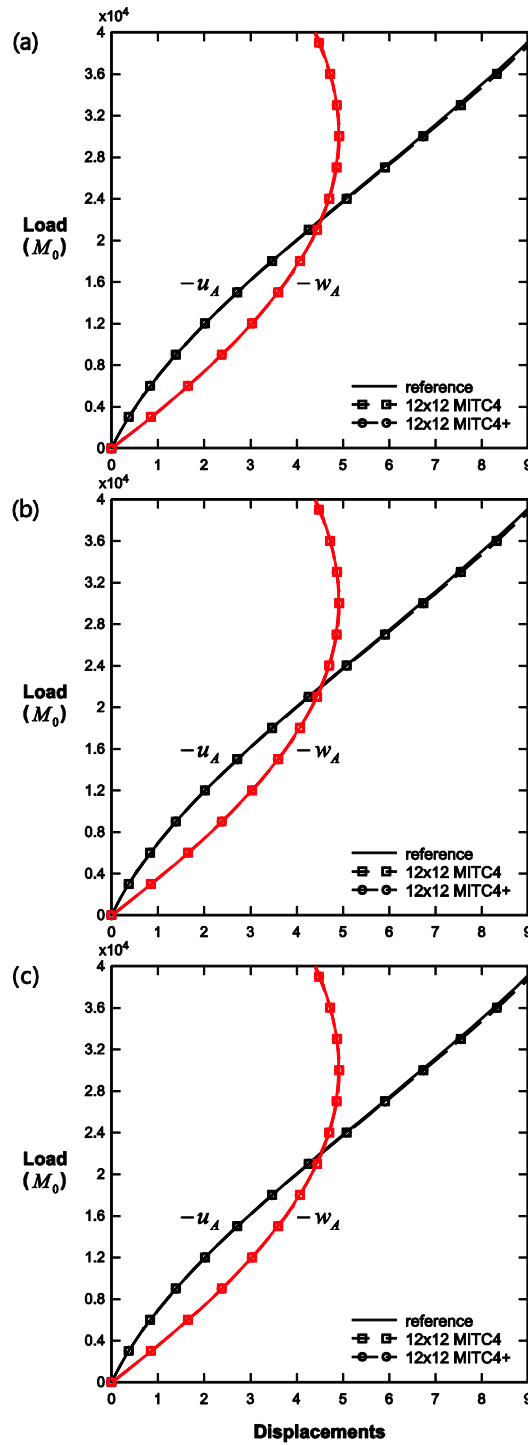


Fig. 2.41. Load-displacement curves for the bending of cylindrical shell structure with the uniform mesh. (a) $h/R = 1/100$. (b) $h/R = 1/1000$. (c) $h/R = 1/10000$.

In addition to the uniform mesh in Fig. 2.40(a), we consider distorted mesh pattern shown in Fig. 2.40(b). Then, when we use an $N \times N$ element mesh, the pair of edges are discretized in the following ratio: $L_1 : L_2 : L_3 : \dots : L_N = 1 : 2 : 3 : \dots : N$. The applied distorted mesh is shown in

Fig. 2.40(c). For the MITC4 and MITC4+ shell elements, 12×12 meshes are used. The reference 32×32 mesh of MITC9 shell elements is employed.

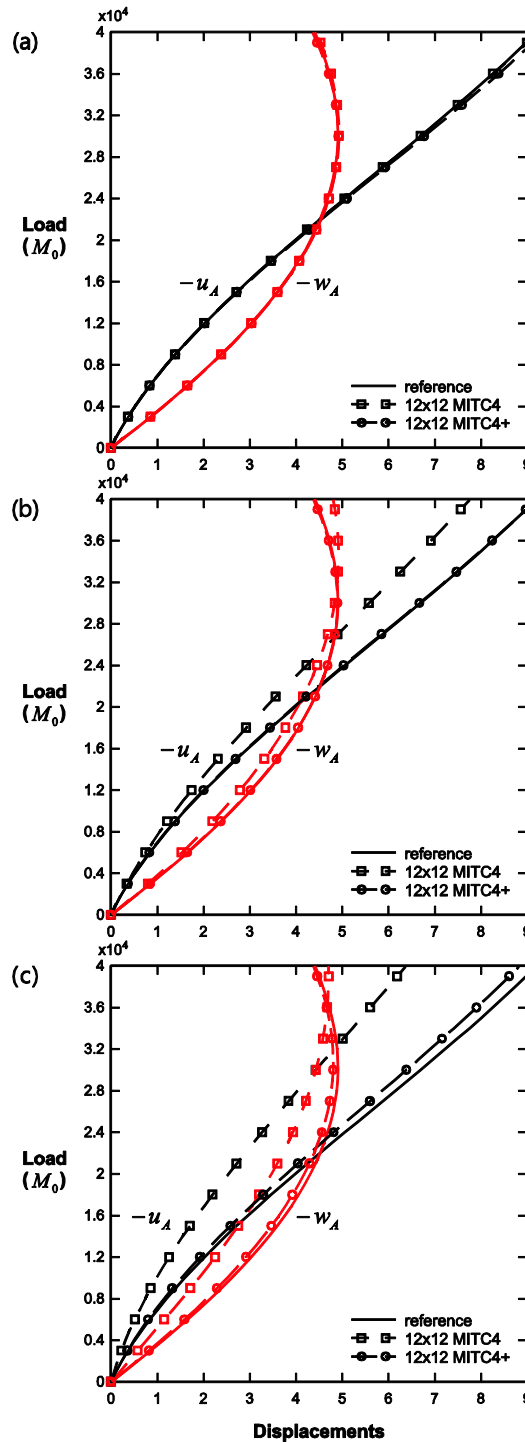


Fig. 2.42. Load-displacement curves for the bending of cylindrical shell structure with the distorted mesh. (a) $h/R = 1/100$. (b) $h/R = 1/1000$. (c) $h/R = 1/10000$.

Fig. 2.41 shows the load-displacement curves for the uniform mesh, where the solutions obtained using the 4-node shell elements agree well with the reference solution. Fig. 2.42 presents the load-displacement curves for the distorted mesh. As thickness is decreased, the solutions obtained by the MITC4 shell element depart largely from the reference due to membrane locking. The MITC4+ shell element still shows good agreement with the reference solution, in which the convergence behavior is close to uniformly optimal as for the uniform mesh case.

2.5.4 Twisted cantilever beam problem

Twisted cantilever beam problem shown in Fig. 2.43 is considered [69,73,111]. The initially twisted beam fully clamped at one end is loaded by point load P at the center of the free tip. The beam has length $L=12.0$ and width $b=1.1$. From the literatures [69,73,111] we test respectively in-plane and out-of-plane load cases for the thin beam structure (thickness $h=0.0032$) to see the effect of membrane locking. In numerical analysis, 4×24 meshes are employed for the MITC4 and MITC4+ shell elements while 8×48 mesh of MITC9 shell elements is used for the reference. The material properties are $E=2.9 \times 10^7$ and $\nu=0.22$. Maximum load level is $P_{\max}=4 \times 10^{-2}$.

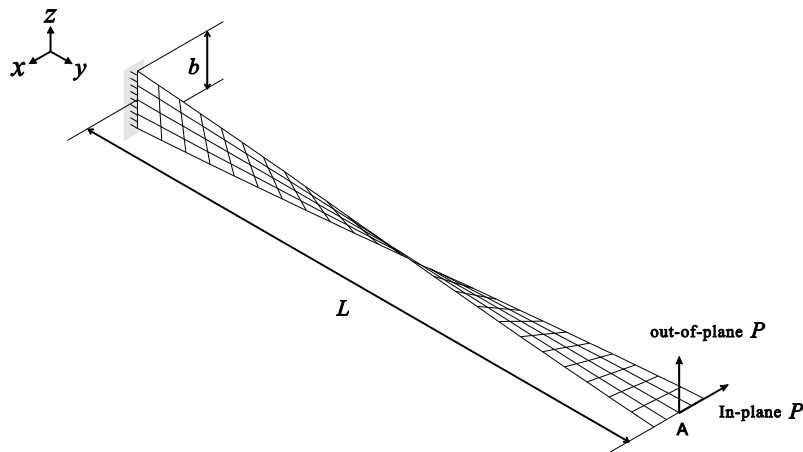


Fig. 2.43. Twisted cantilever beam problem (4×24 mesh).

Fig. 2.44 gives the load-displacement curves for both in-plane and out-of-plane load cases. No severe locking is present for in-plane load case, where both 4-node shell elements perform equally. When the out-of-plane load is applied, the load-displacement curves of the MITC4 shell element digress largely from the reference solution due to membrane locking. Then, the MITC4+ shell element still shows good predictive capability.

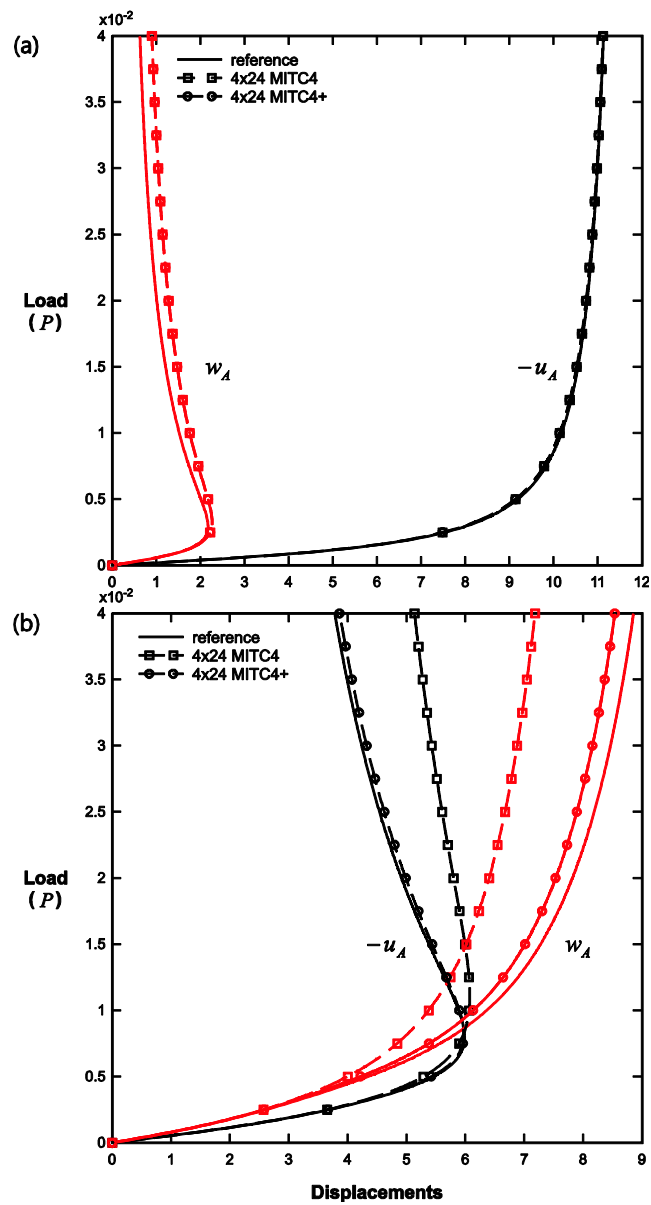


Fig. 2.44. Load-displacement curves for the twisted cantilever beam problem. (a) Case of in-plane load applied. (b) Case of out-of-plane load applied.

2.6 Conclusions

In this study, a set of new 4-node quadrilateral shell elements: the MITC4+, MITC4+N and new MITC4+ elements are developed.

In the MITC4+ shell element, the new assumed strain field was introduced using the membrane

strains obtained from triangular subdomains. The MITC4+ shell element passes the isotropy test, zero energy mode tests, bending and shearing patch tests, and also very closely the membrane patch test. The MITC4+ shell element shows improved convergence behavior in bending-dominated situations without losing the predictive capability of the membrane behavior compared to the MITC4 shell element.

The MITC4+N shell element modifies the formulation of the MITC4+ shell element such that membrane patch test is exactly passed. The element has slightly better membrane-dominated behavior and identical bending-dominated behavior when compared with the MITC4+ shell element.

The new MITC4+ continuum mechanics-based shell element using the MITC approach to alleviate shear and membrane locking. The shear locking is alleviated by using the interpolations of the classical MITC4 element formulation. The membrane locking is alleviated by the use of characteristic geometry and displacement vectors and using a new MITC interpolation on the membrane strains. The new MITC4+ shell element passes all basic tests and shows in an appropriate norm excellent performance in the solution of membrane and bending-dominated problems even when significantly distorted meshes are used. Indeed, in the difficult to solve elliptic and hyperboloid shell analysis problems the element shows an almost ideal behavior.

The new MITC4+ shell element shows a significantly better behavior than the MITC4 shell element for both linear and nonlinear analyses, and is computationally more effective than the previous elements (MITC4+ and MITC4+N). The element is identical to the original MITC4 shell element for a flat geometry and hence the membrane behavior is well preserved.

The limitation in the new MITC4+ shell element is that the value d in Eq. (2.73) could be close to zero if the distortion is severe. Such cases rarely happen in practice and no problem was observed for the numerical examples in this section. However, a mathematical or numerical study of the present formulation to circumvent such limitation would be valuable.

Chapter 3. The new 6-node triangular solid-shell element

3.1 The geometric nonlinear formulation of the developed 6-node triangular solid-shell element, MITC-S6

In this section, the Total Lagrangian nonlinear formulation of newly developed 6-node triangular solid-shell element, the MITC-S6 solid-shell element [117] is presented. In the formulation, the left superscript t and $t + \Delta t$ are used to denote the two consecutive load steps, each of which corresponds to the previously known and the currently unknown configurations in the equilibrium iterations, and the left super- and subscript 0 is used to denote the initial reference configuration. See Fig. 3.1 for the three configurations considered.

The geometry of the proposed element in the configuration t shown in Fig. 3.2 is interpolated by

$${}^t \mathbf{x}(r, s, t) = \frac{1}{2} (1-t) \sum_{i=1}^3 h_i {}^t \mathbf{x}_i^{bot} + \frac{1}{2} (1+t) \sum_{i=1}^3 h_i {}^t \mathbf{x}_i^{top}, \quad (3.1)$$

where $h_1 = r$, $h_2 = s$, $h_3 = 1 - r - s$ and the superscripts “bot” and “top” respectively denotes the bottom and top surfaces of the solid-shell element.

The incremental displacement vector \mathbf{u} from the configuration t to the configuration $t + \Delta t$ is

$$\mathbf{u}(r, s, t) = {}^{t+\Delta t} \mathbf{x}(r, s, t) - {}^t \mathbf{x}(r, s, t), \quad (3.2)$$

and hence

$$\mathbf{u} = \frac{1}{2} (1-t) \sum_{i=1}^3 h_i \mathbf{u}_i^{bot} + \frac{1}{2} (1+t) \sum_{i=1}^3 h_i \mathbf{u}_i^{top}. \quad (3.3)$$

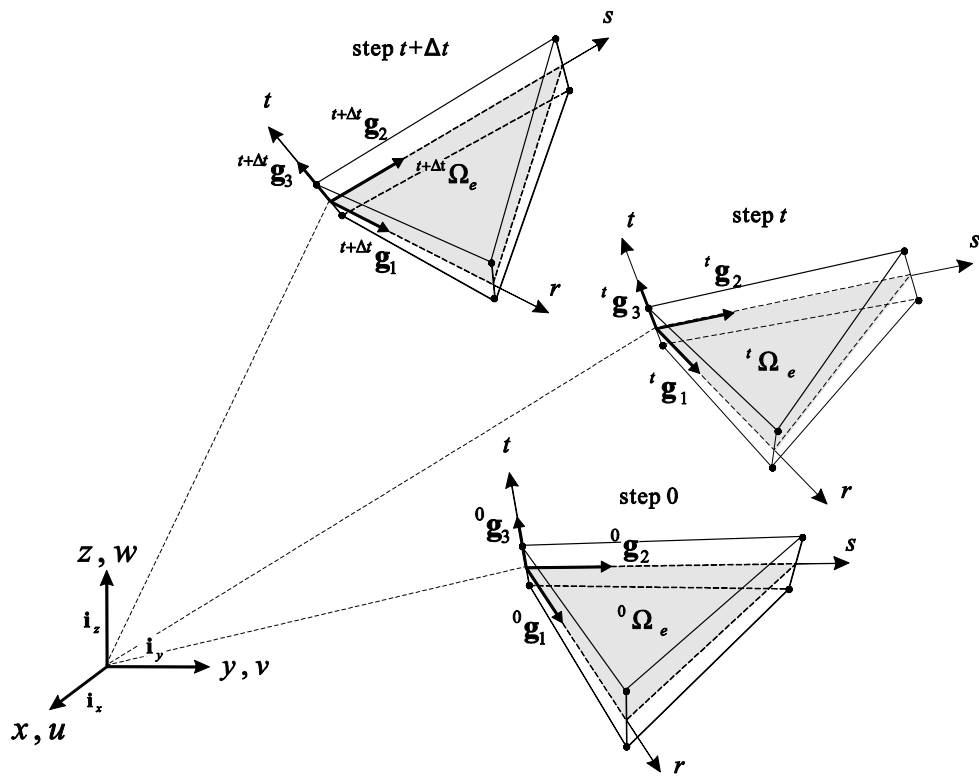


Fig. 3.1. Nonlinear kinematics of the 6-node triangular solid-shell element. The covariant base vectors at $r = s = t = 0$ in the initial (0), previous (t) and current ($t + \Delta t$) configurations are depicted.

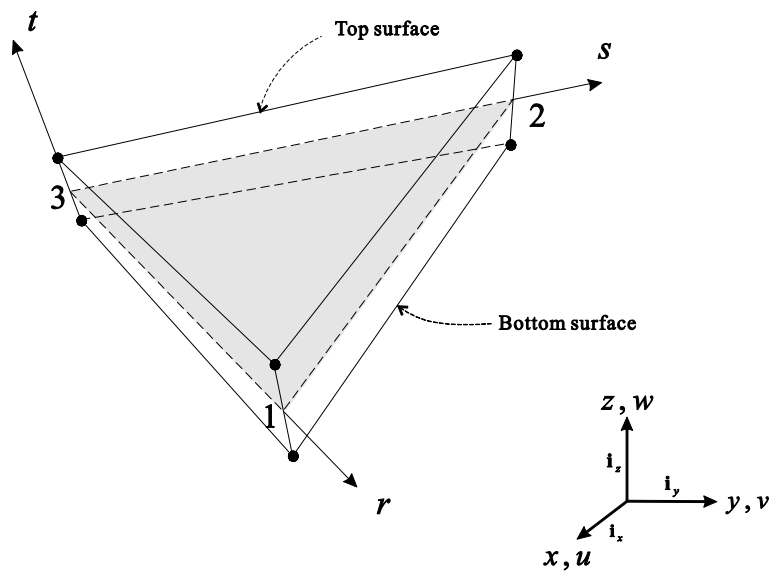


Fig. 3.2. A 6-node triangular solid-shell element.

The covariant components of the Green-Lagrange strain are given by

$${}^t_0\varepsilon_{ij} = \frac{1}{2}({}^t\mathbf{g}_i \cdot {}^t\mathbf{g}_j - {}^0\mathbf{g}_i \cdot {}^0\mathbf{g}_j) \quad \text{with} \quad {}^0\mathbf{g}_i = \frac{\partial {}^0\mathbf{x}}{\partial r_i}, \quad {}^t\mathbf{g}_i = \frac{\partial {}^t\mathbf{x}}{\partial r_i} = {}^0\mathbf{g}_i + \mathbf{u}_{,i}, \quad (3.4)$$

where $\mathbf{u}_{,i} = \frac{\partial \mathbf{u}}{\partial r_i}$, $\mathbf{u} = {}^t\mathbf{x} - {}^0\mathbf{x}$, $r_1 = r$, $r_2 = s$, $r_3 = t$.

The incremental covariant strain components are

$${}_0\varepsilon_{ij} = {}^{t+\Delta t}{}_0\varepsilon_{ij} - {}^t{}_0\varepsilon_{ij} = \frac{1}{2}(\mathbf{u}_{,i} \cdot {}^t\mathbf{g}_j + {}^t\mathbf{g}_i \cdot \mathbf{u}_{,j} + \mathbf{u}_{,i} \cdot \mathbf{u}_{,j}) \quad \text{with} \quad \mathbf{u}_{,i} = \frac{\partial \mathbf{u}}{\partial r_i}. \quad (3.5)$$

which can be decomposed as

$${}_0\varepsilon_{ij} = {}_0e_{ij} + {}_0\eta_{ij} \quad \text{with} \quad {}_0e_{ij} = \frac{1}{2}(\mathbf{u}_{,i} \cdot {}^t\mathbf{g}_j + {}^t\mathbf{g}_i \cdot \mathbf{u}_{,j}), \quad {}_0\eta_{ij} = \frac{1}{2}(\mathbf{u}_{,i} \cdot \mathbf{u}_{,j}), \quad (3.6)$$

where ${}_0e_{ij}$ and ${}_0\eta_{ij}$ are the linear and nonlinear parts, respectively.

Substituting Eq. (3.3) into Eq. (3.6), the linear and nonlinear parts of the covariant in-plane strains are directly calculated as follows:

$${}_0e_{ij} = \frac{1}{2}(\mathbf{u}_{,i} \cdot {}^t\mathbf{g}_j + {}^t\mathbf{g}_i \cdot \mathbf{u}_{,j}) = \mathbf{B}_{ij} \mathbf{U}_e, \quad {}_0\eta_{ij} = \frac{1}{2}(\mathbf{u}_{,i} \cdot \mathbf{u}_{,j}) = \frac{1}{2} \mathbf{U}_e^T \mathbf{N}_{ij} \mathbf{U}_e \quad \text{for } i, j = 1, 2, \quad (3.7)$$

in which \mathbf{B}_{ij} is the linear strain-displacement relation matrix for the strain component ij , \mathbf{U}_e is the incremental nodal displacement vector including \mathbf{u}_i^{bot} and \mathbf{u}_i^{top} , and \mathbf{N}_{ij} is the matrix representing the relation between the nonlinear strain components and the nodal displacements.

For the transverse shear strains and the corresponding variations, the assumed strain field of the MITC3+ triangular shell element [7] is employed. The linear parts of the covariant transverse shear strains ${}_0e_{23}$ and ${}_0e_{13}$ are substituted by

$${}_0\tilde{e}_{23} = \frac{2}{3}({}_0e_{23}^{(A)} - \frac{1}{2}{}_0e_{13}^{(A)}) + \frac{1}{3}({}_0e_{13}^{(C)} + {}_0e_{23}^{(C)}) + \frac{1}{3}\tilde{c}(1-3r) = \mathbf{B}_{23} \mathbf{U}_e, \quad (3.8a)$$

$${}_0\tilde{e}_{13} = \frac{2}{3}({}_0e_{13}^{(B)} - \frac{1}{2}{}_0e_{23}^{(B)}) + \frac{1}{3}({}_0e_{13}^{(C)} + {}_0e_{23}^{(C)}) + \frac{1}{3}\tilde{c}(3s-1) = \mathbf{B}_{23} \mathbf{U}_e, \quad (3.8b)$$

with

$$\tilde{c} = {}_0e_{13}^{(F)} - {}_0e_{13}^{(D)} - {}_0e_{23}^{(F)} + {}_0e_{23}^{(E)}, \quad (3.8c)$$

in which the tying points are shown in Fig. 3.3. As for the MITC3+ shell element [7], the fixed val-

ue $d = 1/100,000$ is chosen. The same assumed strain field with the same tying positions is used for the nonlinear part of the covariant transverse shear strains:

$${}_0\tilde{\eta}_{i3} = \frac{1}{2}\mathbf{U}_e^T \mathbf{N}_{i3} \mathbf{U}_e \quad \text{for } i=1,2. \quad (3.9)$$

To reduce curvature thickness locking, the assumed strain method is also used. The linear and non-linear parts of the thickness strain are assumed as

$${}_0\tilde{e}_{33}(r,s) = \frac{1}{3}({}_0e_{33}(0,0)+{}_0e_{33}(1,0)+{}_0e_{33}(0,1)) = \mathbf{B}_{33}\mathbf{U}_e, \quad (3.10a)$$

$${}_0\tilde{\eta}_{33}(r,s) = \frac{1}{3}({}_0\eta_{33}(0,0)+{}_0\eta_{33}(1,0)+{}_0\eta_{33}(0,1)) = \frac{1}{2}\mathbf{U}_e^T \mathbf{N}_{33} \mathbf{U}_e. \quad (3.10b)$$

Note that, unlike the linear strain field in Ref. [30], the constant assumed strain field is employed for thickness strain in this element.

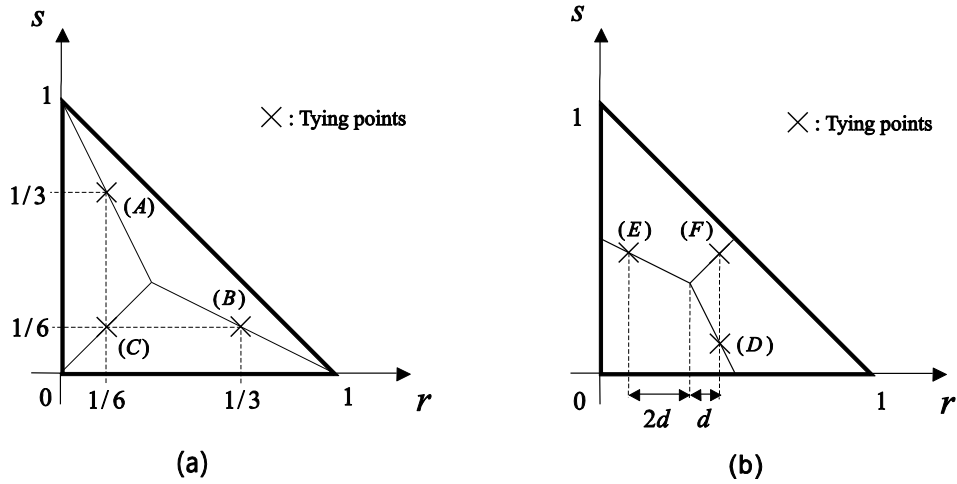


Fig. 3.3. Tying positions for the transverse shear strains of the MITC-S6 solid-shell element.

Here, the enhanced strains to improve the behaviors of the 6-node triangular solid-shell element are derived. The enhanced strains are used for the linear part of the covariant in-plane, transverse shear and thickness strains.

In order to construct the enhanced strains, the following interpolations defined using the bubble-type functions are considered:

$$\mathbf{u}^{\text{in-plane}} = \frac{1}{2}h_b t(\alpha \mathbf{V}_1 + \beta \mathbf{V}_2), \quad (3.11a)$$

$$\mathbf{u}^{\text{thickness}} = -\frac{1}{2}h_q\gamma\mathbf{V}_3, \quad (3.11b)$$

where $h_b = 27rs(1-r-s)$ and $h_q = 1-t^2$ are the two-dimensional bubble and one-dimensional quadratic functions, \mathbf{V}_1 , \mathbf{V}_2 and \mathbf{V}_3 are vectors denoting the direction of translations, and α , β and γ are internal variables.

The interpolation in Eq. (3.11a) is used to effectively enhance the bending mechanism of the triangular elements, see Refs. [7,39,61,62]. In the plate and shell elements [7,62], the variables α and β are defined as rotations about \mathbf{V}_1 and \mathbf{V}_2 . However, in this 6-node solid-shell element, the variables α and β represent the in-plane translation of shell surfaces in the directions of \mathbf{V}_1 and \mathbf{V}_2 . As long as the two vectors can fully define the in-plane translations, i.e. they are not coincident to each other, the same numerical results are obtained. Thus, it is not necessary to update \mathbf{V}_1 and \mathbf{V}_2 in the nonlinear solution procedure. In this study, $\mathbf{V}_1 = \mathbf{i}_x$ and $\mathbf{V}_2 = \mathbf{i}_y$ is chosen.

The interpolation in Eq. (3.11b) has been used in three-dimensional shell elements [35,76,93] to induce the thickness stretch to vary linearly along the thickness direction, which is useful to avoid Poisson thickness locking. For this purpose, the vector \mathbf{V}_3 is taken to be identical to the third contravariant base vector $\mathbf{V}_3 = {}^t\mathbf{g}^3$, where the contravariant base vectors ${}^t\mathbf{g}^i$ satisfy the relation ${}^t\mathbf{g}_i \cdot {}^t\mathbf{g}^j = \delta_{ij}$ for the Kronecker delta δ_{ij} .

Using the bubble interpolation in Eq. (3.11a), the following enhanced in-plane covariant strain is obtained:

$${}_0e_{ij}^{enh} = \frac{1}{2}(\mathbf{u}_{,i}^{\text{in-plane}} \cdot {}^t\mathbf{g}_j + {}^t\mathbf{g}_i \cdot \mathbf{u}_{,j}^{\text{in-plane}}) = \mathbf{G}_{ij}\Lambda_e \quad \text{for } i, j = 1, 2, \quad (3.12)$$

where $\mathbf{u}_{,i}^{\text{in-plane}} = \frac{\partial \mathbf{u}^{\text{in-plane}}}{\partial r_i}$, \mathbf{G}_{ij} is the enhanced strain-displacement relation matrix, and Λ_e is

the vector of internal variables. This strain field is also effective for improving the bending performance of the 6-node triangular solid-shell element.

The transverse shear covariant strains due to the bubble interpolation in Eq. (3.11a) are calculated by

$${}_0e_{i3}^{bub} = \frac{1}{2}(\mathbf{u}_{,i}^{\text{in-plane},t} \cdot \mathbf{g}_3 + {}^t\mathbf{g}_i \cdot \mathbf{u}_{,3}^{\text{in-plane}}), \quad (3.13)$$

and the enhanced transverse shear strains are obtained using the following assumed field:

$${}_0e_{23}^{enh} = \frac{2}{3}({}_0e_{23}^{bub(A)} - \frac{1}{2}{}_0e_{13}^{bub(A)}) + \frac{1}{3}({}_0e_{13}^{bub(C)} + {}_0e_{23}^{bub(C)}) = \mathbf{G}_{23}\mathbf{\Lambda}_e, \quad (3.14a)$$

$${}_0e_{13}^{enh} = \frac{2}{3}({}_0e_{13}^{bub(B)} - \frac{1}{2}{}_0e_{23}^{bub(B)}) + \frac{1}{3}({}_0e_{13}^{bub(C)} + {}_0e_{23}^{bub(C)}) = \mathbf{G}_{13}\mathbf{\Lambda}_e, \quad (3.14b)$$

where the tying points (A , B and C) used are shown in Fig. 3.3. Note that this assumed strain does not include the terms linear in r and s from Eq. (3.8), resulting in simple matrices \mathbf{G}_{23} and \mathbf{G}_{13} as will be presented.

In order to alleviate Poisson thickness locking, the following enhanced strain is employed for the thickness normal component:

$${}_0e_{33}^{enh} = {}^t\mathbf{g}_3 \cdot \mathbf{u}_{,3}^{\text{thickness}} = \gamma t = \mathbf{G}_{33}\mathbf{\Lambda}_e, \quad (3.15)$$

where $\mathbf{u}_{,3}^{\text{thickness}} = \frac{\partial \mathbf{u}^{\text{thickness}}}{\partial r_3}$. In Eq. (3.15), a single internal variable was used, as in Ref. [31], with

the physical meaning of thickness normal translation being quadratic in t .

Note that the interpolation in Eq. (3.11a) is used only to enhance strain components ‘11’, ‘22’, ‘12’, ‘23’ and ‘13’, while the thickness strain (component ‘33’) is enhanced by Eq. (3.11b). That is, two strain enhancements are independently applied to each other. This is an important characteristic for the present 6-node solid-shell element to behave well in various shell problems.

Finally, the linear part of the incremental covariant strains for the 6-node MITC solid-shell element is obtained:

$${}_0\bar{e}_{ij} = {}_0e_{ij} + {}_0e_{ij}^{enh} = \mathbf{B}_{ij}\mathbf{U}_e + \mathbf{G}_{ij}\mathbf{\Lambda}_e \quad \text{for } i, j = 1, 2, \quad (3.16a)$$

$${}_0\bar{e}_{i3} = {}_0\tilde{e}_{i3} + {}_0e_{i3}^{enh} = \mathbf{B}_{i3}\mathbf{U}_e + \mathbf{G}_{i3}\mathbf{\Lambda}_e \quad \text{for } i = 1, 2, \quad (3.16b)$$

$${}_0\bar{e}_{33} = {}_0\tilde{e}_{33} + {}_0e_{33}^{enh} = \mathbf{B}_{33}\mathbf{U}_e + \mathbf{G}_{33}\mathbf{\Lambda}_e, \quad (3.16c)$$

where $\mathbf{\Lambda}_e = [\alpha \quad \beta \quad \gamma]^T$ is the vector of internal variables for the element. Finally, the resulting form of the enhanced strain matrices (\mathbf{G}_{ij}) is given as follows.

$$[\mathbf{G}_{11} \quad \mathbf{G}_{22} \quad \mathbf{G}_{33} \quad \mathbf{G}_{12} \quad \mathbf{G}_{23} \quad \mathbf{G}_{13}]^T$$

$$= \begin{bmatrix} h_{b,1} {}^t \mathbf{V}_1 \cdot {}^t \mathbf{g}_1 & h_{b,2} {}^t \mathbf{V}_1 \cdot {}^t \mathbf{g}_2 & 0 & \frac{1}{2} h_{b,2} {}^t \mathbf{V}_1 \cdot {}^t \mathbf{g}_1 + \frac{1}{2} h_{b,1} {}^t \mathbf{V}_1 \cdot {}^t \mathbf{g}_2 & \frac{1}{4} {}^t \mathbf{V}_1 \cdot {}^t \mathbf{g}_2 & \frac{1}{4} {}^t \mathbf{V}_1 \cdot {}^t \mathbf{g}_1 \\ h_{b,1} {}^t \mathbf{V}_2 \cdot {}^t \mathbf{g}_1 & h_{b,2} {}^t \mathbf{V}_2 \cdot {}^t \mathbf{g}_2 & 0 & \frac{1}{2} h_{b,2} {}^t \mathbf{V}_2 \cdot {}^t \mathbf{g}_1 + \frac{1}{2} h_{b,1} {}^t \mathbf{V}_2 \cdot {}^t \mathbf{g}_2 & \frac{1}{4} {}^t \mathbf{V}_2 \cdot {}^t \mathbf{g}_2 & \frac{1}{4} {}^t \mathbf{V}_2 \cdot {}^t \mathbf{g}_1 \\ 0 & 0 & t & 0 & 0 & 0 \end{bmatrix}^T, \quad (3.17)$$

in which $h_{b,i} = \frac{\partial h_b}{\partial r_i}$ for $i = 1, 2$.

Linearizing the principle of virtual work in the configuration $t + \Delta t$ about the known configuration at t , the following total Lagrangian formulation is given [15].

$$\int_{0V} {}_0 C^{ijkl} {}_0 \bar{e}_{ij} \delta_0 \bar{e}_{kl} d^0 V + \int_{0V} {}^t S^{ij} \delta_0 \bar{\eta}_{ij} d^0 V = {}^{t+\Delta t} \mathfrak{R} - \int_{0V} {}^t \bar{S}^{ij} \delta_0 \bar{e}_{ij} d^0 V, \quad (3.18)$$

where ${}^0 V$ is the volume of the solid-shell element at step 0, ${}^{t+\Delta t} \mathfrak{R}$ is the external virtual work due to the applied surface tractions and body forces, ${}^t S^{ij}$ denotes the contravariant second Piola-Kirchhoff stress and ${}_0 C^{ijkl}$ is the corresponding general 3D material law tensor [35,93,100].

Substituting Eqs. (3.7)-(3.10) and (3.16) into Eq. (3.18), the Total Lagrangian formulation is discretized as follows:

$$\begin{aligned} & \delta \mathbf{U}_e^T \left[\int_{0V} \mathbf{B}_{ij}^T {}_0 C^{ijkl} \mathbf{B}_{kl} d^0 V + \int_{0V} \mathbf{N}_{ij} {}^t S^{ij} d^0 V \right] \mathbf{U}_e + \delta \mathbf{U}_e^T \left[\int_{0V} \mathbf{B}_{ij}^T {}_0 C^{ijkl} \mathbf{G}_{kl} d^0 V \right] \mathbf{A}_e \\ & + \delta \mathbf{A}_e^T \left[\int_{0V} \mathbf{G}_{ij}^T {}_0 C^{ijkl} \mathbf{B}_{kl} d^0 V \right] \mathbf{U}_e + \delta \mathbf{A}_e^T \left[\int_{0V} \mathbf{G}_{ij}^T {}_0 C^{ijkl} \mathbf{G}_{kl} d^0 V \right] \mathbf{A}_e \\ & = \delta \mathbf{U}_e^T {}^{t+\Delta t} \mathbf{R}_e - \delta \mathbf{U}_e^T \int_{0V} \mathbf{B}_{ij}^T {}^t S^{ij} d^0 V - \delta \mathbf{A}_e^T \int_{0V} \mathbf{G}_{ij}^T {}^t S^{ij} d^0 V, \end{aligned} \quad (3.19)$$

where ${}^{t+\Delta t} \mathbf{R}_e$ is the external load vector at step $t + \Delta t$.

The following linearized equilibrium equation is obtained in the element level:

$$\begin{bmatrix} {}^t \hat{\mathbf{K}}_e & {}^t \mathbf{\Gamma}_e \\ {}^t \mathbf{\Gamma}_e^T & {}^t \mathbf{A}_e \end{bmatrix} \begin{bmatrix} \mathbf{U}_e \\ \mathbf{A}_e \end{bmatrix} = \begin{bmatrix} {}^{t+\Delta t} \mathbf{R}_e \\ \mathbf{0} \end{bmatrix} - \begin{bmatrix} {}^t \hat{\mathbf{F}}_e \\ {}^t \mathbf{H}_e \end{bmatrix}, \quad (3.20)$$

with

$${}^t \hat{\mathbf{K}}_e = \int_{0V} \mathbf{B}_{ij}^T {}_0 C^{ijkl} \mathbf{B}_{kl} d^0 V + \int_{0V} \mathbf{N}_{ij} {}^t S^{ij} d^0 V, \quad {}^t \mathbf{\Gamma}_e = \int_{0V} \mathbf{B}_{ij}^T {}_0 C^{ijkl} \mathbf{G}_{kl} d^0 V,$$

$${}^t \mathbf{A}_e = \int_{0V} \mathbf{G}_{ij}^T {}_0 C^{ijkl} \mathbf{G}_{kl} d^0 V, \quad {}^t \hat{\mathbf{F}}_e = \int_{0V} \mathbf{B}_{ij}^T {}^t S^{ij} d^0 V, \quad {}^t \mathbf{H}_e = \int_{0V} \mathbf{G}_{ij}^T {}^t S^{ij} d^0 V.$$

The internal variables related to the strain enhancements can be easily condensed out in the element level to obtain the condensed equilibrium equation [32,33,35,39]

$${}^t\mathbf{K}_e\mathbf{U}_e = {}^{t+\Delta t}\mathbf{R}_e - {}^t\mathbf{F}_e \quad \text{with} \quad {}^t\mathbf{K}_e = {}^t\hat{\mathbf{K}}_e - {}^t\Gamma_e {}^t\mathbf{A}_e^{-1} {}^t\Gamma_e^T, \quad {}^t\mathbf{F}_e = {}^t\hat{\mathbf{F}}_e - {}^t\Gamma_e {}^t\mathbf{A}_e^{-1} {}^t\mathbf{H}_e \quad (3.21)$$

where the contravariant second Piola-Kirchhoff stress is updated by

$${}^{t+\Delta t}{}_0\mathbf{S}^{ij} = {}^t{}_0\mathbf{S}^{ij} + {}_0\mathbf{S}^{ij} \quad (3.22)$$

with

$${}_0\mathbf{S}^{ij} = {}_0\mathbf{C}^{ijkl} (\mathbf{B}_{kl}\mathbf{U}_e + \mathbf{G}_{kl}\Lambda_e + \frac{1}{2}\mathbf{U}_e^T \mathbf{N}_{kl}\mathbf{U}_e), \quad (3.23)$$

$$\Lambda_e = -{}^t\mathbf{A}_e^{-1} ({}^t\mathbf{H}_e + {}^t\Gamma_e^T \mathbf{U}_e). \quad (3.24)$$

In the incremental solution procedure, the geometry is updated using Eq. (3.2). For the evaluation of the element stiffness matrix and internal nodal force vector, 3-point Gauss integration in the r - s plane and the 2-point Gauss integration in the t -direction are employed.

3.2 The previous 8-node quadrilateral solid-shell element, MITC-S8

In this section, the formulation of the 8-node solid-shell element in the literatures [32-36,41] are presented. The element is denoted as MITC-S8 that is used for comparison in this study. Shear locking and thickness locking are treated using the assumed strain and EAS methods.

For the 8-node solid-shell element, the geometry and displacement interpolations are given by (Fig. 3.4)

$$\hat{\mathbf{x}}(r, s, t) = \frac{1}{2}(1-t)\sum_{i=1}^4 \hat{h}_i \hat{\mathbf{x}}_i^{bot} + \frac{1}{2}(1+t)\sum_{i=1}^4 \hat{h}_i \hat{\mathbf{x}}_i^{top}, \quad (3.25)$$

$$\hat{\mathbf{u}}(r, s, t) = \frac{1}{2}(1-t)\sum_{i=1}^4 \hat{h}_i \hat{\mathbf{u}}_i^{bot} + \frac{1}{2}(1+t)\sum_{i=1}^4 \hat{h}_i \hat{\mathbf{u}}_i^{top}. \quad (3.26)$$

$$\text{with } \hat{h}_1 = \frac{1}{4}(1-r)(1-s), \quad \hat{h}_2 = \frac{1}{4}(1+r)(1-s), \quad \hat{h}_3 = \frac{1}{4}(1+r)(1+s), \quad \hat{h}_4 = \frac{1}{4}(1-r)(1+s).$$

The linear part of the covariant strain is calculated by

$$\tilde{e}_{ij}(r, s, t) = \frac{1}{2}(\hat{\mathbf{u}}_{,i} \cdot \hat{\mathbf{g}}_j + \hat{\mathbf{g}}_i \cdot \hat{\mathbf{u}}_{,j}) \quad (3.27)$$

$$\text{with } \hat{\mathbf{u}}_{,i} = \frac{\partial \hat{\mathbf{u}}}{\partial r_i}, \quad \hat{\mathbf{g}}_i = \frac{\partial \hat{\mathbf{x}}}{\partial r_i}, \quad r_1 = r, \quad r_2 = s, \quad r_3 = \xi. \quad (3.28)$$

The following assumed transverse shear strains are employed to treat shear locking, see Refs. [32-36,41]

$$\tilde{e}_{23}(r, s, t) = \frac{1}{2}(1+r)\tilde{e}_{23}^{(C)} + \frac{1}{2}(1-r)\tilde{e}_{23}^{(D)}, \quad (3.29)$$

$$\tilde{e}_{13}(r, s, t) = \frac{1}{2}(1+s)\tilde{e}_{13}^{(A)} + \frac{1}{2}(1-s)\tilde{e}_{13}^{(B)}, \quad (3.30)$$

where the tying points are shown in Fig. 2.2.

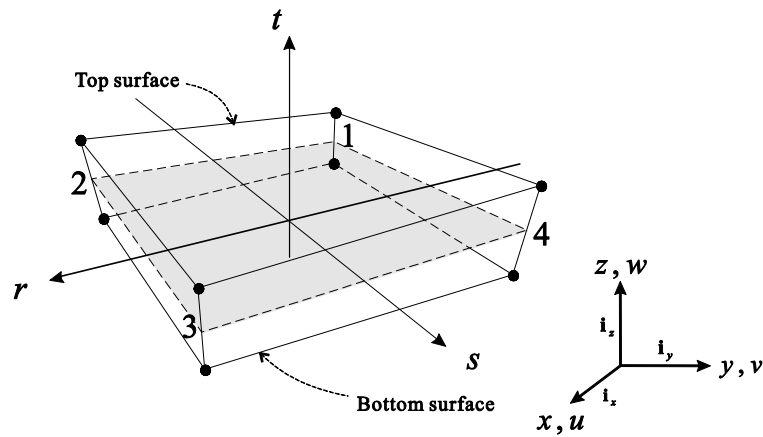


Fig. 3.4. An 8-node quadrilateral solid-shell element.

In order to reduce thickness locking, the following assumed strains is used for thickness strain, see Refs. [32-35,41,76],

$$\tilde{e}_{33}(r, s, t) = \hat{h}_1 \tilde{e}_{33}(-1,-1) + \hat{h}_2 \tilde{e}_{33}(1,-1) + \hat{h}_3 \tilde{e}_{33}(1,1) + \hat{h}_4 \tilde{e}_{33}(-1,1). \quad (3.31)$$

The enhanced assumed thickness strain is also used as follows:

$$e_{33}^{enh}(r, s, t) = \frac{j_0}{j} t_{33}^2 [t \quad rt \quad st \quad rst] \begin{bmatrix} \gamma_1 \\ \gamma_2 \\ \gamma_3 \\ \gamma_4 \end{bmatrix}, \quad (3.32)$$

$$\text{with } t_{33} = \widehat{\mathbf{g}}_3(r,s,t) \cdot \widehat{\mathbf{g}}^3(0,0,0), \quad \widehat{\mathbf{g}}_i(r,s,t) \cdot \widehat{\mathbf{g}}^j(r,s,t) = \delta_{ij}, \quad (3.33)$$

in which j and j_0 are the determinants of the Jacobian matrix $[\widehat{\mathbf{g}}_1 \quad \widehat{\mathbf{g}}_2 \quad \widehat{\mathbf{g}}_3]^T$ at (r,s,t) and at $(0,0,0)$, respectively, and γ_i are internal variables, see Refs. [32,33,41]. Note that, unlike the MITC-S6 triangular solid-shell element, four internal variables are necessary to satisfy the basic tests.

Note that this element is equivalent to the 8-node solid-shell element proposed by Klinkel et al. [32,33]. In the numerical examples, the $2 \times 2 \times 2$ Gauss integration is employed.

3.3 Basic tests

In this section, basic numerical tests are conducted for the proposed solid-shell element. The isotropy, patch and zero energy mode tests are considered.

Spatially isotropic behavior is an important requirement for the triangular elements. The element behavior should not depend on the sequence of node numbering, i.e. the element orientation [3,5-9,38]. The proposed solid-shell element passes this test.

Three patch tests of the membrane, bending and transverse shearing patch tests are performed, see Refs. [1,5-9,14,19,30-34,36-40,101,102]. The geometry of the mesh is shown in Fig. 3.5(a). The loading and boundary conditions for the membrane, bending and transverse shearing patch tests are shown in Fig. 3.5(b) to 3.5(d), respectively, in which the boundary conditions for the shaded regions are specified. The patch of elements is additionally subjected to the minimum number of constraints to prevent rigid body motions. If the correct constant stress fields are calculated, the patch tests are passed. The proposed element passes all the patch tests. Also, the element expresses constant normal stress in the constant compression test [30] performed using a single element, see Fig. 3.6.

In the zero energy mode tests, the number of zero eigenvalues of the stiffness matrix of a single unsupported element is counted [1,5-9,14,19,31,35,38-40]. For the present element, only the six zero eigenvalues corresponding to the six correct rigid body modes are obtained.

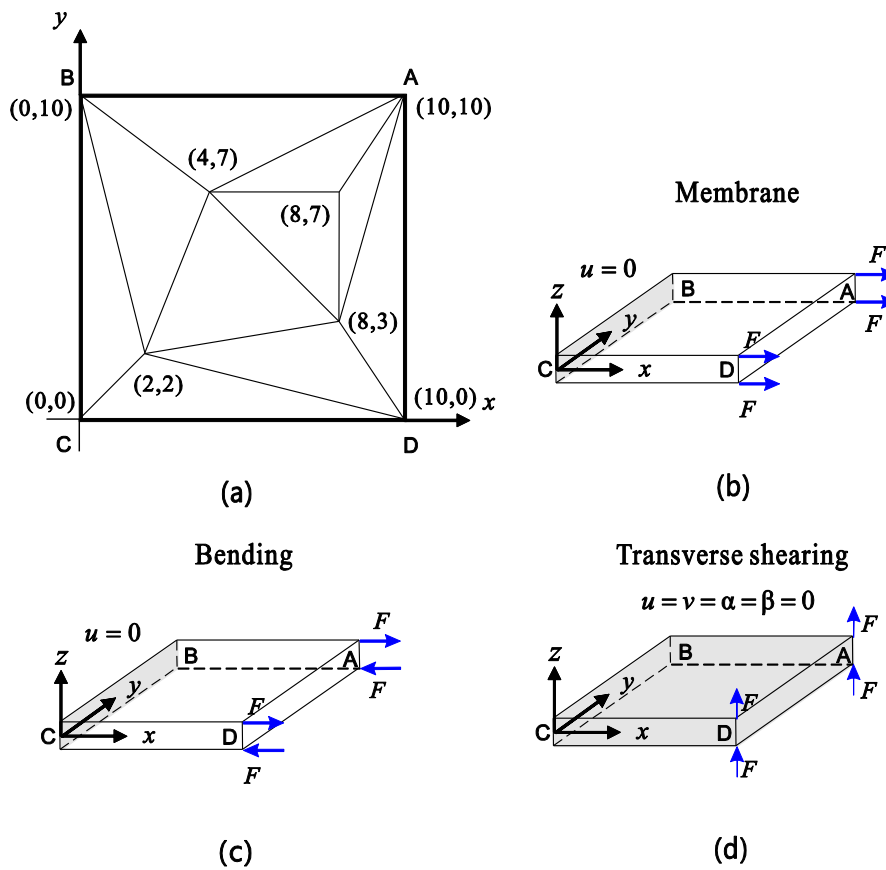


Fig. 3.5. Patch tests. (a) The mesh geometry. The loading and boundary conditions used for the (b) membrane, (c) bending, and (d) transverse shearing patch tests.

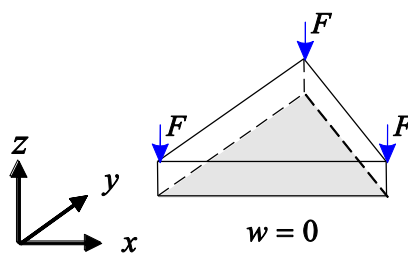


Fig. 3.6. An element used for the constant compression test.

3.4 Classical benchmark tests

Here, a set of widely-used linear benchmark problems are presented to test the proposed solid-shell elements. The problems considered are the fully clamped square plate problem, pinched cylinder problem, twisted beam problem, Scordelis-Lo roof problem and hyperboloid shell problems. As in

the literature, convergence is measured using a representative displacement in a specific location of the shell structure.

The solutions of the MITC-S6 solid-shell element are compared with those of the 6-node solid-shell element by Sze et al. [30], the 6-node solid-shell element, SC6R, used in the commercial software ABAQUS [109] and the 8-node solid-shell element in the literature, denoted as MITC-S8 [32-36,41].

3.4.1 Fully clamped square plate problem

The plate bending problem [5-8,30,32-34,38,39,42,90,93,108] is shown in Fig. 3.7. The square plate with dimensions of $2L \times 2L$ and thickness t is subjected to uniform pressure $q = 1.0$. Three different thicknesses, $t/L = 1/100$, $1/1000$ and $1/10000$ are considered with $L = 100$. The material properties used are $E = 1.0 \times 10^4$ and $\nu = 0.3$.

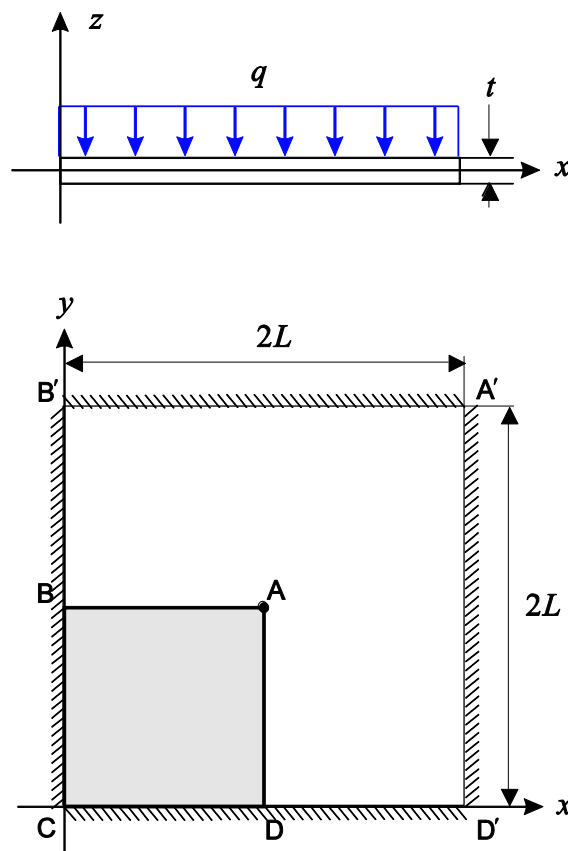


Fig. 3.7. Fully clamped square plate problem.

Due to symmetry, only a quarter of the plate corresponding to the shaded region ABCD in Fig. 3.7 is modeled with the mesh patterns shown in Fig. 3.8. The boundary conditions are $v=0$ along the edge AB, $u=0$ along the edge AD and $u=v=w=0$ along the edges CD and BC. $N \times N$ meshes are used with $N = 2, 4$ and 8 . For the case of $t/L = 1/100$, the reference vertical deflection is $w_{ref} = 1.384$. As the plate thickness becomes smaller, the deflection value varies with $(t/L)^3$.

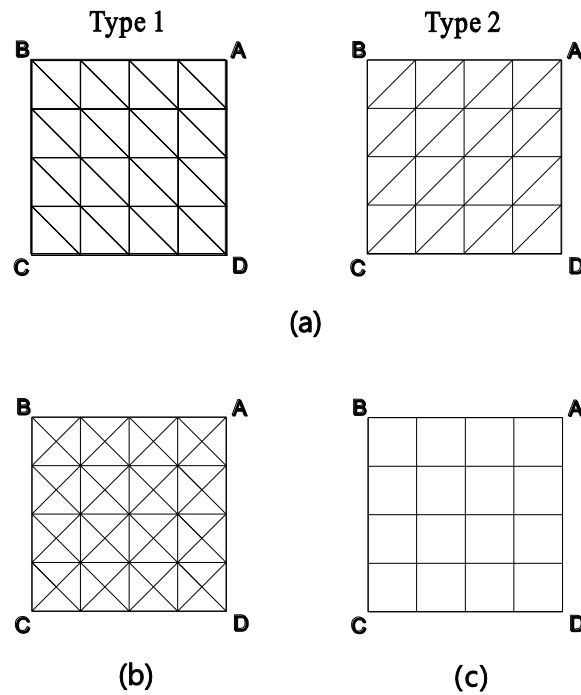


Fig. 3.8. Mesh patterns used for the benchmark tests: Regular meshes of (a) type 1 and (b) type 2 for triangular elements, (c) cross mesh for triangular elements and (d) regular mesh for quadrilateral elements.

Table 3.1 presents the vertical deflection at the plate center, w_A , normalized by the reference values. Figure 3.9 shows convergences of the normalized displacement, w_A / w_{ref} according to N . It is observed that the MITC-S6 element shows good convergences regardless of t/L and outperforms the 6-node solid-shell developed by Sze, compared in the cross mesh. In the regular mesh patterns (types 1 and 2) considered here, the predictive capability of the MITC-S6 triangular solid-shell element is comparable to that of the MITC-S8 quadrilateral solid-shell element. Note that, in plate bending problems, most triangular elements perform much better in a cross mesh than in regular meshes (types 1 and 2).

Table 3.1. Normalized vertical deflections at the plate center (point A) for the clamped plate problem. The mesh patterns are shown in Fig. 3.8.

t/L	N	Type 1		Type 2		Cross mesh			Regular
		regular mesh		regular mesh					mesh
		MITC-S6	SC6R	MITC-S6	SC6R	MITC-S6	SC6R	Sze et al.	MITC-S8
1/100	2	0.743	0.029	0.993	0.043	0.933	0.773	0.781	0.957
	4	0.925	0.554	1.000	0.668	0.981	0.937	0.946	0.988
	8	0.981	0.941	1.001	0.970	0.995	0.985	0.991	0.997
1/1000	2	0.741	0.001	0.991	0.001	0.931	0.771	0.778	0.956
	4	0.924	0.032	0.998	0.034	0.979	0.933	0.943	0.987
	8	0.979	0.557	0.999	0.484	0.993	0.982	0.987	0.995
1/10000	2	0.741	0.000	0.990	0.000	0.931	0.770	0.778	0.956
	4	0.923	0.006	0.998	0.006	0.979	0.933	0.943	0.987
	8	0.979	0.091	0.999	0.092	0.993	0.982	0.987	0.995

3.4.2 Pinched cylinder problem

The pinched cylinder problem [1,10,30,35,36,38,39,97,110,111], shown in Fig. 2.27, is considered. The cylinder structure of length $L = 600$, radius $R = 300$ and thickness $t = 3$ is supported by rigid diaphragms along its ends and is subjected to a pair of pinching forces, $F = 1.0$. The material properties used are $E = 3.0 \times 10^6$ and $\nu = 0.3$.

Only one-eighth of the structure corresponding to the shaded region ABCD in Fig. 2.27 is modeled. The boundary conditions are $u = 0$ along the edge AB, $v = 0$ along the edge AD, $w = 0$ along the edge CD, and $u = w = 0$ along the edge BC. $N \times N$ meshes are used with $N = 4, 6, 8, 10, 12, 14, 16$ and 32 .

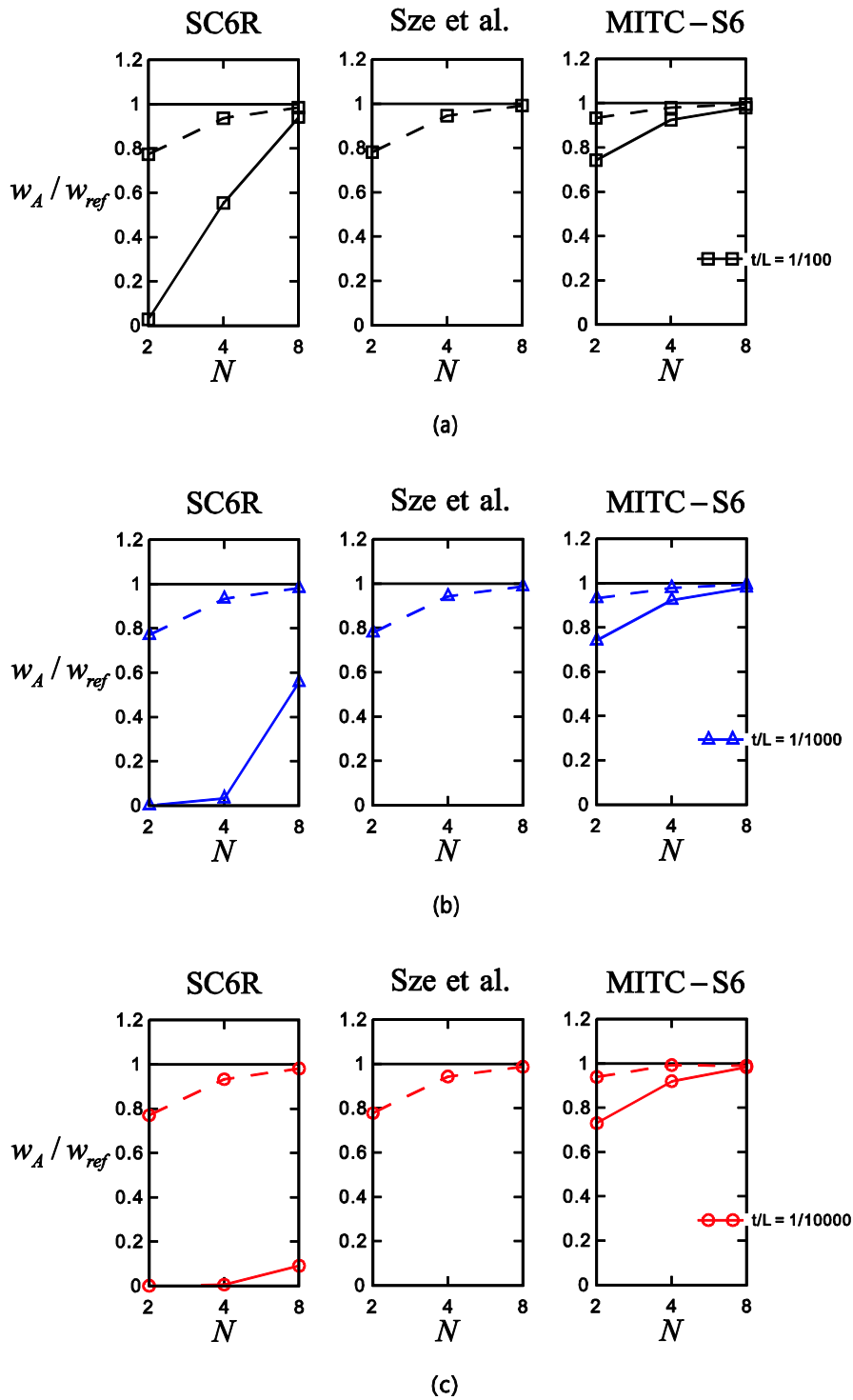


Fig. 3.9. Convergence of the normalized vertical deflections for the fully clamped square plate problem with (a) $t/L=1/100$, (b) $t/L=1/1000$ and (c) $t/L=1/10000$. The solid and dotted lines denote type 1 regular and cross mesh in Fig. 3.8, respectively. The horizontal line represents the exact vertical deflection.

Table 3.2 presents the vertical deflections at point A, w_A , normalized by the reference value of $w_{ref} = 1.8248 \times 10^{-5}$ [97]. Fig. 3.10 shows the convergence of w_A / w_{ref} . In this problem, the MITC-S6 solid-shell element outperforms both the SC6R solid-shell element and the 6-node solid-shell developed by Sze, and its performance is also comparable to that of the MITC-S8 quadrilateral solid-shell element.

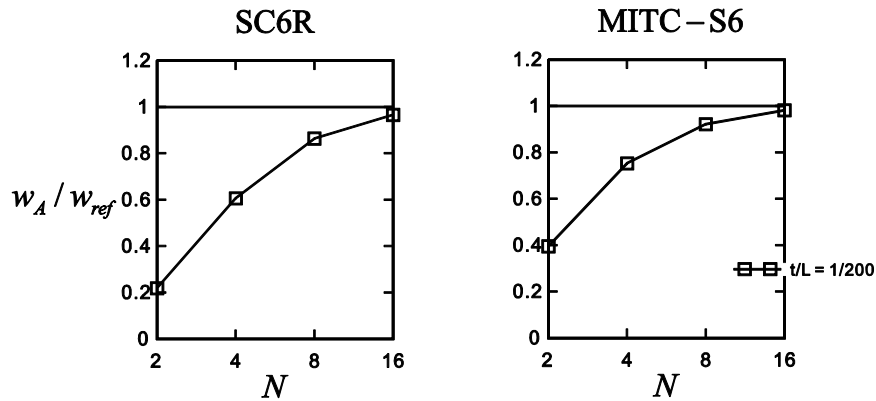


Fig. 3.10. Convergence of the normalized vertical deflections for the pinched cylinder problem with the type 1 regular mesh shown in Fig. 3.8. The horizontal lines represent the exact vertical deflection.

Table 3.2. Normalized vertical deflections of the cylinder at point A. The mesh patterns are shown in Fig. 3.8.

t/L	N	Type 1		Type 2		Cross mesh			Regular
		regular mesh		regular mesh		MITC-S6	SC6R	Sze et al.	mesh
		MITC-S6	SC6R	MITC-S6	SC6R				MITC-S8
0.005	4	0.395	0.218	0.424	0.196	0.498	0.331	0.354	0.379
	6	0.625	0.447	0.651	0.428	0.714	0.552	0.567	0.613
	8	0.753	0.606	0.771	0.589	0.824	0.685	0.695	0.747
	10	0.826	0.710	0.836	0.694	0.882	0.769	0.776	0.826
	12	0.871	0.780	0.876	0.765	0.915	0.825	0.829	0.875
	14	0.901	0.829	0.903	0.815	0.936	0.863	0.868	0.907
	16	0.921	0.864	0.923	0.851	0.951	0.891	-	0.929
	32	0.981	0.966	0.981	0.959	0.992	0.975	-	0.987

3.4.3 Twisted beam problem

The twisted beam problem [34,36,38,40,110,111] shown in Fig. 3.11 often has been considered to test membrane locking. A cantilever beam of length $L=12$, width $w=1.1$, and twist of 90° is loaded by concentrated forces at the center of free tip, point A. The material properties are $E = 2.9 \times 10^7$ and $\nu = 0.22$. The two different thicknesses, $t=0.32$ and $t=0.0032$ are considered.

The whole beam is modeled with $N \times N$ regular meshes with $N = 2, 4, 8, 16$ or 32 . Two loading cases are considered: in-plane (P) and out-of-plane (F) loadings. For $t=0.32$, $P = F = 1.0$ is used and the reference deflections at point A are $v_{ref} = 0.5424 \times 10^{-2}$ and $w_{ref} = 0.1754 \times 10^{-2}$ for in-plane and out-of-plane loadings, respectively [110]. For $t=0.0032$, $P = F = 1.0 \times 10^{-6}$ is used, and the reference deflections at point A are $v_{ref} = 0.5256 \times 10^{-2}$ and $w_{ref} = 0.1294 \times 10^{-2}$ for in-plane and out-of-plane loadings, respectively [110].

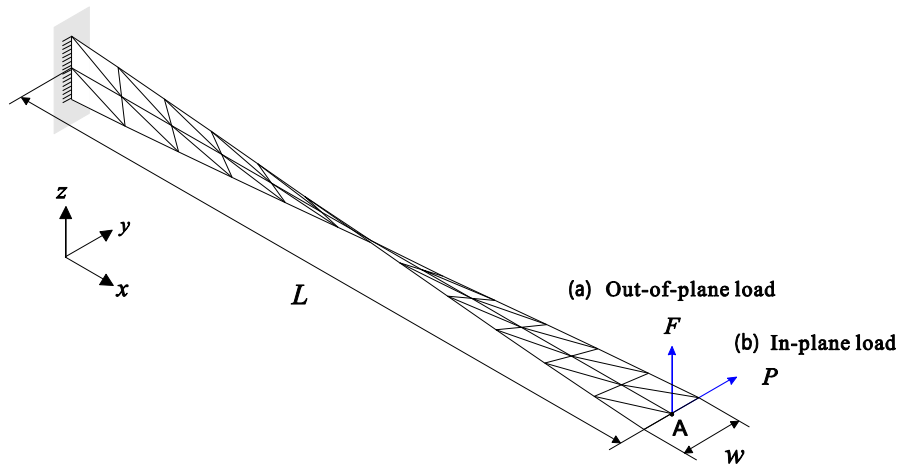


Fig. 3.11. Twisted beam problem. (a) Problem description (2×12 mesh). (a) Out-of-plane load case. (b) In-plane load case.

Table 3.3 presents the in-plane and out-of plane deflections at point A, v_A and w_A , normalized by the reference values of each. All the solid-shell elements considered here show excellent performance. Fig. 3.12 shows the convergence of v_A / v_{ref} and w_A / w_{ref} . All elements show nearly identical performances.

Table 3.3. Normalized deflections at the free end of the twisted beam in the direction of applied load.

t/L	Mesh	In-plane load			Out-of-plane load		
		MITC-S6	SC6R	MITC-S8	MITC-S6	SC6R	MITC-S8
0.0267 ($t = 0.32$)	2×12	0.981	0.996	0.990	0.832	0.825	0.918
	4×24	0.990	0.996	0.995	0.922	0.907	0.973
	8×48	0.995	0.999	0.997	0.973	0.967	0.991
0.000267 ($t = 0.0032$)	2×12	0.998	0.994	0.979	0.990	0.995	0.974
	4×24	0.988	0.985	0.991	0.990	0.992	0.992
	8×48	0.993	0.995	0.997	0.996	0.998	0.997

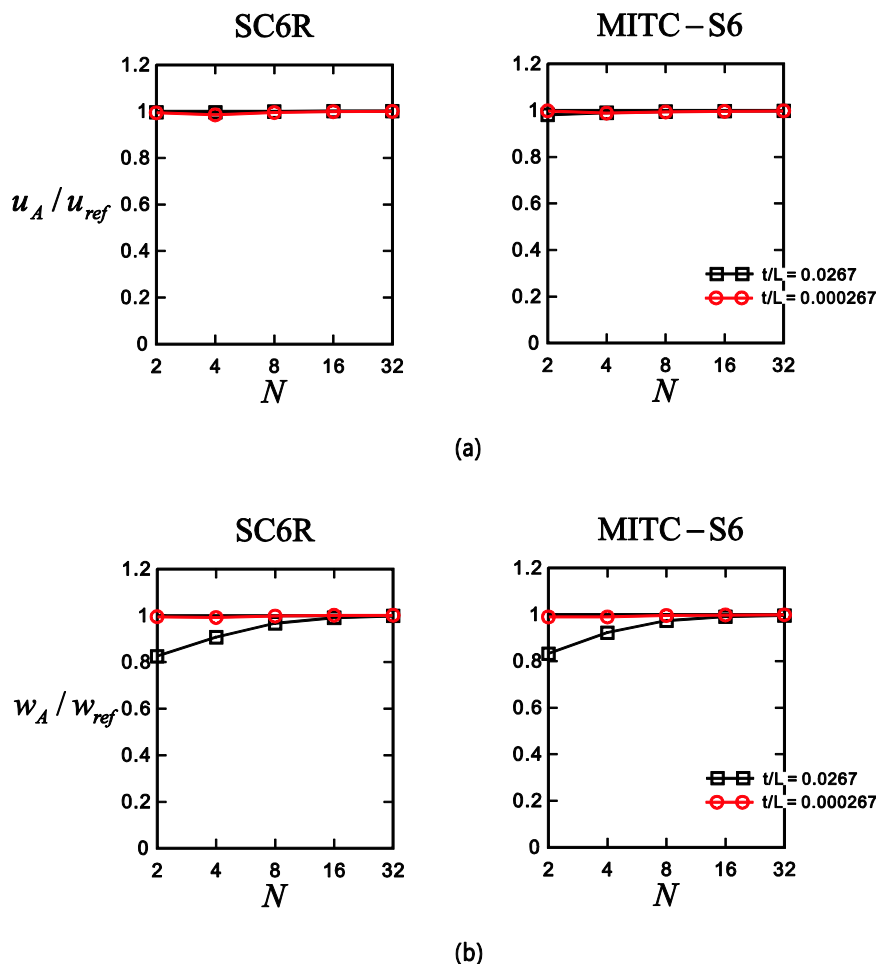


Fig. 3.12. Convergence of the normalized deflections for the twisted beam problem with (a) in-plane and (b) out-of-plane load cases. The horizontal lines represent the exact deflection.

3.4.4 Scordelis-Lo roof problem

The Scordelis-Lo roof problem [1,17,30,31,34,40,76,97,110] in Fig. 3.13 is considered. A roof structure of length $L=50$, radius $R=25$ and thickness $t=0.25$ is supported by rigid end diaphragms along its curved edges and is subjected to a self-weight with density $\rho=360$ and gravity constant $g=1.0$. Its material properties are $E=4.32 \times 10^8$ and $\nu=0.0$.

Only one quarter of the structure corresponding to the shaded region ABCD in Fig. 3.13 is modeled with the mesh patterns shown in Fig. 3.8. The boundary conditions are $v=0$ along the edge AD, $u=0$ along the edge AB and $u=w=0$ along the edge BC. $N \times N$ meshes are used with $N=4, 6, 8, 10, 12, 14, 16$ and 32 .

Table 3.4 shows the normalized vertical deflections at the center of free edge (point D), w_D , normalized by the reference value of $w_{ref} = 0.3024$ [97]. Fig. 3.14 shows the convergence of the normalized vertical deflections (w_D / w_{ref}) according to the mesh division N for the type 1 regular mesh of the 6-node solid-shell elements. The proposed solid-shell element outperforms the SC6R element.

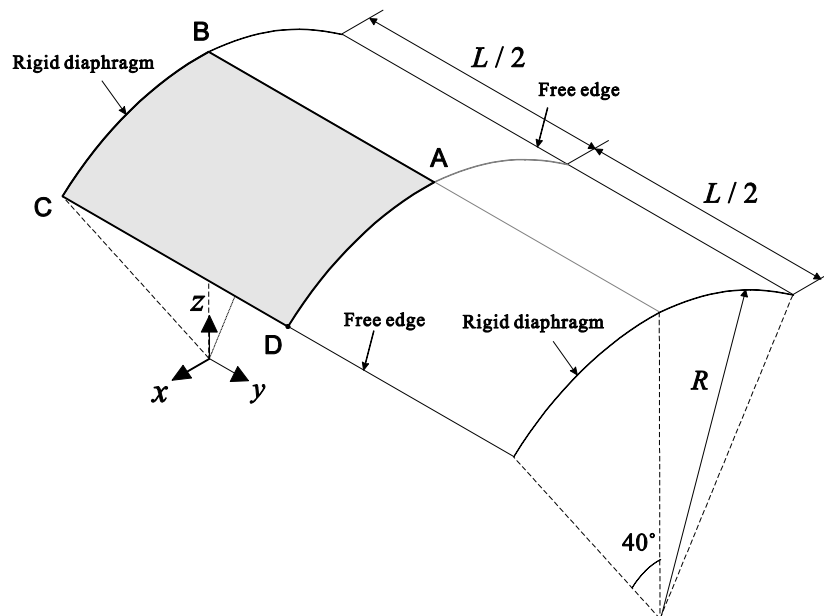


Fig. 3.13. Scordelis-Lo roof problem.

Table 3.4. Normalized vertical deflections at the center of free edge (point D) of the Scordelis-Lo roof problem. The mesh patterns are shown in Fig. 3.8.

t/L	N	Type 1		Type 2		Cross mesh			Regular
		regular mesh		regular mesh		MITC-S6	SC6R	Sze et al.	mesh
		MITC-S6	SC6R	MITC-S6	SC6R				
0.005	4	0.740	0.625	0.670	0.590	0.872	0.829	0.892	0.943
	6	0.819	0.735	0.786	0.704	0.923	0.890	0.946	0.960
	8	0.878	0.811	0.858	0.803	0.952	0.928	0.975	0.973
	10	0.914	0.863	0.900	0.858	0.967	0.951	0.992	0.980
	12	0.936	0.898	0.926	0.894	0.977	0.965	1.003	0.984
	14	0.951	0.921	0.943	0.919	0.984	0.974	1.014	0.987
	16	0.961	0.938	0.955	0.937	0.988	0.980	1.014	0.989
	32	0.987	0.986	0.985	0.985	1.010	0.997	-	0.994

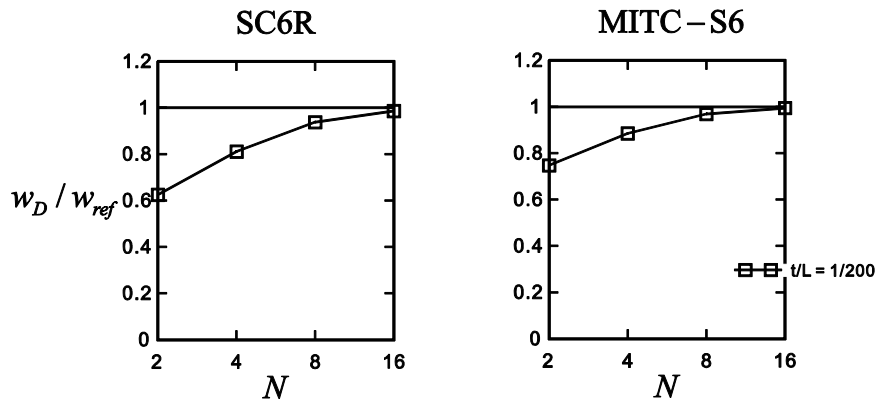


Fig. 3.14. Convergence of the normalized vertical deflections for the Scordelis-Lo roof problem with the type 1 regular mesh shown in Fig. 3.8. The horizontal lines represent the exact vertical deflection.

3.4.5 Pressurized cylinder problem

Here we additionally test effect of thickness locking using a simple test. Cylinder with radially applied pressure shown in Fig. 3.15 [118] is considered. The cylinder having radius $R = 10.0$ and thickness $t = 1.0$, under plane strain condition (z displacements are constrained), is subject-

ed to external pressure $p = 60$. Material properties are $E = 1.0 \times 10^4$ and $\nu = 0.0$. Let us denote the MITC-S6 without thickness locking treatment as MITC-S6i. If thickness locking is present, the stress in radial direction cannot vary linearly over the radial direction. A coordinate $\xi \in [-1,1]$ is set up for the radius $r = (R_i + R_o)/2 + (-R_i + R_o)\xi/2$ to vary from R_i to R_o . The cylinder is modeled with four meshes along the θ direction.

Fig. # shows the radial stresses (σ_{rr}) across the thickness of the MITC-S6 and MITC-S6i elements. Even though results obtained using this coarse mesh does not accurately represent thick-cylinder solution [118], the MITC-S6 element shows linearly varying radial stress in contrast with the MITC-S6i element. If meshes are refined, the solutions of both elements converge toward thin-cylinder solution of $\sigma_{rr} = -p/2$, which is constant over thickness. In order to accurately represent the stress of thick cylinder, three-dimensional shell using 7- or more parameters are necessary, such as in Ref. [118,119].

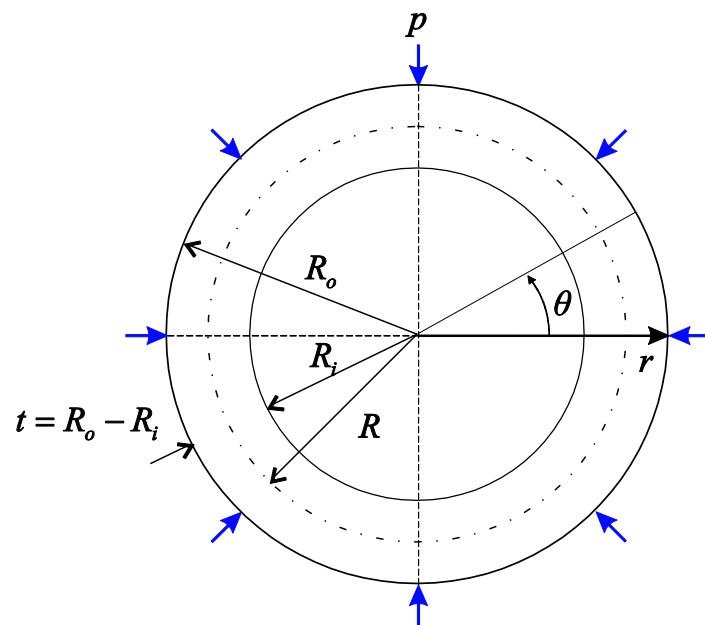


Fig. 3.15. Pressurized cylinder in plane strain condition.

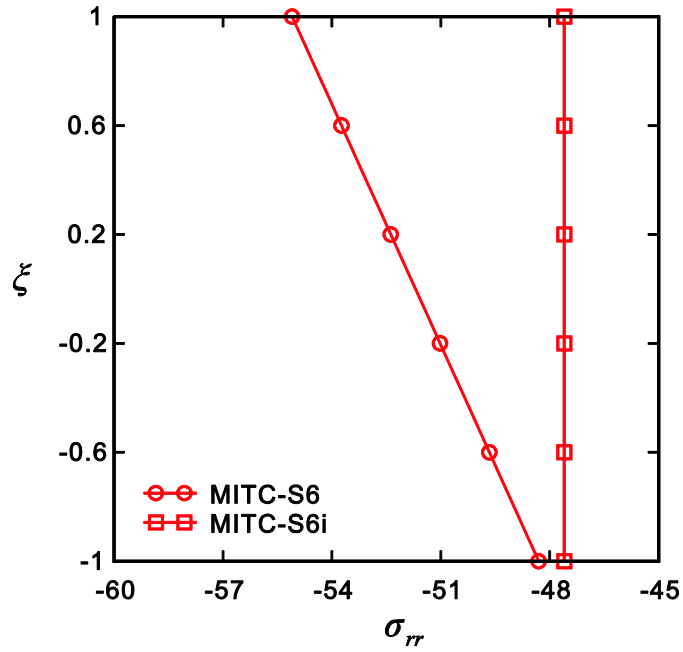


Fig. 3.16. Radial stresses across thickness of the pressurized cylinder.

3.5 Detailed convergence studies

In this section, in-depth convergence studies of solid-shell elements are performed for plate and hyperboloid shell structures with various values of t/L . Unlike the previous section where the benchmark problems are solved using only regular meshes of solid-shell elements, the behaviors of the elements adapting to irregular meshes are also tested.

Solution convergences are measured using the following normalized strain energy error \bar{E}_h ,

$$\bar{E}_h = \left| \frac{E_{ref} - E_h}{E_{ref}} \right|, \quad (3.34)$$

in which E_h and E_{ref} denote strain energies obtained from the finite element and reference solutions, respectively. Optimal convergence for low-order elements considered in this study is obtained if $\bar{E}_h \cong ch^2$, where c is a constant independent of the shell thickness and h is the element size.

In order to investigate how much thickness locking deteriorates the solution accuracy, an intermediate 6-node solid-shell element is also implemented: MITC-S6 without thickness locking treatment (MITC-S6i). The solutions obtained using the MITC-S6 and MITC-S6i solid-shell elements are compared with those of the MITC-S8 solid-shell elements.

3.5.1 Fully clamped square plate problem

To further study the solution convergence of the solid-shell elements with various values of t/L , the plate bending problem in Fig. 3.7 is again solved with geometric and material constants [5-8,108] in Fig. 2.13.

To avoid difference between regular meshes (type 1 and type 2), the whole plate shown in Fig. 3.7 is modeled with the regular mesh pattern shown in Fig. 3.8. The boundary conditions are

$u = v = w = 0$ along the edges $A'B'$, $B'C'$, $C'D'$ and $D'A'$. $N \times N$ meshes are used with $N = 4, 8, 16$ and 32 .

In order to study the performance of the solid-shell elements in irregular meshes, the mesh patterns shown in Fig. 3.17(a) and (b) are also considered for the triangular and quadrilateral elements, respectively, where each edge is discretized in the following ratio: $L_1 : L_2 : L_3 : \dots = 1 : 2 : 3 : \dots : N$ [5-8]. The similar distorted mesh patterns have been used for testing triangular elements, see Refs. [38,39].

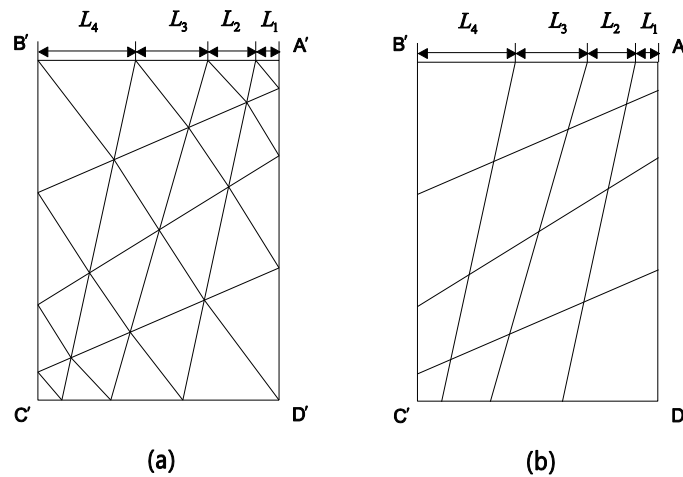


Fig. 3.17. Irregular mesh patterns used ($N = 4$) for (a) triangular and (b) quadrilateral elements.

The reference solutions are obtained using a 72×72 uniform mesh of MITC9 shell elements [12,18].

Fig. 3.18 shows the convergence curves of the solid-shell elements when the regular and irregular

mesh patterns are used. The element size in the convergence curves is $h = L/N$. The performance of the MITC-S6 solid-shell element is again comparable to that of the MITC-S8 solid-shell element, and is particularly better when the irregular mesh pattern is used. On the other hand, the convergence of the MITC-S6i solid-shell element severely deteriorates and the errors do not diminish well with the mesh refinement. This is due to the Poisson thickness locking, and the optimal convergence behavior is successfully recovered through the EAS technique.

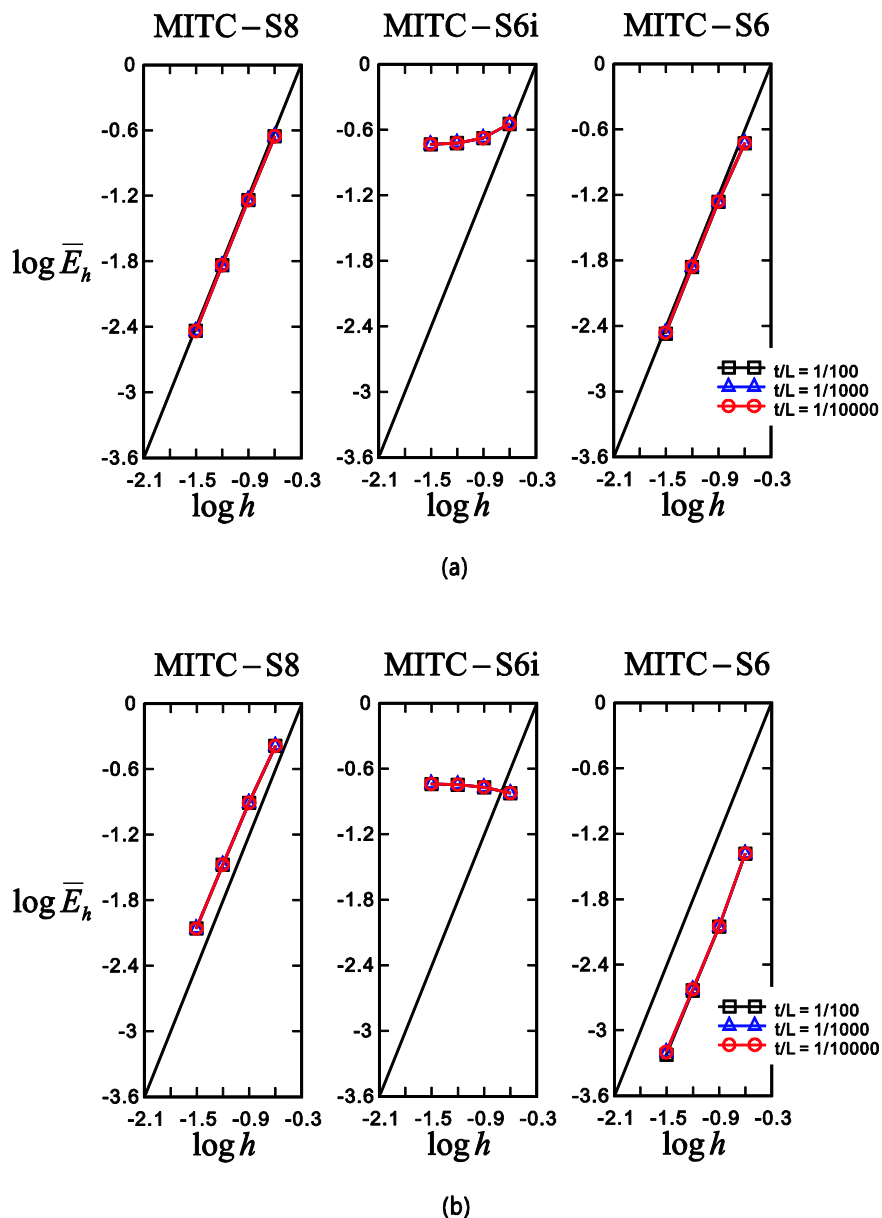


Fig. 3.18. Convergence curves for the fully clamped square plate problem with the (a) regular and (b) irregular mesh patterns shown in Fig. 3.17. The bold lines represent the optimal convergence rate.

3.5.2 Hyperboloid shell problems

The hyperboloid shell problem [5-8,12,18,100] shown in Fig. 2.19(a) is considered. The mid-surface of the shell surface is given by Eq. (2.82) and a smoothly varying pressure in Eq. (2.81) is applied.

A bending-dominated behavior is obtained with free ends and a membrane-dominated behavior is given with clamped ends.

Due to symmetry, only one-eighth of the structure corresponding to the shaded region ABCD in Fig. 2.19(a) is modeled for the analysis. For the membrane-dominated case, the clamped boundary condition is imposed: $u_z = \beta = 0$ along DC, $u_x = \beta = 0$ along AB, $u_y = \alpha = 0$ along AD, and $u_x = u_y = u_z = \alpha = \beta = 0$ along BC. For the bending-dominated case, the free boundary condition is imposed: $u_z = \beta = 0$ along DC, $u_x = \beta = 0$ along AB, and $u_y = \alpha = 0$ along AD. For both cases, $N \times N$ meshes are used with $N = 4, 8, 16$ and 32 .

For the membrane-dominated case, the regular mesh graded in a boundary layer of width $6\sqrt{t}$ shown in Fig. 2.19(b) is considered, see Refs. [7,18,21]. For the bending-dominated case, the regular mesh is graded in a boundary layer of width $0.5\sqrt{t}$ [18,21]. The convergence studies are also performed with the distorted meshes shown in Fig. 3.17(a) and (b). The points in the figures are matched as follows: A is equal to A', B is equal to B', C is equal to C' and D is equal to D'. Note that for this hyperboloid shell problems type 1 and type 2 regular meshes shown in Fig. 3.8(a) yields almost identical results.

Fig. 3.19 shows the convergence curves of the solid-shell elements for the regular and irregular mesh patterns when the clamped boundary condition is imposed. A 72×72 uniform mesh of MITC9 shell elements is used to obtain the reference strain energy. The element size is $h = L/N$. The performance of the MITC-S6 solid-shell element is similar to that of the MITC-S8 solid-shell element. As expected, it is observed that thickness locking is inherently not present in this membrane-dominated problem.

Fig. 3.20 shows the convergence curves of the solid-shell elements when the free boundary condition is used. In both regular and irregular meshes, the MITC-S6 solid-shell element presents excellent convergence behavior, while the convergence of the MITC-S8 solid-shell element severely deteriorates for the case of irregular mesh. This is due to membrane locking, which is investigated in detail in Ref. [5]. In addition, thickness locking manifests even more severely for this problem, notably from both curvature and Poisson thickness locking. The combined use of the assumed strain and EAS techniques for thickness strain indeed facilitates solution convergence in this doubly-curved shell problem.

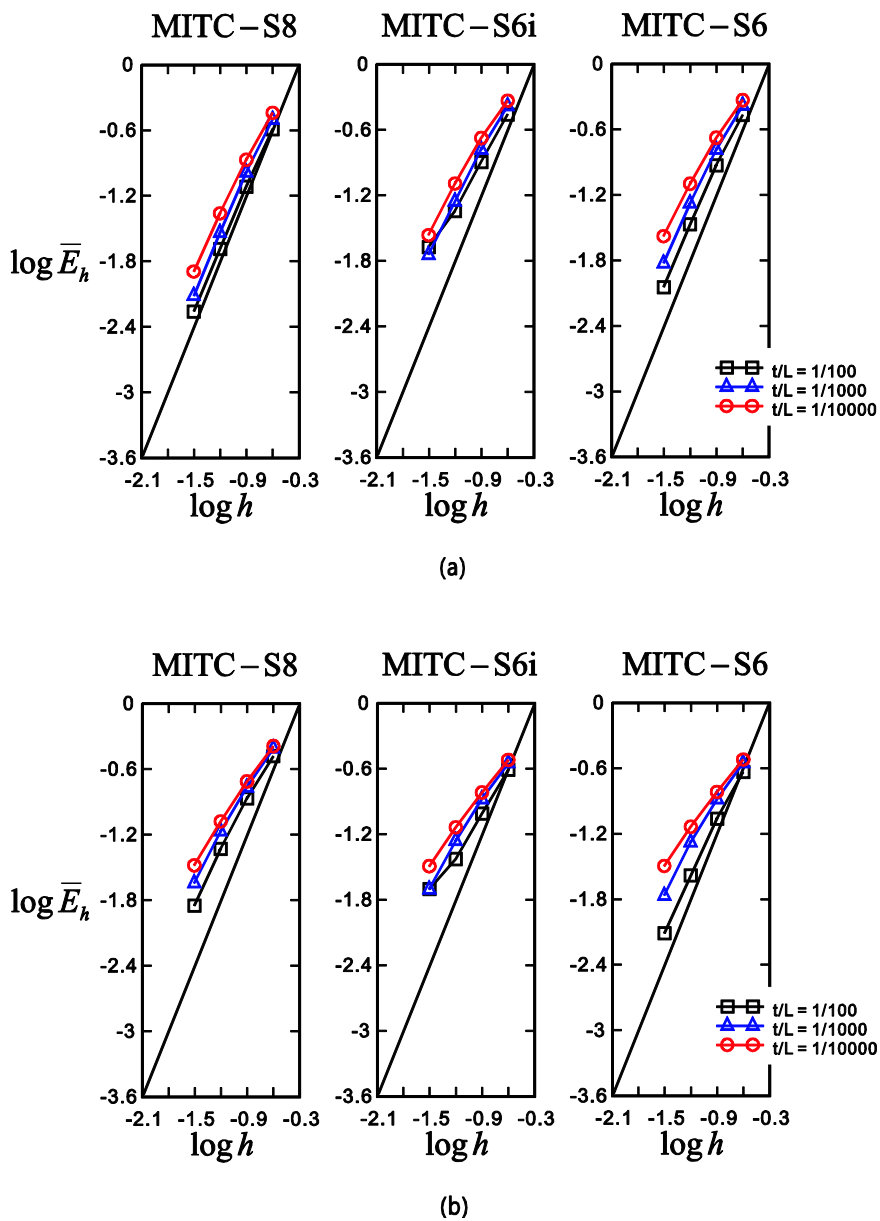


Fig. 3.19. Convergence curves for the clamped hyperboloid shell problem with the (a) regular and (b) irregular mesh pattern shown in Fig. 3.17. The bold lines represent the optimal convergence rate.

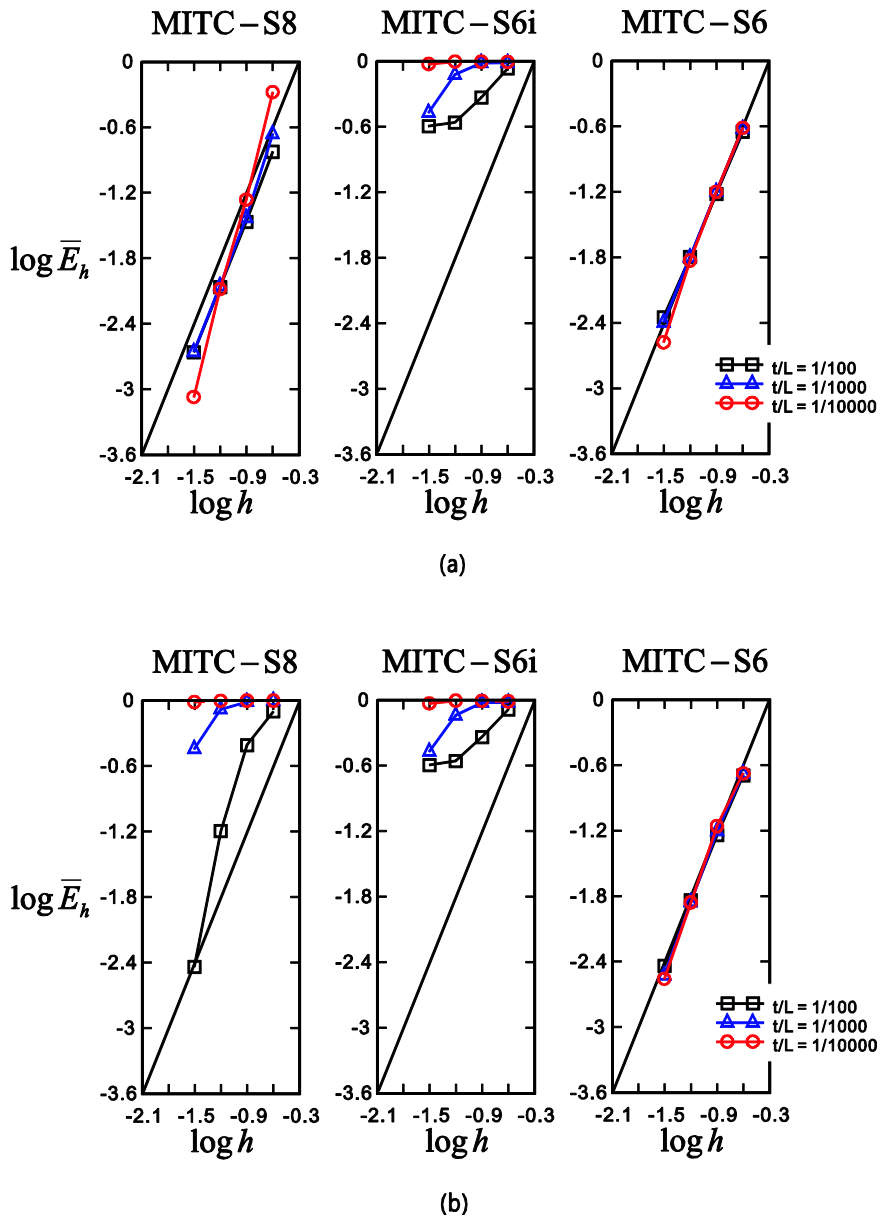


Fig. 3.20. Convergence curves for the free hyperboloid shell problem with the (a) regular and (b) irregular mesh pattern shown in Fig. 3.17. The bold lines represent the optimal convergence rate.

3.6 Geometric nonlinear analysis

In this section, the performance of the MITC-S6 solid-shell element is presented in the numerical examples involving large displacements and large rotations through three shell problems: a cantilever beam under shear tip force and a pinched cylindrical shell [111,115,116].

3.6.1 Cantilever under end shearing force

Here consider cantilever under end shearing force shown in Fig. 2.30(b) is considered again. The cantilever is modeled with 8×1 mesh of the proposed 6-node solid-shell elements. Fig. 3.21 shows the load-displacement curves: non-dimensional applied load PL^2/EI (with $I = bt^3/12$) versus non-dimensional tip displacements u_{tip}/L and w_{tip}/L . The load-displacement curves are in very good agreement with those obtained by Sze et al. [115]. Deformed shapes for load levels $P=1.0$, 2.0 and 4.0 are shown in Fig. 3.22.

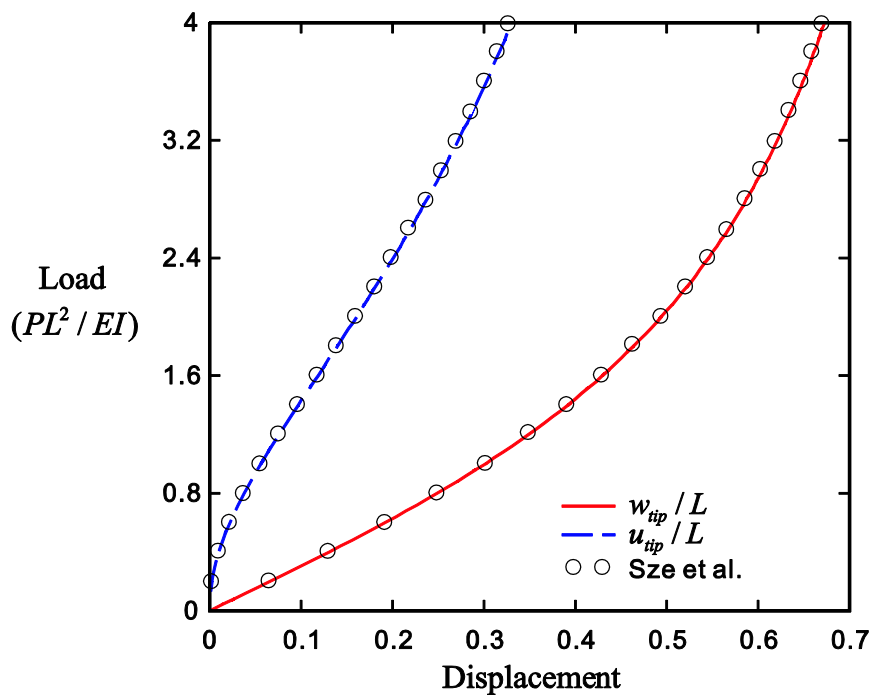


Fig. 3.21. Load-displacement curve for the cantilever beam under end shearing force.

3.6.2 Pinched cylindrical shell

The pinched cylindrical shell problem [111,115,116] is considered here, see Fig. 3.23. The cylinder of length $L = 3.048$, radius $R = 1.016$ and thickness $t = 0.03$ is clamped at one end and is subjected to a pair of concentrated forces F at the free end. The material properties used are $E = 2.0685 \times 10^7$ and $\nu = 0.3$. Due to symmetry, only one quarter of the cylinder is modeled using 14×14 meshes of the proposed 6-node solid-shell elements. As in Ref. [111], the analysis was

performed neglecting the possible contact within the shell structure up to the maximum force $P = 2.0 \times 10^3$.

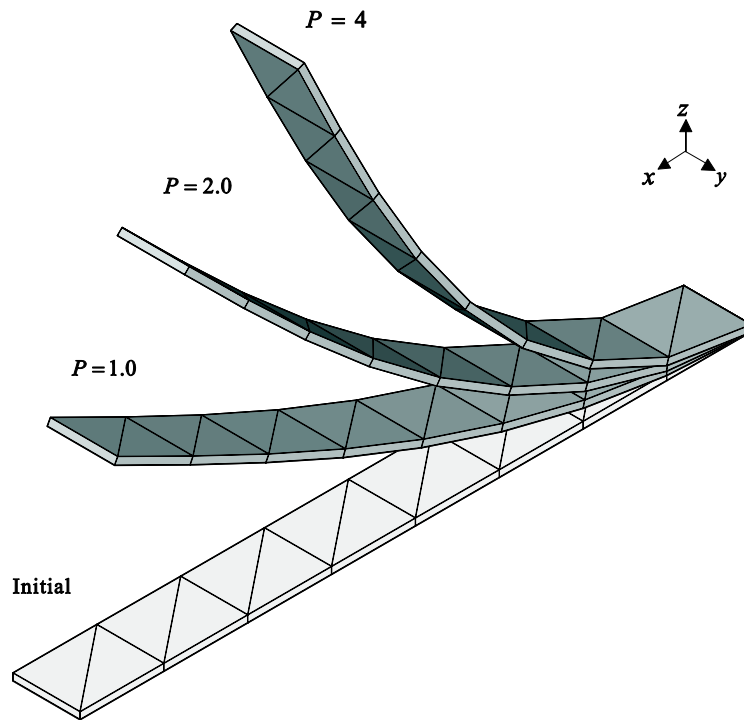


Fig. 3.22. Deformed shapes at shear tip forces $P = 1.0$, 2.0 or 4.0 for the cantilever beam problem.

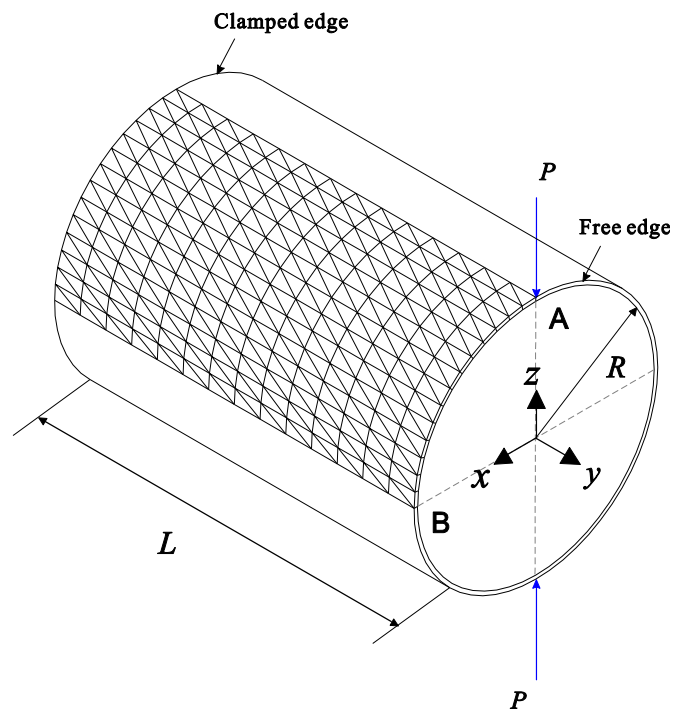


Fig. 3.23. Pinched cylindrical shell.

The radial displacements at points A and B of the shell are shown in Fig. 3.24. The overall load-displacement curves are in good agreement with Refs. [111,115,116]. The deformed shape at $P = 700$ is shown in Fig. 3.25.

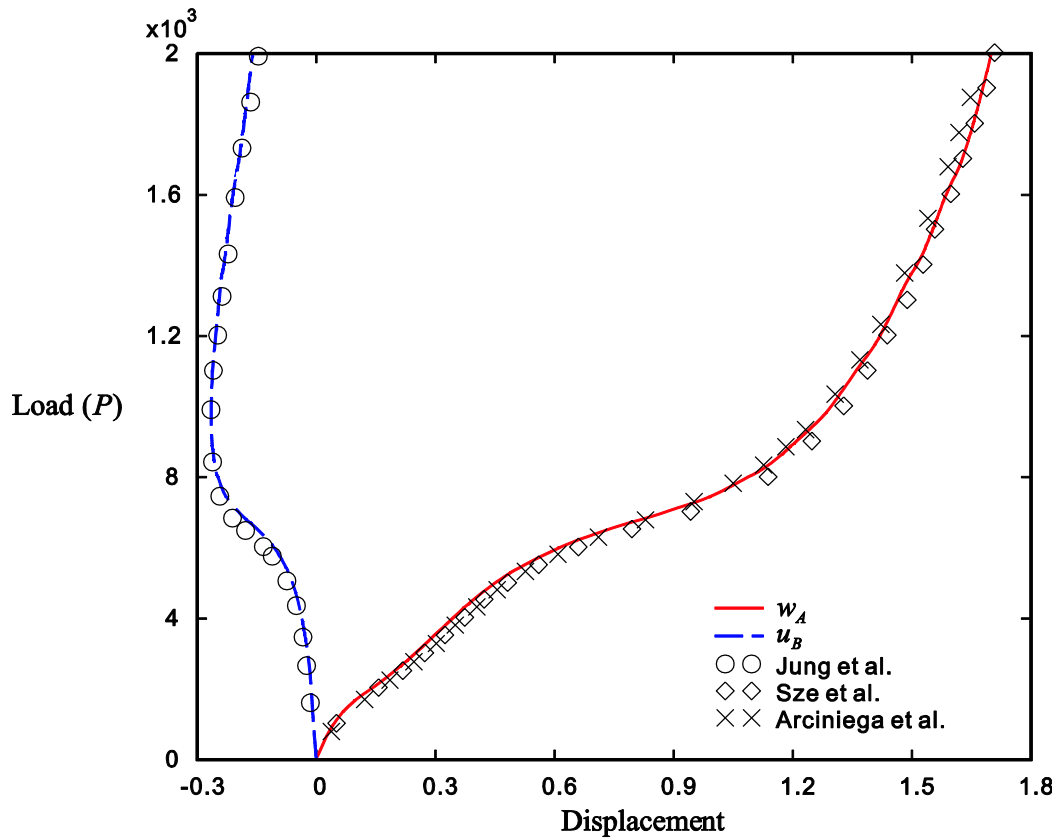


Fig. 3.24. Load-displacement curves for the pinched cylindrical shell.

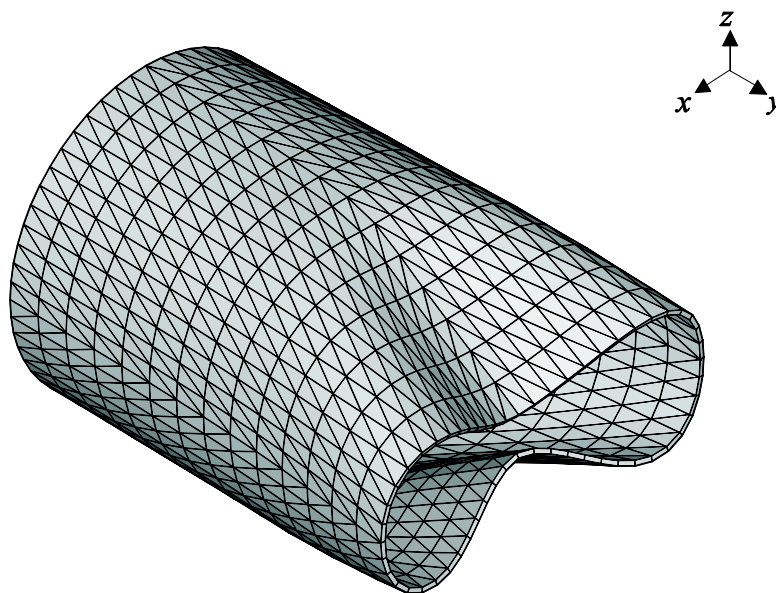


Fig. 3.25. Deformed shape at $P = 700$ for the pinched cylindrical shell.

3.7 Conclusions

In this study, a new 6-node solid-shell element is developed by extending the previous 3-node MITC3+ shell element, in which assumed transverse shear strain field of the MITC3+ shell element is adopted onto the new MITC-S6 solid-shell element. The concept of enhancing the bending mechanism using the cubic bubble function is similar to the MITC3+ shell element, but in this solid-shell element the mechanism is applied for the in-plane translation of the shell element through the EAS method. To avoid Poisson thickness locking, the thickness stretch mechanism is enhanced to include quadratic variation in the thickness direction. The assumed constant thickness strain is adopted to avoid curvature thickness locking.

The new MITC-S6 solid-shell element satisfies basic tests and achieves uniformly optimal convergence on various shell problems considered in this study while providing a simple formulation, as in the MITC3+ shell element. The MITC-S6 solid-shell element also maintains various advantages in computational aspects of nonlinear simulations: No rotation updates are necessary and the general three-dimensional material law is directly used, which facilitates further application of the present solid-shell element to the analysis of elastoplastic behavior of shell structures when thickness change is important [119].

On the other hand, computational cost increases due to added internal degrees of freedom, and the resulting MITC-S6 shell element has purely numerical parameter, $d = 1/100,000$. A study to overcome such limitations would be greatly valuable.

Chapter 4. Conclusions

In this study, two different types of shell elements are developed: 4-node quadrilateral shell element and 6-node triangular solid-shell elements, both of which are low-order shell elements.

In the development of 4-node quadrilateral shell elements, the cause of locking phenomenon present in the displacement-based membrane strain was investigated for general element under out-of-plane distortion. In the series of developments, the MITC4+, MITC4+N and new MITC4+, different creative approaches are applied for curing such locking mechanism.

In the MITC4+ shell element, the bilinear interpolation was removed by subdividing the mid-surface and applying triangular interpolation, which are subsequently applied with new assumed strain method including transformation. This approach remedied membrane locking to some degree, but membrane performance as well as pass of membrane patch tests was not retained. In the MITC4+N shell element, the similar assumed strain method as in the MITC4+ shell element were applied, the membrane subdivision was maintained, but the interpolation was done on the whole quadrilateral domain. The fact that MITC4+N shell element alleviates membrane locking in the same degree as the MITC4+ shell element means assumed strain, not the interpolation function, is the key to achieve better bending performance under out-of-plane mesh distortion.

In the new MITC4+ shell element, the idea of Choi and Paik [2], Kulikov [3], among many others were adopted to develop new assumed strain for the 4-node quadrilateral shell element that behaves optimally on bending problems but also retains the membrane performance. The assumed strain is constructed from five tied strain components as well as coefficients that come from characteristic geometry vectors of the mid-surface. The resulting element passes basic tests and significantly improves convergence behaviors, and also retains the robustness in geometric nonlinear simulation of the original MITC4 shell element.

In the development of 6-node triangular solid-shell element, the previous literatures on shear and

thickness locking were searched. Shear locking treatment of 3-node MITC triangular shell element, MITC3+, and commonly used treatment of thickness locking, EAS method, were applied into the 6-node solid-shell element. The resulting element passes basic tests, performs particularly well in convergence studies and show good agreement with other literatures in geometric nonlinear analysis examples.

In future works, any further numerical or theoretical study to overcome limitations of the new-MITC4+ shell element and the MITC-S6 solid-shell element would be valuable. As a succession of the present work, reducing membrane locking within 4-node quadrilateral shell elements by making use of the recent methods such as IGA [25-27] can be of particular interest. In addition, membrane locking phenomenon should be tested for more arbitrary (generally distorted and unstructured) meshes other than the ones presented in this paper. I believe that reduction of dominant locking phenomena, shear and membrane locking, in low-order shell element has been performed quite successfully up to limiting point (MITC3+ and MITC4+). Hence, applying the extended FEM [23,24] to avoid possible locking that may present in more general meshes can be valuable.

References

- [1] Dvorkin EN, Bathe KJ. A continuum mechanics based four-node shell element for general nonlinear analysis. *Eng Comput* 1984;1(1):77-88.
- [2] Choi CK, Paik JG. An efficient four node degenerated shell element based on the assumed covariant strain. *Struct Eng Mech* 1994;2(1):17-34.
- [3] Kulikov GM, Plotnikova SV. A family of ANS four-node exact geometry shell elements in general connected curvilinear coordinates. *Int J Num Meth Eng* 2010;83(10):1376-406.
- [4] Roh HY, Cho M. The application of geometrically exact shell elements to B-spline surfaces. *Comp Meth Appl Mech Eng* 2004;193(23):2261-99.
- [5] Ko Y, Lee PS, Bathe KJ. The MITC4+ shell element and its performance. *Comput Struct* 2016;169:57-68.
- [6] Lee PS, Bathe KJ. Development of MITC isotropic triangular shell finite elements. *Comput Struct* 2004;82(11):945-62.
- [7] Lee Y, Lee PS, Bathe KJ. The MITC3+ shell element and its performance. *Comput Struct* 2014;138:12-23.
- [8] Lee Y, Yoon K, Lee PS. Improving the MITC3 shell finite element by using the Hellinger-Reissner principle. *Comput Struct* 2012;110-111:93-106.
- [9] Kim DN, Bathe KJ. A triangular six-node shell element. *Comput Struct* 2009;87(23), 1451-460.
- [10] Bucalem ML, Bathe KJ. Higher-order MITC general shell elements. *Int J Num Meth Eng* 1993;36(21):3729-54.
- [11] da Veiga LB, Chapelle D, Suarez IP. Towards improving the MITC6 triangular shell element. *Comput*

Struct 2007;85(21):1589-610.

[12] Bathe KJ, Lee PS, Hiller JF. Towards improving the MITC9 shell element. *Comput Struct* 2003;81(8):477-89.

[13] Bathe KJ, Dvorkin EN. A formulation of general shell elements—the use of mixed formulation of tensorial components. *Int J Num Meth Eng* 1986;22(3):697-722.

[14] Bucalem ML, Bathe KJ. Finite element analysis of shell structures. *Archiv Comp Meth Eng* 1997;4(1):3-61.

[15] Bathe KJ. Finite element procedures. Prentice Hall; 1996, 2nd edition KJ Bathe, Watertown, MA, 2014.

[16] Bathe KJ. The inf–sup condition and its evaluation for mixed finite element methods. *Comput Struct* 2001;79(2):243–52.

[17] Lee PS, Bathe KJ. On the asymptotic behavior of shell structures and the evaluation in finite element solutions. *Comput Struct* 2002;80(3):235-55.

[18] Hiller JF, Bathe KJ. Measuring convergence of mixed finite element discretizations: an application to shell structures. *Comput Struct* 2003;81(8):639-54.

[19] Chapelle D, Bathe KJ. Fundamental considerations for the finite element analysis of shell structures. *Comput Struct* 1998;66(1):19-36,711-2.

[20] Bathe KJ, Iosilevich A, Chapelle D. An inf-sup test for shell finite elements. *Comput Struct* 2000;75(5):439-56.

[21] Chapelle D, Bathe KJ. The finite element analysis of shells – fundamentals. Berlin: Springer; 2003.; 2nd edition, 2011.

[22] Bathe KJ, Iosilevich A, Chapelle D. An evaluation of the MITC shell elements. *Comput Struct* 2000;75(1):1-30.

- [23] Nguyen-Thanh N, Rabczuk T, Nguyen-Xuan H, Bordas SP. A smoothed finite element method for shell analysis. *Comp Meth Appl Mech Eng* 2008;198(2):165-77.
- [24] Wyart E, Coulon D, Duflot M, Pardoën T, Remacle JF, Lani F. A substructured FE-shell/XFE-3D method for crack analysis in thin-walled structures. *Int J Num Meth Eng* 2007;72(7):757-79.
- [25] Benson DJ, Bazilevs Y, Hsu MC, Hughes TJR. A large deformation, rotation-free, isogeometric shell. *Comp Meth Appl Mech Eng* 2011;200(13):1367-78.
- [26] Nguyen-Thanh N, Kiendl J, Nguyen-Xuan H, Wüchner R, Bletzinger KU, Bazilevs Y, Rabczuk T. Rotation free isogeometric thin shell analysis using PHT-splines. *Comp Meth Appl Mech Eng* 2011;200(47):3410-24.
- [27] Echter, R., Oesterle, B., & Bischoff, M. (2013). A hierarchic family of isogeometric shell finite elements. *Computer Methods in Applied Mechanics and Engineering*, 254, 170-180.
- [28] Lee PS, Noh HC, Bathe KJ. Insight into 3-node triangular shell finite elements: the effects of element isotropy and mesh patterns. *Comput Struct* 2007;85(7):404-18.
- [29] Chapelle D, Bathe KJ. The mathematical shell model underlying general shell elements. *Int J Num Meth Eng* 2000;48(2):289-313.
- [30] Sze KY, Chan WK. A six-node pentagonal assumed natural strain solid-shell element. *Fin Elem Anal Des* 2001;37(8):639-55.
- [31] Flores FG. Development of a non-linear triangular prism solid-shell element using ANS and EAS techniques. *Comp Meth Appl Mech Eng* 2013;266:81-97.
- [32] Klinkel S, Gruttmann F, Wagner W. A robust non-linear solid shell element based on a mixed variational formulation. *Comp Meth Appl Mech Eng* 2006;195(1):179-201.
- [33] Klinkel S, Gruttmann F, Wagner W. A continuum based three-dimensional shell element for laminated

structures. *Comput Struct* 1999;71(1):43-62.

[34] Schwarze M, Reese S. A reduced integration solid-shell finite element based on the EAS and the ANS concept—Geometrically linear problems. *Int J Num Meth Eng* 2009;80(10): 1322-55.

[35] Hauptmann R, Schweizerhof K. A systematic development of ‘solid-shell’ element formulations for linear and non-linear analyses employing only displacement degrees of freedom. *Int J Num Meth Eng* 1998;42:49–69.

[36] Sze KY, Yao LQ. A hybrid stress ANS solid-shell element and its generalization for smart structure modeling. Part I—solid-shell element formulation. *Int J Num Meth Eng* 2000;48(4):545-64.

[37] Sze KY, Chan WK, Pian THH. An eight-node hybrid-stress solid-shell element for geometric non-linear analysis of elastic shells. *Int J Num Meth Eng* 2002;55(7):853-78.

[38] Kim JH, Kim YH, Lee SW. An assumed strain formulation of efficient solid triangular element for general shell analysis. *Int J Num Meth Eng* 2000;47(8):1481-97.

[39] Hong WI, Kim JH, Kim YH, Lee SW. An assumed strain triangular curved solid shell element formulation for analysis of plates and shells undergoing finite rotations. *Int J Num Meth Eng* 2001;52(7):747-61.

[40] Sze KY, Zhu D. A quadratic assumed natural strain curved triangular shell element. *Comp Meth Appl Mech Eng* 1999;174(1):57-71.

[41] Harnau M, Schweizerhof K. About linear and quadratic ‘solid-shell’ elements at large deformations. *Comput Struct* 2002;80:805-17.

[42] Kim CH, Sze KY, Kim YH. Curved quadratic triangular degenerated-and solid-shell elements for geometric non-linear analysis. *Int J Num Meth Eng* 2003;57(14):2077-97.

[43] Kemp BL, Cho C, Lee SW. A four-node solid shell element formulation with assumed strain. *Int J Num Meth Eng* 1998;43(5):909-24.

- [44] Hauptmann R, Schweizerhof K, Doll S. Extension of the 'solid-shell' concept for application to large elastic and large elastoplastic deformations. *Int J Num Meth Eng* 2000;49(9):1121-41.
- [45] Alves de Sousa RJ, Cardoso RP, Fontes Valente RA, Yoon JW, Grácio JJ, Natal Jorge RM. A new one-point quadrature enhanced assumed strain (EAS) solid-shell element with multiple integration points along thickness: Part I—geometrically linear applications. *Int J Num Meth Eng* 2005;62(7):52-77.
- [46] Kim KD, Liu GZ, Han SC. A resultant 8-node solid-shell element for geometrically nonlinear analysis. *Comput Mech* 2005;35(5):315-31.
- [47] Cardoso RP, Yoon JW, Mahardika M, Choudhry S, Alves de Sousa RJ, Fontes Valente RA. Enhanced assumed strain (EAS) and assumed natural strain (ANS) methods for one-point quadrature solid-shell elements. *Int J Num Meth Eng* 2008;75(2):156-87.
- [48] Kulikov GM, Plotnikova SV. Finite rotation geometrically exact four-node solid-shell element with seven displacement degrees of freedom. *Comp Model Eng Sci* 2008; 28(1):15-38.
- [49] Simo JC, Fox DD. On a stress resultant geometrically exact shell model. Part I: Formulation and optimal parametrization. *Comp Meth Appl Mech Eng* 1989;72(3):267-304.
- [50] Trinh VD, Abed-Meraim F, Combescure A. A new assumed strain solid-shell formulation “SHB6” for the six-node prismatic finite element. *J Mech Sci Tech* 2011;25(9):2345-64.
- [51] Bathe KJ, Ho LW. A simple and effective element for analysis of general shell structures. *Comput Struct* 1981;13(5):673-81.
- [52] Ibrahimbegovic A, Wilson EL. A unified formulation for triangular and quadrilateral flat shell finite elements with six nodal degrees of freedom. *Com Appl Num Meth* 1991;7(1):1-9.
- [53] Aminpour MA. An assumed-stress hybrid 4-node shell element with drilling degrees of freedom. *Inter J Num Meth Eng* 1992;33(1):19-38.

- [54] Cook RD. Four-node 'flat' shell element: drilling degrees of freedom, membrane-bending coupling, warped geometry, and behavior. *Comput Struct* 1994;50(4):549-55.
- [55] Groenwold AA, Stander N. An efficient 4-node 24 dof thick shell finite element with 5-point quadrature. *Eng Comput* 1995;12(8):723-47.
- [56] Kim JH, Lee BC. A four-node degenerated shell element with drilling degrees of freedom. *Struct Eng Mech* 1998;6(8):921-37.
- [57] Choi CK, Lee PS, Park YM. Defect-free 4-node flat shell element: NMS-4F element. *Struct Eng Mech* 1999;8(2):207-31.
- [58] Choi CK, Lee TY. Efficient remedy for membrane locking of 4-node flat shell elements by non-conforming modes. *Comp Meth Appl Mech Eng* 2003;192(16):1961-71.
- [59] Taylor RL. Finite element analysis of linear shell problems. In Whiteman, JR (ed.), *Proceedings of the Mathematics in Finite Elements and Applications* 1987:191-203.
- [60] Batoz JL, Bathe KJ, Ho LW. A study of three-node triangular plate bending elements. *Int J Num Meth Eng* 1980;15(12):1771-812.
- [61] Fricker AJ. An improved three-noded triangular element for plate bending. *Int J Num Meth Eng* 1985;21(1):105-14.
- [62] Auricchio F, Taylor RL. A generalized elastoplastic plate theory and its algorithmic implementation. *Int J Num Meth Eng* 1994;37(15):2583-608.
- [63] Argyris J, Tenek L. An efficient and locking-free flat anisotropic plate and shell triangular element. *Comp Meth Appl Mech Eng* 1994;118(1):63-119.
- [64] Onate E, Zárata F. Rotation-free triangular plate and shell elements. *Int J Num Meth Eng* 2000;47(1-3):557-603.

- [65] Belytschko T, Tsay CS, Liu WK. A stabilization matrix for the bilinear Mindlin plate element. *Comp Meth Appl Mech Eng* 1981;29(3):313-27.
- [66] Hughes TJ, Liu WK. Nonlinear finite element analysis of shells: Part I. Three-dimensional shells. *Comp Meth Appl Mech Eng* 1981;26(3):331-62.
- [67] Belytschko T, Tsay CS. A stabilization procedure for the quadrilateral plate element with one-point quadrature. *Int J Num Meth Eng* 1983;19(3):405-19.
- [68] Belytschko T, Lin JJ, Chen-Shyh T. Explicit algorithms for the nonlinear dynamics of shells. *Comp Meth Appl Mech Eng* 1984;42(2):225-51.
- [69] Belytschko T, Wong BL, Chiang HY. Advances in one-point quadrature shell elements. *Comp Meth Appl Mech Eng* 1992;96(1):93-107.
- [70] Belytschko T, Leviathan I. Physical stabilization of the 4-node shell element with one point quadrature. *Comp Meth Appl Mech Eng* 1994;113(3):321-50.
- [71] Zhu Y, Zacharia T. A new one-point quadrature, quadrilateral shell element with drilling degrees of freedom. *Comp Meth Appl Mech Eng* 1996;136(1):165-203.
- [72] Kim KD, Lomboy GR, Voyiadjis GZ. A 4-node assumed strain quasi-conforming shell element with 6 degrees of freedom. *Int J Num Meth Eng* 2003;58(14):2177-200.
- [73] Belytschko T, Leviathan I. Projection schemes for one-point quadrature shell elements. *Comp Meth Appl Mech Eng* 1994;115(3):277-86.
- [74] Lee SW, H Plan TH. Improvement of plate and shell finite elements by mixed formulations. *AIAA J* 1978;16(1):29-34.
- [75] Andelfinger U, Ramm E. EAS-elements for two-dimensional, three-dimensional, plate and shell structures

and their equivalence to HR-elements. *Int J Num Meth Eng* 1993;36(8):1311-37.

[76] Bischoff M, Ramm E. Shear deformable shell elements for large strains and rotations. *Int J Num Meth Eng* 1997;40:4427-49.

[77] Witkowski W. 4-Node combined shell element with semi-EAS-ANS strain interpolations in 6-parameter shell theories with drilling degrees of freedom. *Comput Mech* 2009;43(2):307-19.

[78] Rengarajan G, Aminpour MA, Knight NF. Improved assumed-stress hybrid shell element with drilling degrees of freedom for linear stress, buckling and free vibration analyses. *Int J Num Meth Eng* 1995;38(11):1917-43.

[79] Sze KY, Sim YS, Soh AK. A hybrid stress quadrilateral shell element with full rotational DOFS. *Int J Num Meth Eng* 1997;40(10):1785-1800.

[80] Sansour C, Kollmann FG. Families of 4-node and 9-node finite elements for a finite deformation shell theory. An assesment of hybrid stress, hybrid strain and enhanced strain elements. *Comput Mech* 2000;24(6):435-47.

[81] Cen S, Zhou MJ, Fu XR. A 4-node hybrid stress-function (HS-F) plane element with drilling degrees of freedom less sensitive to severe mesh distortions. *Comput Struct* 2011;89(5):517-28.

[82] Pian TH. Derivation of element stiffness matrices by assumed stress distributions. *AIAA J* 1964;2(7):1333-36.

[83] Stander N, Matzenmiller A, Ramm E. An assessment of assumed strain methods in finite rotation shell analysis. *Eng Comput* 1989;6(1):58-66.

[84] Koschnick F, Bischoff M, Camprubí N, Bletzinger KU. The discrete strain gap method and membrane locking. *Comp Meth Appl Mech Eng* 2005;194(21):2444-463.

[85] Vampa V. Analysis of in-layer strains in the low order MITC shell element. *Latin Am J Solid Struct* 2007;4(2):87-102.

- [86] Dvorkin EN, Vassolo SI. A quadrilateral 2-D finite element based on mixed interpolation of tensorial components. *Eng Comput* 1989;6(3):217-24.
- [87] Argyris J, Tenek L. A practicable and locking-free laminated shallow shell triangular element of varying and adaptable curvature. *Comp Meth Appl Mech Eng* 1994;119(3):215-82.
- [88] Wempner G, Talaslidis D, Hwang CM. A simple and efficient approximation of shells via finite quadrilateral elements. *J Appl Mech* 1982;49(1):115-20.
- [89] Macneal RH. Derivation of element stiffness matrices by assumed strain distributions. *Nuc Eng Des* 1982;70(1):3-12.
- [90] Hughes TJR, Tezduyar T. Finite elements based upon Mindlin plate theory with particular reference to the four-node bilinear isoparametric element. *J Appl Mech* 1981;48(3):587-96.
- [91] Prathap G. The finite element method in structural mechanics: principles and practice of design of field-consistent elements for structural and solid mechanics. Dordrecht: Kluwer Academic; 1993.
- [92] Simo JC, Rifai MS. A class of mixed assumed strain methods and the method of incompatible modes. *Int J Num Meth Eng* 1990;29(8):1595-638.
- [93] Büchter N, Ramm E, Roehl D. Three-dimensional extension of non-linear shell formulation based on the enhanced assumed strain concept. *Int J Num Meth Eng* 1994;37(15):2551-68.
- [94] Prathap G, Bhashyam GR. Reduced integration and the shear-flexible beam element. *Int J Num Meth Eng* 1982;18(2):195-210.
- [95] Stolarski H, Belytschko T. Membrane locking and reduced integration for curved elements. *J Appl Mech* 1982;49(1):172-76.
- [96] Stolarski H, Belytschko T. Shear and membrane locking in curved C0 elements. *Comp Meth Appl Mech*

Eng 1983;41(3):279-96.

[97] Belytschko T, Stolarski H, Liu WK, Carpenter N, Ong JS. Stress projection for membrane and shear locking in shell finite elements. *Comp Meth Appl Mech Eng* 1985;51(1):221-58.

[98] Pitkäranta J. The problem of membrane locking in finite element analysis of cylindrical shells. *Num Math* 1992;61(1):523-42.

[99] Bucelem ML, Bathe KJ. Locking behavior of isoparametric curved beam finite elements. *Appl Mech Rev* 1995;48(11S):S25-S29.

[100] Lee PS, Bathe KJ. Insight into finite element shell discretizations by use of the “basic shell mathematical model”. *Comput Struct* 2005;83(1):69-90.

[101] Irons BM, Razzaque A. Experience with the patch test for convergence of finite elements. *The Mathematical Foundations of the Finite Element Method with Applications to Partial Differential Equations*. New York: Academic Press; 1972.

[102] Huang HC, Hinton E. A nine node Lagrangian Mindlin plate element with enhanced shear interpolation. *Eng Comput* 1984;1(4):369-79.

[103] Ko Y, Lee PS, Bathe KJ. A New MITC4+ shell element. *Comput Struct*, in preparation.

[104] Chen XM, Cen S, Long YQ, Yao ZH. Membrane elements insensitive to distortion using the quadrilateral area coordinate method. *Comput Struct* 2004;82(1):35-54.

[105] Cen S, Chen XM, Fu XR. Quadrilateral membrane element family formulated by the quadrilateral area coordinate method. *Comp Meth Appl Mech Eng* 2007;196(41):4337-53.

[106] Cen S, Chen XM., Li CF, Fu XR. Quadrilateral membrane elements with analytical element stiffness matrices formulated by the new quadrilateral area coordinate method (QACM-II). *Int J Num Meth Eng* 2009;77(8):1172-200.

- [107] Long ZF, Cen S, Wang L, Fu XR, Long YQ. The third form of the quadrilateral area coordinate method (QACM-III): theory, application, and scheme of composite coordinate interpolation. *Fin Elem Anal Des* 2010;46(10):805-18.
- [108] Lee PS, Bathe KJ. The quadratic MITC plate and MITC shell elements in plate bending. *Adv Eng Soft* 2010;41(5):712–28.
- [109] Systèmes D. ABAQUS 6.12 Theory manual. Dassault Systèmes Simulia Corp., Providence, Rhode Island, 2012.
- [110] Belytschko T, Wong BL, Stolarski H. Assumed strain stabilization procedure for the 9-node Lagrange shell element. *Int J Num Meth Eng* 1989;28(2):385-414.
- [111] Jung WY, Han SC. An 8-node shell element for nonlinear analysis of shells using the refined combination of membrane and shear interpolation functions. *Math Prob Eng* 2013.
- [112] Ko Y, Lee PS, Bathe KJ. The MITC4+ shell element in geometric nonlinear analysis. *Comput Struct*, in preparation.
- [113] Bathe KJ, Bolourchi S. A geometric and material nonlinear plate and shell element. *Comput Struct* 1980;11(1):23-48.
- [114] Bathe KJ, Dvorkin E, Ho LW. Our discrete-Kirchhoff and isoparametric shell elements for nonlinear analysis—an assessment. *Comput Struct* 1983;16(1):89-98.
- [115] Sze KY, Liu XH, Lo SH. Popular benchmark problems for geometric nonlinear analysis of shells. *Fin Elem Anal Des* 2004;40(11):1551-69.
- [116] Arciniega RA, Reddy JN. Tensor-based finite element formulation for geometrically nonlinear analysis of shell structures. *Comp Meth Appl Mech Eng* 2007;196(4):1048-73.

[117] Ko Y, Lee PS. A 6-node triangular solid-shell element for linear and nonlinear analysis. *Int J Num Meth Eng*, submitted.

[118] Kim DN, Bathe KJ. A 4-node 3D-shell element to model shell surface tractions and incompressible behavior. *Comput Struct* 2008;86(21):2027-41.

[119] Sussman T, Bathe KJ. 3D-shell Elements for Structures in Large Strains. *Comput Struct* 2013;122:2-12.

요 약 문

연속체 역학 기반 4 절점 쉘 유한요소의 막잠김 현상 해결

쉘 구조물은 공학적으로나 자연적으로 널리 존재하지만, 그 거동현상을 수학적으로 해석할 수 있는 방법이 없어 유한요소법과 같은 수치해석이 주로 쓰인다. 이번 연구에서는, 어떠한 쉘 구조물의 형태나 거동에 관계없이 정확하고, 효율적이며 안정적인 해석을 수행할 수 있는 저차 쉘 유한요소들을 개발하는 것을 목표로 한다.

효과적인 쉘 유한요소는 등방성(isotropy) 거동을 보이고, 일관성(consistency)와 타원율(ellipticity) 조건에서 오는 다양한 기본적인 테스트들을 만족해야 한다. 모눈 실험(patch test)와 영에너지 모드 실험(zero-energy mode test)가 대표적인 테스트로, 쉘 유한요소가 작은 메쉬 개수에서도 정확한지와 정적, 동적 해석에 관계없이 쓰일 수 있는지를 각각 테스트한다. 또한 해의 수렴성능 면에서 쉘 구조물의 형상, 두께, 경계조건과 하중 등에 상관없는 최적의 수렴 거동을 보여야 한다. 수렴 거동이 유한요소의 메쉬 크기를 작게 함과 관계없이 큰 오차로 영향을 받는 현상을 잠김 현상이라고 하며, 막 잠김, 전단 잠김, 두께 잠김 현상 등이 있다.

쉘 유한요소를 감절점 쉘(degenerated), 연속체 쉘(solid-shell)과 평판 쉘(flat shell)로 구별할 수 있고, 현재까지 수행된 연구들을 보았을 때 그 장, 단점 및 해결해야 할 부분 또한 상이하다. 계산 시간 면에서 효율적이어서 널리 쓰이는 저차 쉘 유한요소들의 경우, 사각형 감절점 쉘의 막잠김 현상을 효과적으로 해결하는 것은 오랜 유한요소 분야의 난제였으며, 또한 두께 잠김 현상을 해결해서 삼각형 연속체 쉘을 만드는 것 또한 가치있는 연구이다.

사각형 4 노드 감절점 쉘 유한요소는 대체 변형률장 방식으로 전단 잠김현상을 제거한 요소 (MITC4 쉘 유한요소)가 널리 쓰이고 있다. 그러나 요소가 굽어진 형상을 가질 때 굽힘 거동에서 발생하는 막 잠김 현상은 효과적인 해결책이 오랫동안 나오지 않았다. 널리 쓰이는 저차 수치 적분(reduced integration)은 거짓영에너지 모드(spurious zero energy mode)를 가짐으로 인해 안정화 행렬을 사용해야 하며, 물리적인 영에너지 모드(physical rigid body mode)가 제대로 표현되지 않아 변위 투사(displacement projection) 등 쉘의 물리적 거동에 영향을 주는 기법들이 쓰여야 한다. 또한 대체 막변형률장을 이용한 지금까지의 연구들은 기본적인 테스트들 중, 특히 모눈 실험(patch test)와 막 성능 자체를 보존하는 것에서 효과적이지 못했다.

사각형 4 노드 감절점 쉘 유한요소의 개발을 위해 일반적인 형상의 쉘 유한요소에서 막 잠김 현상이 발생하는 원인을 밝혀 내었다. 이로부터 3 가지의 개선된 사각형 쉘 유한요소 (MITC4+, MITC4+N, new MITC4+)이 개발되었다. 대체 막변형률장에 기초로 한 이 요소들은, 지금까지의 연구들이 모눈 실험 통과와 막 성능 보존과 같은 기본 테스트들을 만족하지 못했던 어려움을 극복하였다. 마지막 사각형 감절점 쉘 유한요소(new MITC4+)의 경우 막 성능도 기존의 유한요소(MITC4)와 동일하며, 굽힘 거동에서 최적의 거동에 가까운 수렴 성능을 보인다. 또한 복잡한 계산을 요구하는 기하 비선형 문제에서 기존의 유한요소(MITC4)와 유사한 안정적인 성능을 보인다.

새롭게 개발된 삼각형 6 노드 연속체 쉘 유한요소는 기존에 대체 변형률장 방식으로 전단 잠김현상을 제거한 감절점 3 노드 쉘 유한요소 (MITC3+ 쉘 유한요소) 및 기존에 쓰이는 두께 잠김현상의 해결책 중 효과적인 강화 대체 변형률장 방식(Enhanced Assumed Strain) 을 기초로 한다. 새롭게 개발된 삼각형 연속체 쉘 유한요소(MITC-S6)는 기본적인 테스트들을 만족하며, 굽힘 거동에서 최적에 가까운 수렴 성능을 보인다. 기하 비선형 문제에서도 기존의 유한요소들과 일치하는 결과를 내었다.

핵심어: 쉘 유한요소, 연속체 쉘 유한요소, 대체 변형률장, 막잠김 현상, 두께 잠김 현상

감 사 의 글

평범하거나 그 미만이었던 모습의 제가 현재의 위치에 오를 수 있게 만들어 주신 지도교수님 이필승 교수님께 무한히 감사드립니다. 또한 언제나 최선을 다하는 학생의 입장을 지지해 주시던 심사위원 정 현 교수님께 감사드립니다. 이번 학위 논문의 심사를 맡아 주신 유한요소 분야의 전문가이신 이병채 교수님, 김도년 교수님, 그리고 윤정환 교수님께 감사드립니다.

멀리서 저를 응원해 주신 김양한 교수님과 박광춘 교수님 그리고 MIT Bathe 교수님, 학생들의 입장을 앞장서서 고려해 주시는 김경웅 교수님, 너그러움과 실력을 동시에 갖추신 윤성기 교수님, 노력하는 리더쉽을 가르쳐 주신 이두용 교수님, 칼 같은 카리스마를 가지신 이종원 교수님, 창조적인 마인드를 알려주신 양동열 교수님, 학사과정 때 지도를 아끼지 않으신 배중면 교수님과 김정원 교수님, 예술적인 세계를 일깨워 주신 변계원 전 교수님, 인지과학 분야에 빠져들게 만들어 주신 김정훈 교수님, 인연과 사명감의 중요성을 알려주신 허 훈 교수님, 간간함과 빠른 일처리를 알려주신 김광준 교수님과 김기태 선배님, 제게 항상 큰 힘이 되어 주신 김진균 선배님께 모두 감사드립니다.

이 밖에 응원을 아끼지 않았던 경호형, 윤규형, 김산 형, 대건형, 주성이형, 헌신하는 모습을 알려주신 강현이형, 철후형, 최걸기 연구원, 동화, 정호형, 그리고 효진이, 채민씨, 형준씨, 현덕이, 훈태, 이병도 님, 김성윤 님께도 감사드립니다. 이 밖에도 승균이형, 준건이형, 희규씨 등 같은 대학원 소속 학생분께 감사드립니다.

마지막으로 제가 연구를 할 수 있게 지원해 준 대한민국, 그리고 제가 과제를 수행할 수 있도록 격려하고 도와주신 한순홍 교수님, 신영식 교수님, 김용욱 연구교수님, 충남대학교 노인식 교수님, 울산대학교 조상래 교수님께도 감사드립니다.